Université du Québec
Institut National de la Recherche Scientifique
Centre Énergie Matériaux
Télécommunications

Munich University of Applied Sciences
Department of Applied Sciences and
Mechatronics

Improving the power factor of thermoelectric materials by polymer-polymer blending

Par

Marc Daniel Paulik

Thèse présentée pour l'obtention du grade de
Maître es Sciences (M.Sc.)
en sciences de l'énergie et des matériaux

14.08.2025

Jury d'évaluation

Research Director	Prof. Emanuele Orgiu
Research Co-Director	Prof. Martina Schwager
Internal Reviewer, Jury President	Prof. Andreas Rüdiger
External Reviewer	Prof. Piero Cosseddu

Université du Québec
Institut National de la Recherche Scientifique
Centre Énergie Matériaux
Télécommunications

Hochschule München
Fakultät für angewandte
Naturwissenschaften und Mechatronik

Improving the power factor of thermoelectric materials by polymer-polymer blending

---

Master's Thesis

Thèse présentée pour l'obtention du grade de
Maîtrise en sciences (M. Sc.)
de l'énergie et des matériaux

zur Erlangung des akademischen Grades
Master of Science (M. Sc.)
in Mikro- und Nanotechnik

Par

vorgelegt von

Marc Daniel Paulik

Submission Date:	Thursday 14th August, 2025
Supervisor (HM):	Prof. Martina Schwager
Supervisor (INRS):	Prof. Emanuele Orgiu

Résumé

Dans le contexte de l'augmentation des déchets électroniques et de la dissipation d'énergie dans tous les types de processus de conversion énergétique [1], les générateurs thermoélectriques (TEG) offrent une solution durable en convertissant la chaleur résiduelle en énergie électrique utilisable. On estime que plus de 60% de l'énergie produite dans les centrales électriques et les automobiles est perdue sous forme de chaleur résiduelle. [2, 3] Alors que les matériaux TEG inorganiques, tels que Bi_2Te_3, PbTe, SiGe ou $FeSi_2$, présentent une efficacité thermoélectrique élevée, avec des chiffres de mérite (zT) proches de 1 [4, 5] à température ambiante et des facteurs de puissance allant jusqu'à 10,000 $\mu Wm^{-1}K^{-2}$ [2, 4], ils dépendent d'éléments rares et toxiques tels que Te, Bi et Pb, et nécessitent des températures de traitement élevées, ce qui limite leur évolutivité et leur durabilité environnementale. [4, 6, 7] Les générateurs thermoélectriques organiques (OTEG), en revanche, sont composés d'éléments abondants et non toxiques, offrent une flexibilité mécanique et bénéficient d'une faible conductivité thermique intrinsèque (généralement <1 $Wm^{-1}K^{-1}$ [8]), ce qui accroît leurs performances thermoélectriques. [3] Néanmoins, ils restent limités par des paramètres de performance inférieurs, tels que des valeurs de zT autour de 0.4 et des facteurs de puissance typiques entre 100 et 3000 $\mu Wm^{-1}K^{-2}$ [9]. Cette thèse étudie une approche de dopage par mélange pour améliorer la performance thermoélectrique du polymère de type p poly(3-hexylthiophène) (P3HT) en utilisant le nouveau polymère de type n poly(3,7-dihydrobenzo[1,2-b :4,5-b']difuran-2,6-dione) (PBDF), étant donné que les deux polymères présentent un bon alignement de leurs orbitales moléculaires respectives. [10–12] La conductivité électrique, le coefficient Seebeck et le facteur de puissance ont été mesurés pour différents pourcentages de poids de PBDF à l'aide de configurations de test personnalisées. Les résultats montrent une amélioration du facteur de puissance de plus de quatre ordres de grandeur, de $2.0 \cdot 10^{-6}$ à 0.06 $\mu Wm^{-1}K^{-2}$, à 25 wt% PBDF dans les films coulés, principalement en raison d'une augmentation de la conductivité électrique de $2.0 \cdot 10^{-7}$ à 1.1 S/cm, tout en maintenant un coefficient Seebeck stable autour de 22 $\mu V/K$, avec une valeur exceptionnellement élevée de 160.6 $\mu V/K$ à 1 wt% PBDF. On a constaté que le type de porteur de charge du mélange passait du type p au type n entre 5 et 10 wt% de PBDF, où il reste de type n. L'analyse des transistors à effet de champ (FET) a confirmé l'amélioration de la mobilité linéaire à 1 wt% de PBDF, avec des valeurs augmentant jusqu'à un facteur 10 par rapport au P3HT pur, ce qui indique un dopage efficace sans conversion vers un transport de type n. Des défis de fabrication tels que la solubilité du PBDF et l'homogénéité du film ont été identifiés, avec des recommandations pour des stratégies de revêtement optimisées,

la sélection des solvants et les conditions de traitement.

Abstract

In the context of increasing electronic waste and energy dissipation in all types of energy conversion processes [1], thermoelectric generators (TEGs) offer a sustainable solution by converting waste heat into usable electrical energy. It is estimated that more than 60% of the energy generated in power plants and automobiles is lost in form of waste heat. [2, 3] While inorganic TEG materials, such as Bi_2Te_3, PbTe, SiGe or $FeSi_2$, exhibit high thermoelectric efficiency, with figures of merit (zT) approaching 1 [4, 5] at room temperature and power factors up to 10,000 $\mu Wm^{-1}K^{-2}$ [2, 4], they rely on scarce and toxic elements such as Te, Bi, and Pb, and require high processing temperatures, limiting their scalability and environmental sustainability. [4, 6, 7] Organic thermoelectric generators (OTEGs), in contrast, are composed of abundant, non-toxic elements, offer mechanical flexibility, and benefit from low intrinsic thermal conductivity (typically <1 $Wm^{-1}K^{-1}$ [8]), which boosts their thermoelectric performance. [3] Nevertheless, they remain limited by lower performance metrics, such as zT values around 0.4 and typical power factors between 100 and 3000 $\mu Wm^{-1}K^{-2}$ [9].

This thesis investigates a doping-by-blending approach to enhance the thermoelectric performance of the p-type polymer poly(3-hexylthiophene) (P3HT) using the novel n-type polymer poly(3,7-dihydrobenzo[1,2-b:4,5-b']difuran-2,6-dione) (PBDF), as both polymers exhibit a good alignment of their respective molecular orbitals. [10–12] Electrical conductivity, Seebeck coefficient, and power factor were measured for various PBDF weight percentages using customized test setups. The results show a power factor improvement by over four orders of magnitude, from $2.0 \cdot 10^{-6}$ to 0.06 $\mu Wm^{-1}K^{-2}$, at 25 wt% PBDF in drop-casted films, primarily due to an increase in electrical conductivity from $2.0 \cdot 10^{-7}$ to 1.1 S/cm, while maintaining a stable Seebeck coefficient around 22 $\mu V/K$, with an exceptionally high value of 160.6 $\mu V/K$ at 1 wt% PBDF. The charge carrier type of the blend was found to transition from p- to n-type between 5 and 10 wt% PBDF, from where on it remains n-type.

Field-effect transistor (FET) analysis confirmed enhanced linear mobility at 1 wt% PBDF, with values increasing by up to a factor of 10 compared to pure P3HT, further indicating effective doping without conversion to n-type transport. Fabrication challenges such as PBDF solubility and film homogeneity, both for spin-coating and drop-casting, were identified, with recommendations for optimized coating strategies, solvent selection, and processing conditions.

Zusammenfassung

Im Kontext zunehmender elektronischer Abfälle und Verluste in sämtlichen Energieumwandlungsprozessen [1] bieten thermoelektrische Generatoren (TEGs) eine nachhaltige Lösung, indem sie Abwärme in nutzbare elektrische Energie umwandeln. Schätzungen zufolge gehen über 60% der in Kraftwerken und Automobilen erzeugten Energie in Form von Abwärme verloren. [2, 3] Während anorganische TEG-Materialien wie Bi_2Te_3, PbTe, SiGe oder $FeSi_2$ eine hohe thermoelektrische Effizienz aufweisen, mit Gütezahlen (zT) nahe 1 [4, 5] bei Raumtemperatur und Leistungsfaktoren von bis zu 10.000 $\mu Wm^{-1}K^{-2}$ [2, 4], basieren sie auf seltenen und toxischen Elementen wie Te, Bi und Pb und erfordern hohe Prozesstemperaturen, was ihre Skalierbarkeit und Umweltverträglichkeit einschränkt. [4, 6, 7] Organische thermoelektrische Generatoren (OTEGs) hingegen bestehen aus reichlich vorhandenen, ungiftigen Elementen, sind mechanisch flexibel und zeichnen sich durch eine niedrige intrinsische Wärmeleitfähigkeit (von typischerweise <1 $Wm^{-1}K^{-1}$ [8]) aus , was ihre thermoelektrische Leistung begünstigt. [3] Dennoch bleiben sie durch geringere Leistungswerte limitiert, wie etwa zT-Werte um 0,4 und typische Leistungsfaktoren zwischen 100 und 3000 $\mu Wm^{-1}K^{-2}$ [9]. Diese Arbeit untersucht einen Dotierung-durch-Mischen-Ansatz zur Verbesserung der thermoelektrischen Eigenschaften des p-leitenden Polymers Poly(3-hexylthiophen) (P3HT) durch das neuartige n-leitende Polymer Poly(3,7-dihydrobenzo[1,2-b:4,5-b']difuran-2,6-dion) (PBDF), da beide Polymere eine günstige energetische Ausrichtung ihrer Molekülorbitale aufweisen. [10–12] Elektrische Leitfähigkeit, Seebeck-Koeffizient und Leistungsfaktor wurden für verschiedene Gewichtsprozente (wt%) von PBDF mithilfe eigens entwickelter Messaufbauten bestimmt. Die Ergebnisse zeigen eine Verbesserung des Leistungsfaktors um mehr als vier Größenordnungen, von $2{,}0 \cdot 10^{-6}$ bis 0,06 $\mu Wm^{-1}K^{-2}$, bei 25 wt% PBDF in drop-casting Filmen. Dies ist hauptsächlich auf einen Anstieg der elektrischen Leitfähigkeit von $2.0 \cdot 10^{-7}$ auf 1,1 S/cm zurückzuführen, während der Seebeck-Koeffizient recht stabil bei etwa 22 $\mu V/K$ bleibt, mit einem außerordentlich hohen Wert von 160,6 $\mu V/K$ bei 1 wt% PBDF. Der dominierende Ladungstransport der Mischung wechselt zwischen 5 und 10 wt% PBDF von p- zu n-Typ und bleibt ab diesem Bereich n-leitend. Die Analyse mittels Feldeffekttransistoren (FETs) bestätigte eine erhöhte lineare Mobilität bei 1 wt% PBDF, wobei die Werte im Vergleich zu reinem P3HT um bis zu das Zehnfache anstiegen. Dies deutet für diesen prozentualen Anteil auf ein effektives Doping hin, ohne dass ein Übergang zu n-Typ-Transport erfolgt. Herausforderungen bei der Herstellung, wie die Löslichkeit von PBDF und die Homogenität der Filme, wurden identifiziert. Abschließend werden Empfehlungen zur Optimierung von Beschichtungsverfahren, Lösungsmittelauswahl und Prozessparametern gegeben.

Synopsis

The synopsis is a concise French version of the Master's thesis, covering everything from the introduction to the conclusion. It highlights the main themes and important points discussed, and explains the working hypotheses that guided the research. It also outlines the main research objectives, describes the methods used, and summarizes the main findings and results. The aim of this summary is to provide the reader with a clear understanding of the main contributions of the thesis and insights into the research conducted.

Le synopsis est une version française concise du mémoire de master, qui va de l'introduction à la conclusion. Il met en évidence les principaux thèmes et points importants discutés, et explique les hypothèses de travail qui ont guidé la recherche. Il expose également les principaux objectifs de la recherche, décrit les méthodes utilisées et résume les principales conclusions et résultats. L'objectif de ce résumé est de permettre au lecteur de bien comprendre les principales contributions de la thèse et d'avoir un aperçu de la recherche menée.

1 Introduction

Le réchauffement climatique, ainsi que l'utilisation croissante d'appareils électroniques, entraînent une augmentation des déchets électroniques et de la production de chaleur perdue. Plus de 60% de l'énergie générée dans les centrales électriques et les véhicules est dissipée sous forme de chaleur [1–3]. Les générateurs thermoélectriques (TEGs) permettent de convertir cette chaleur perdue en électricité. À ce jour, des matériaux inorganiques comme le Bi_2Te_3, le PbTe, le SiGe ou le $FeSi_2$ sont majoritairement utilisés en raison de leur forte conductivité électrique et de leur stabilité thermique jusqu'à 600 K [2, 4]. Ces matériaux atteignent un facteur de mérite zT proche de 1 à température ambiante, contre environ 0.4 pour des matériaux organiques comme le PEDOT :PSS [4, 5].
Cependant, les matériaux inorganiques présentent plusieurs inconvénients : la loi de Wiedemann–Franz lie leur conductivité électrique et thermique [13], et leur fabrication repose sur des éléments rares, coûteux et parfois toxiques (comme le Te, le Bi ou le Pb), avec un fort impact environnemental [4, 6, 7].
Les générateurs thermoélectriques organiques (OTEGs) apparaissent comme une alternative prometteuse. Ils offrent une flexibilité mécanique, un faible coût de production, et une conductivité thermique intrinsèquement basse ($<$1 $Wm^{-1}K^{-1}$) [3,4,8]. Des prototypes intégrés dans des textiles, destinés à capter la chaleur corporelle, ont montré des résultats encourageants, comme une puissance de sortie de 13 µW obtenue avec des matériaux Na(NiETT) et PEDOT :PSS [14, 15].
Néanmoins, les matériaux organiques souffrent encore d'une faible conductivité électrique et de faibles facteurs de puissance (100 à 3000 $\mu Wm^{-1}K^{-2}$), contre jusqu'à 10,000 $\mu Wm^{-1}K^{-2}$ pour des matériaux comme le NbFeSb [9, 16]. Pour améliorer leurs performances thermoélectriques, plusieurs stratégies de dopage sont à l'étude : dopage acide, électrochimique ou par mélange en solution [4]. Ce travail explore cette dernière méthode à travers l'étude du Poly-3-hexylthiophène (P3HT) et du nouveau polymère PBDF (Poly-3,7-dihydrobenzo[1,2-b :4,5-b´]difuran-2,6-dione), en raison de leur bon alignement des niveaux d'énergie.

2 Principes de la thermoélectricité organique

Ce chapitre traite de l'origine physique et chimique de la conductivité électrique et thermique des semi-conducteurs organiques, ainsi que des principes des méthodes de dopage. Il explique en outre le principe de fonctionnement des générateurs thermoélectriques, qui sont les dispositifs centraux sur lesquels cette étude se concentre.

2.1 Propriétés électroniques des matériaux organiques

Les semi-conducteurs organiques (OSCs) sont des molécules ou des polymères conjugués à base de carbone, présentant un comportement semi-conducteur. Contrairement aux semi-conducteurs inorganiques, ils se distinguent par leur structure moléculaire et les faibles interactions de type van der Waals entre les chaînes. Leur faible conductivité électrique s'explique par une large bande interdite et un chevauchement limité entre les molécules.

Leurs propriétés électroniques dépendent fortement de la structure conjuguée de leur squelette moléculaire, formé de l'alternance de liaisons simples et doubles entre atomes de carbone hybridés sp^2. Cela crée un système d'électrons π délocalisés qui définit des paramètres clés comme l'énergie d'ionisation (IE), l'affinité électronique (EA) et la différence HOMO–LUMO [17]. La Figure 1 illustre ces orbitales moléculaires et types de liaisons.

Le transport de charges dans les OSCs repose à la fois sur le chevauchement des orbitales π à l'intérieur des chaînes et sur les interactions entre molécules. La mobilité des porteurs de charge est influencée par la longueur et la structure des chaînes conjuguées : des chaînes plus longues améliorent généralement la mobilité, mais peuvent aussi engendrer des enchevêtrements ou défauts structuraux [18, 19]. Des stratégies de conception telles que l'ajustement de la masse molaire, l'ajout de chaînes latérales ou la modification de la bande interdite permettent d'optimiser ces propriétés.

Les films minces d'OSCs présentent souvent une anisotropie du transport électrique due à l'ordre moléculaire partiel issu de l'empilement π–π. Toutefois, leur faible cristallinité et la présence de pièges électroniques réduisent la mobilité. Le transport s'effectue par 'hopping' entre états localisés et entre domaines cristallins, soulignant l'importance d'une conception moléculaire optimisée pour améliorer les performances des semi-conducteurs organiques.

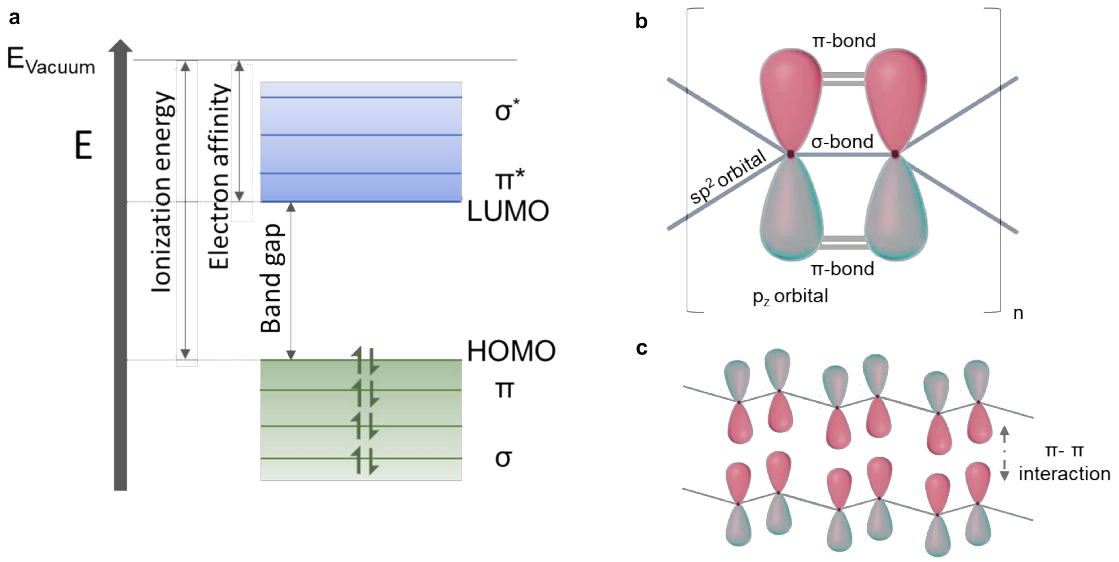

FIGURE 1 Visualisation des liaisons σ- et π pour les atomes de carbone et les chaînes de polymères. **a** montre les positions de l'énergie d'ionisation, de l'affinité électronique et de la bande interdite par rapport aux orbitales moléculaires occupées jusqu'à la plus élevée (HOMO) et aux orbitales moléculaires inoccupées, en commençant par la plus basse (LUMO). σ et π font référence aux orbitales de liaison, contrairement aux orbitales anti-liaison σ* et π*. **b** représente les différentes positions des liaisons σ- et π dans l'orbitale p_z entre deux atomes de carbone et les orbitales sp^2 adjacentes. **c** poursuit cette constellation pour les chaînes de polymères plus longues, en soulignant en outre l'interaction π-π entre les chaînes. [4]

2.1.1 Mécanismes de dopage dans les semi-conducteurs organiques

La conductivité électrique des semi-conducteurs organiques (OSC) dépend de la concentration en porteurs de charge et de leur efficacité de transport. Le dopage est la méthode la plus efficace pour augmenter la conductivité, atteignant des valeurs allant jusqu'à 10^4 S/cm, mais son contrôle précis reste difficile car il nécessite un ajustement fin des interactions entre le dopant et l'OSC.

Ces interactions influencent fortement les niveaux d'énergie moléculaires et dépendent de la distance spatiale et de l'orientation relative entre les molécules du dopant et de l'OSC. Le dopage augmente la densité des porteurs en introduisant des donneurs d'électrons (n-type) ou des accepteurs d'électrons (p-type). Les stratégies courantes incluent le dopage moléculaire, par transfert de charge, en surface, électrochimique et thermique.

Un mécanisme clé est le dopage par transfert de charge, où un électron est transféré en fonction de l'alignement énergétique entre le dopant et l'OSC :

- dopage p-type : lorsque le HOMO de l'OSC est situé au-dessus du LUMO du dopant, permettant le transfert d'électron vers le dopant.

- dopage n-type : lorsque le LUMO de l'OSC est en dessous du HOMO du dopant, facilitant le transfert d'électron du dopant vers l'OSC.

Cette approche est appliquée aux polymères étudiés dans ce travail.

2.1.2 Injection de charges dans les semi-conducteurs organiques

Les performances des dispositifs à semi-conducteurs organiques (OSCs) sont fortement influencées par la géométrie du dispositif et la résistance de contact, car ces paramètres déterminent l'efficacité de l'injection et du transport des charges. Lorsqu'une électrode métallique est mise en contact avec un OSC, les électrons s'écoulent du matériau ayant le niveau de Fermi le plus élevé vers celui ayant le niveau le plus bas. Pour assurer une injection de charges efficace, il est essentiel que les niveaux d'énergie du métal et de l'OSC soient bien alignés, afin de minimiser la barrière d'énergie à l'interface.
Cette interface est généralement modélisée à l'aide de la **barrière de Schottky** Φ_b, qui résulte de la différence entre les fonctions travail du métal et du semi-conducteur organique. Les caractéristiques de cette barrière — sa hauteur et sa largeur — dépendent de la concentration en porteurs de charge dans l'OSC. Lorsque cette concentration est élevée, la région de déplétion devient très étroite (environ 2–3 nm), et le transport des charges se fait principalement par effet tunnel. En revanche, lorsque la concentration en porteurs est faible, la largeur de la zone de déplétion augmente considérablement (de l'ordre de plusieurs dizaines de nanomètres), et l'injection de charges s'effectue par émission thermoïonique, les porteurs devant alors franchir thermiquement la barrière de Schottky.
L'application d'une tension externe à la jonction permet de réduire la hauteur effective de la barrière, améliorant ainsi l'efficacité de l'injection. Toutefois, cette méthode nécessite un apport énergétique supplémentaire, ce qui réduit l'efficacité énergétique globale du dispositif. La Figure 2 illustre l'interface métal–OSC et le rôle de la barrière de Schottky selon différents niveaux de dopage.

2.1.3 Caractéristiques des porteurs de charge dans les matériaux semi-conducteurs des transistors à effet de champ (FETs)

Les transistors à effet de champ (FETs) sont utilisés pour identifier les porteurs de charge dominants dans un matériau semi-conducteur et pour mesurer leur mobilité. Un FET typique se compose de trois électrodes : la source (S), le drain (D) et la grille (G). Le courant entre la source et le drain, noté I_{ds}, dépend à la fois de la tension entre le drain et la source V_{ds} et de la tension entre la grille et la source V_{gs}.
Les FETs peuvent être classés selon qu'ils utilisent un canal de type p ou de type n. La polarité des courbes I_{ds}–V_{ds} et I_{ds}–V_{gs} permet de distinguer les FETs à canal n de ceux à canal p. Les dispositifs à canal n présentent un courant de drain positif pour des tensions V_{ds}

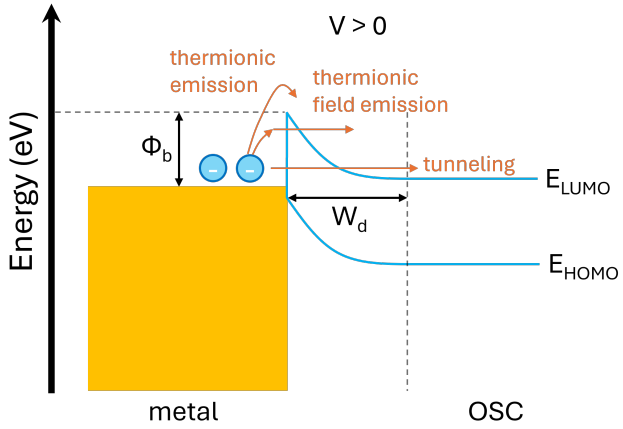

FIGURE 2 Schéma de l'interface entre un contact métallique et un OSC. La barrière de Schottky Φ_b résulte de la différence entre les fonctions de travail du métal et de l'OSC. Si l'OSC présente une forte concentration de porteurs de charge, la largeur de déplétion W_d devient faible, ce qui fait du transport par effet tunnel le transport dominant. Dans le cas contraire, Φ_b doit être surmonté thermiquement pour de faibles concentrations de porteurs. La barrière peut être réduite en appliquant une tension externe $V > 0$, ce qui conduit à la représentation de la courbure des niveaux d'énergie. [4]

positives, tandis que les dispositifs à canal p affichent un courant négatif pour des tensions V_{ds} négatives.

Les FETs fonctionnent principalement dans deux régimes : la **région linéaire (ou ohmique)** et la **région de saturation**, toutes deux utilisées pour extraire la mobilité des porteurs de charge.

Dans la **région linéaire**, le transistor se comporte comme une résistance contrôlée par la grille. Ce régime est atteint lorsque : $V_{gs} > V_{Th}$ et $V_{ds} < V_{gs} - V_{Th}$.

Le courant de drain est alors exprimé par :

$$I_{ds} = \mu C_i \frac{W}{L} \left((V_{gs} - V_{Th}) V_{ds} - \frac{V_{ds}^2}{2} \right) \tag{0.1}$$

Ici, μ est la mobilité des porteurs, C_i est la capacité par unité de surface de l'isolant de grille, W est la largeur du canal, et L est la longueur du canal.

Dans ce régime, la mobilité μ peut être extraite à partir de la pente $m_{lin} = \frac{\partial I_{ds}}{\partial V_{gs}}$ obtenue sur une courbe I_{ds}–V_{gs}, selon [20] :

$$\mu = m_{lin} \frac{L}{W} \frac{1}{C_i} = \frac{\partial I_{ds}}{\partial V_{gs}} \frac{L}{W} \frac{1}{C_i} \tag{0.2}$$

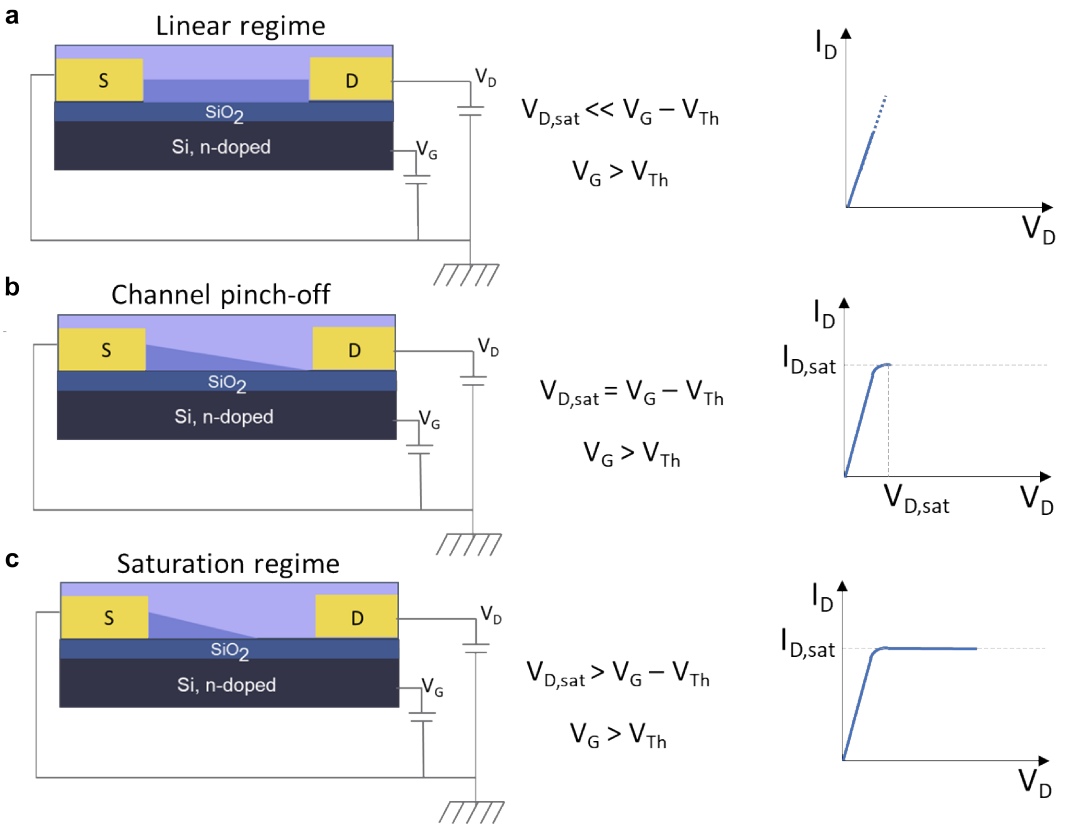

FIGURE 3 Schéma des deux régions des FET. **a** montre la région linéaire pour des tensions de drain $V_{D,sat}$ inférieures à la tension de grille V_G moins la tension de seuil V_{Th}. **b** montre le point de pincement du canal, où $V_{D,sat}$ est égal à $V_G - V_{Th}$ et où le dispositif commence à saturer, avant le régime de saturation de **c**. [17]

Dans la **région de saturation**, le canal est pincé (pinch-off) et le courant se stabilise. Ce régime commence lorsque : $V_{gs} > V_{Th}$ et $V_{ds} \geq (V_{gs} - V_{Th})$.

Le courant de drain est alors modélisé par :

$$I_{ds} = \frac{\mu C_i}{2} \frac{W}{L} (V_{gs} - V_{Th})^2 (1 + \lambda V_{ds}) \tag{0.3}$$

Le terme λ est le paramètre de modulation de longueur de canal, qui prend en compte la faible dépendance de I_{ds} à V_{ds} même en régime de saturation.

Dans cette région, la mobilité est extraite à l'aide de la pente $m_{sat} = \frac{\partial \sqrt{I_{ds}}}{\partial V_{gs}}$ obtenue sur une courbe $\sqrt{I_{ds}}$–V_{gs}, selon [20] :

$$\mu = m_{sat}^2 \frac{2L}{W} \frac{1}{C_i} = \left(\frac{\partial \sqrt{I_{ds}}}{\partial V_{gs}} \right)^2 \frac{2L}{W} \frac{1}{C_i} \tag{0.4}$$

La Figure 3 illustre les différents régimes de fonctionnement des FETs et résume les équations correspondantes.

Caractéristiques des transistors organiques à effet de champ (OFETs)

Une caractéristique déterminante des matériaux organiques, par rapport aux semi-conducteurs inorganiques, est la distribution plus large des niveaux d'énergie de leurs orbitales moléculaires (OM). Cela est dû à la nature amorphe des polymères, qui ne possèdent pas la structure cristalline ordonnée des matériaux inorganiques, ce qui entraîne des bandes d'énergie moins nettement définies. Les HOMO et LUMO, appelées orbitales frontières, jouent un rôle essentiel dans le comportement électrique des molécules organiques. Dans de nombreux cas, le premier état excité d'une molécule organique peut être décrit majoritairement (à 80–95%) par une configuration contenant un électron dans la HOMO et un autre dans la LUMO [21]. Dans les OFETs, l'interface entre les électrodes source/drain et le canal semi-conducteur est cruciale. Les barrières à cette jonction entravent le transport de charge, et la morphologie des électrodes peut influencer la formation du canal ainsi que les performances globales du dispositif. Des matériaux comme l'or sont souvent utilisés comme électrodes en raison de leur haute fonction de travail, qui s'aligne bien avec la HOMO de nombreux semi-conducteurs organiques [18].

2.2 Propriétés thermoélectriques des matériaux organiques

2.2.1 L'effet Seebeck

L'effet Seebeck décrit la force électromotrice générée lorsqu'une différence de température existe à travers un matériau conducteur électrique. Le coefficient de Seebeck SS quantifie cet effet selon, [17, 22] :

$$S = -\frac{\Delta V}{\Delta T} \tag{0.5}$$

où ΔV est la tension thermoélectrique et ΔT la différence de température. En explicitant les positions :

$$S = -\frac{V_{gauche} - V_{droite}}{T_{gauche} - T_{droite}} \tag{0.6}$$

Le signe négatif indique que le gradient de tension est opposé au gradient de température. Lors des mesures pratiques, la tension totale inclut aussi la contribution des fils de mesure, comme dans un thermocouple. Convention de signe : p-type $\rightarrow S > 0$ (les trous migrent du chaud vers le froid), n-type $\rightarrow S < 0$ (les électrons migrent du chaud vers le froid).
Les courants électrique et thermique dans un matériau thermoélectrique s'expriment par : [22]

$$J = \sigma \mathbf{E} - \sigma S \frac{dT}{dx} \tag{0.7}$$

$$J_Q = (T\sigma S)\mathbf{E} - (\kappa_0 + \kappa_L)\frac{dT}{dx} \tag{0.8}$$

où J est la densité de courant électrique, $\mathbf{E}$ le champ électrique, σ la conductivité électrique, et J_Q le flux thermique. Le second terme traduit la contribution induite par le gradient

thermique. La différence des distributions de Fermi-Dirac entre deux points aux températures T_1 et T_2 est : [23]

$$f_1 - f_2 \approx f_0(E_F, T_1) - f_0(E_F, T_2) \tag{0.9}$$
$$\approx -\frac{\partial f_0}{\partial T}\Delta T \tag{0.10}$$
$$\approx \frac{f_0(T_1) - f_0(T_1 + \Delta T)}{\Delta T}\Delta T \tag{0.11}$$
$$\approx -\frac{E - E_F}{T}\left(-\frac{\partial f_0(E)}{\partial E}\right)\Delta T \tag{0.12}$$

Ceci conduit à un courant net décrit par la formule de Landauer : [24]

$$I = \frac{2e}{h}\int T(E)M(E)[f_1(E) - f_2(E)]dE \tag{0.13}$$

où $T(E)$ est la transmission, $M(E)$ le nombre de canaux de transport, et $f(E)$ la distribution de Fermi. En incluant la différence de température, le courant devient :

$$I = -\left[\int\left(\frac{E - E_F}{eT}\right)\sigma'(E)dE\right]\Delta T \tag{0.14}$$

où $\sigma'(E)$ est la conductivité dépendant de l'énergie. En combinant ces expressions, on obtient, [23, 25]

$$S = -\frac{\int\left(\frac{E-E_F}{eT}\right)\sigma'(E)dE}{\int\sigma'(E)dE} = -\int\frac{E - E_F}{eT}\frac{\sigma'(E)dE}{\sigma} \tag{0.15}$$

ce qui montre que S est une moyenne pondérée en énergie de la différence $E - E_F$, normalisée par la conductivité totale. En termes de l'énergie moyenne des porteurs E_J :

$$S = -\frac{E_J - E_F}{eT} \tag{0.16}$$

Pour les semi-conducteurs, $E_J >> E_F$, donc $|S|$ est grand. Pour les métaux ou semi-conducteurs fortement dopés, $E_J \approx E_F$, donnant un S très faible.

2.2.2 Générateurs thermoélectriques (TEGs)

Les générateurs thermoélectriques convertissent la chaleur en énergie électrique grâce à l'effet Seebeck, où un gradient de température à travers un matériau induit une différence de potentiel en raison du mouvement inégal des porteurs de charge. Un TEG typique est constitué d'un matériau thermoélectrique pris en sandwich entre des électrodes chaude (T_h) et froide (T_c).

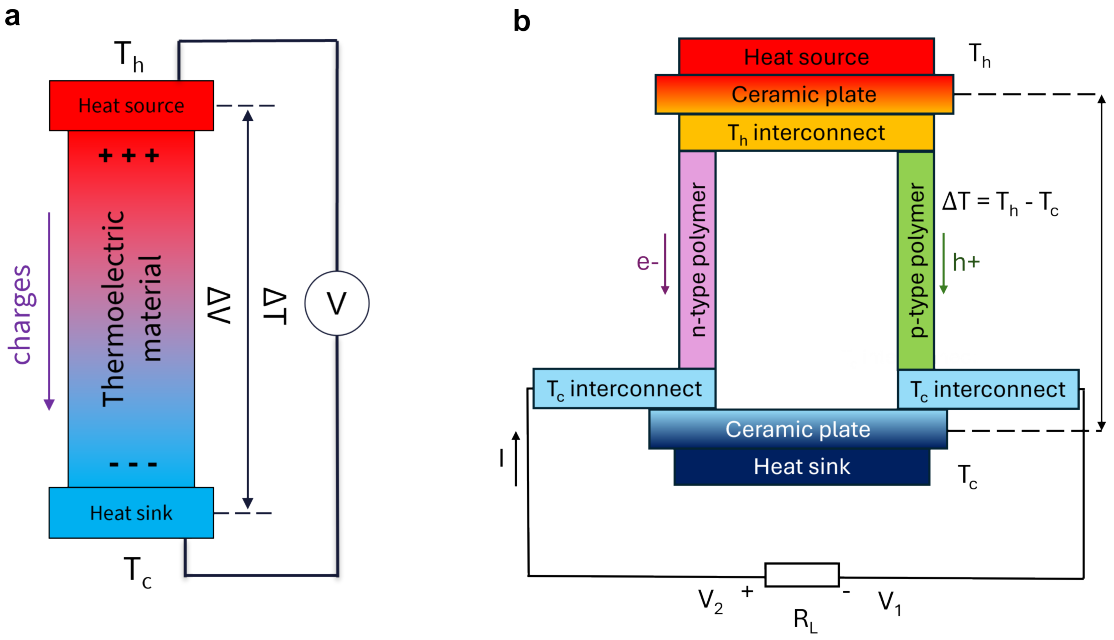

FIGURE 4 Schéma du principe de fonctionnement d'un générateur thermoélectrique (TEG). **a** montre un exemple de base pour un TEG à une jambe. Il fonctionne sur la base de l'effet Seebeck, selon lequel une différence de tension ΔV est induite par un gradient de température externe ΔT. Les structures à deux branches, comme dans **b**, sont couramment utilisées en répétition de centaines ou de milliers d'éléments pour accumuler la puissance de sortie générée.

L'efficacité maximale d'un dispositif est donnée par :

$$\eta_{TE} = \eta_c \frac{\sqrt{1+zT}-1}{\sqrt{1+zT}+1-\eta_c} \tag{0.17}$$

Le facteur de mérite zT évalue la performance d'un matériau, [3, 26]

$$zT = \frac{S^2 \sigma T}{\kappa} \tag{0.18}$$

où κ est la conductivité thermique et T la température. Une efficacité élevée nécessite un S et une σ élevés, et une κ faible. Comme κ est difficile à mesurer, on utilise souvent le facteur de puissance : [17]

$$PF = S^2 \sigma \tag{0.19}$$

Un TEG associe généralement plusieurs branches n-type et p-type en série pour augmenter la puissance de sortie (Figure 4). Le flux thermique entraîne les électrons (n-type) et les trous (p-type) du côté chaud vers le côté froid, générant un courant qui alimente une charge externe R_L. [3, 14]

2.2.3 Transport de chaleur dans les semi-conducteurs organiques

La chaleur est principalement transportée par les phonons et les électrons, avec une conductivité thermique totale :

$$\kappa = \kappa_{ph} + \kappa_e \tag{0.20}$$

Dans les matériaux organiques faiblement dopés, κ_e est négligeable. [27] Pour les matériaux cristallins, la contribution phononique suit le modèle du gaz de phonons, [28]

$$\kappa_{ph} = \frac{1}{3} C v_g l = \frac{1}{3} C v_g^2 \tau \tag{0.21}$$

où C est la capacité calorifique volumique, v_g est la vitesse de groupe des phonons, l est le libre parcours moyen, et τ est le temps de relaxation. Les semi-conducteurs organiques amorphes, dépourvus d'ordre à longue portée et basés sur des interactions faibles (empilement $\pi - \pi$, liaisons hydrogène, interactions de van der Waals), sont difficiles à modéliser pour le transport thermique. [27]
Les polymères semi-cristallins montrent une forte augmentation de κ avec la mobilité, tandis que les matériaux amorphes présentent peu de variation. Globalement, κ varie d'un ordre de grandeur au maximum, contre huit ordres pour la mobilité, ce qui indique que la conductivité électrique ($\sigma = ne\mu$) est beaucoup plus ajustable que la conductivité thermique. [8]

3 Méthodes

S'appuyant sur les principes théoriques exposés dans le chapitre précédent, cette section détaille les procédures expérimentales et les matériaux utilisés tout au long de l'étude. L'accent est mis sur les polymères organiques sélectionnés pour l'étude, les techniques de fabrication et les dispositions utilisées pour les échantillons de conductivité, de coefficient Seebeck et de transistor à effet de champ, ainsi que les techniques de mesure spécifiques employées pour caractériser leurs propriétés.

3.1 Polymères organiques visés par cette étude

3.1.1 Poly-3,4-ethylenedioxythiophene polystyrene sulfonate (PEDOT :PSS, conducteur de type p)

Le poly(3,4-éthylènedioxythiophène) (PEDOT) est un polymère conducteur largement étudié pour sa grande stabilité, son gap énergétique modéré et son faible potentiel rédox. Son principal inconvénient est sa faible solubilité, qui peut être surmontée en le combinant avec le polystyrène sulfonate (PSS). Ce dernier agit comme un contre-ion, équilibrant la charge de la molécule et améliorant sa solubilité dans l'eau, formant ainsi le composite conducteur de type p PEDOT :PSS. Une dispersion aqueuse à 2.8% en poids de chez Sigma Aldrich est utilisée dans cette étude. PEDOT :PSS détient la meilleure efficacité thermœlectrique rapportée parmi les matériaux organiques conducteurs, avec un facteur de mérite zT=0.42 [5]. Il est utilisé dans de nombreuses applications telles que les écrans tactiles, les diodes électroluminescentes organiques (OLED) et les cellules solaires organiques. Dans ce travail, il est utilisé pour vérifier la fonctionnalité de deux bancs de mesure destinés à la caractérisation électrique et à la détermination du coefficient Seebeck, grâce à ses propriétés bien documentées.

3.1.2 Poly-3-hexylthiophene (P3HT)

Le P3HT est un polymère de type p connu pour sa haute mobilité de trous et sa structure semi-cristalline, composée de régions amorphes et cristallines [29]. Il est bien soluble dans le chloroforme, jusqu'à une concentration de 38 mg/mL [30], et utilisé ici à une concentration de 5 mg/mL. Son niveau HOMO est estimé à –5.08 eV par voltampérométrie cyclique [10], ou à –4.9 eV par spectroscopie photoélectronique ultraviolette (UPS) et spectroscopie photoélectronique à rayons X résolue en angle (AR-XPS) [11]. Sa conductivité électrique à température ambiante se situe entre 6.7 et 9.4 nS/cm [31]. Le produit utilisé dans ce travail est le LT-S909 de Luminescence Technology Corp., avec une masse molaire de 165.28 g/mol.

3.1.3 Poly-3,7-dihydrobenzo[1,2-b :4,5-b´]difuran-2,6-dione (PBDF,conducteur de type n)

Le PBDF est un polymère organique conducteur de type n, soluble en solution, issu de réactions en cascade catalysées par le cuivre. Il est stable à l'entreposage entre –20 et 65°C. À ce jour, le PBDF possède le niveau LUMO le plus bas parmi les polymères n organiques, ce qui en fait le seul conducteur n organique considéré comme thermodynamiquement stable. Un polymère est dit cinétiquement stable si son LUMO est inférieur à –4.0 eV (afin d'éviter les réactions de réduction avec l'eau ou l'oxygène) ; pour la stabilité thermodynamique, un niveau inférieur à –4.9 eV est requis. La conductivité du PBDF varie entre 12 et 2100 S/cm selon la teneur en acétate de cuivre [12], soit plus de neuf ordres de grandeur au-dessus de celle du P3HT. Dans ce travail, il est utilisé en solution dans du diméthylsulfoxyde (DMSO) à une concentration de 7 mg/mL. Sa masse molaire est de 186.12 g/mol.

3.1.4 Mécanisme de dopage entre P3HT et PBDF

L'alignement énergétique entre le HOMO du P3HT et le LUMO du PBDF — dans la distribution statistique des niveaux d'orbitales — rend possible un transfert de charge entre ces deux polymères. Ce mécanisme de transfert d'électrons est représenté schématiquement dans la Figure 5.

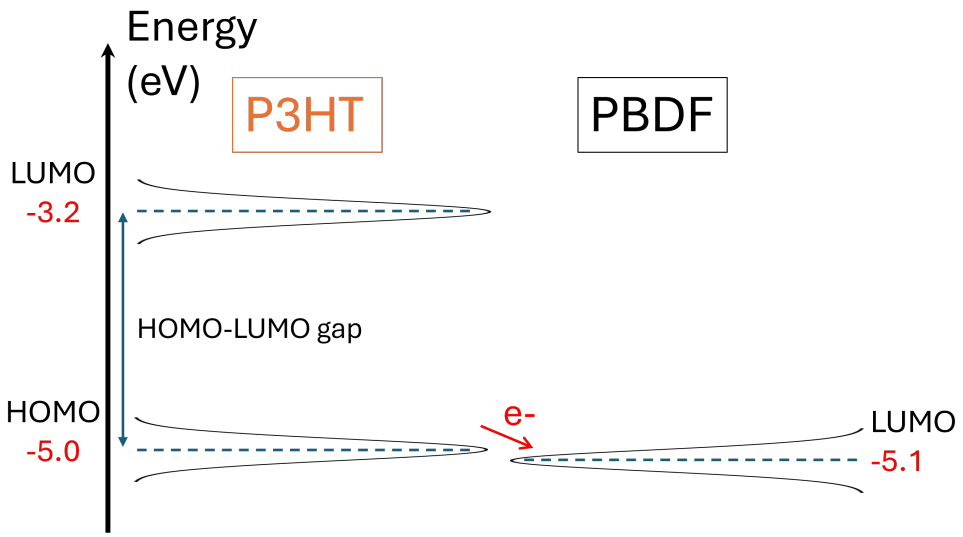

FIGURE 5 Représentation des orbitales énergétiques HOMO et LUMO du P3HT et du PBDF l'une par rapport à l'autre. Si les deux polymères sont rapprochés suffisamment, la barrière potentielle entre eux devient infiniment petite, ce qui rend théoriquement possible la circulation des électrons entre les orbitales HOMO du P3HT et LUMO du PBDF.

3.2 Boîte à gants

Une boîte à gants (modèle "Universal") de Vacuum Technology Inc. (VTI) est utilisée dans cette étude afin de fournir un environnement contrôlé, isolé de l'air ambiant. Le système fonctionne à une pression équivalente à 1/1000 de la pression atmosphérique et maintient une atmosphère quasi pure d'azote, avec des concentrations très faibles en eau et en oxygène—inférieures à 0.01 ppm dans des conditions normales. Cela garantit des conditions propres, anhydres et anaérobiques constantes pour tous les échantillons, empêchant toute interaction avec l'humidité ou l'oxygène.

3.3 Mélange et dépôt par goutte à goutte des polymères

Dans cette étude, le P3HT est dopé avec du PBDF par mélange des deux polymères en solution, l'ensemble du processus étant réalisé dans la boîte à gants. Le P3HT solide est d'abord dissous dans du chloroforme à une concentration de 5 mg/mL, puis agité pendant au moins 30 minutes pour obtenir une solution homogène. Ensuite, un volume défini de cette solution de P3HT est transféré dans un second flacon pour le mélange. Une quantité prédéfinie de PBDF—déjà dissoute dans du diméthylsulfoxyde (DMSO)—est ajoutée pour atteindre le taux de dopage souhaité. Le mélange final est ensuite agité pendant au moins 30 minutes supplémentaires afin d'assurer une homogénéité complète.

Après le mélange, la solution polymère est déposée par goutte à goutte sur des contacts en or pour la caractérisation électrique et thermoélectrique. La solution est appliquée en plusieurs couches superposées. Pour les mesures du coefficient de Seebeck, trois couches de 10 µL chacune sont appliquées. Pour les mesures de conductivité, cinq couches de 10 µL sont utilisées, car la zone active est environ deux fois plus grande.

3.4 Dépôt métallique par faisceau d'électrons

Tous les contacts électriques sont réalisés par dépôt sous vide par faisceau d'électrons (e-beam), à l'aide du système AXXIS de Kurt J. Lesker. Chaque cycle de dépôt utilise un support d'échantillon de 6 pouces, chargé avec six lames de verre. Ces lames sont montées sur une plaque métallique magnétique, avec des masques d'ombrage de précision, maintenus en place par de petits aimants.

Dans le procédé e-beam, des électrons sont émis par un filament chauffé, puis accélérés par un champ électrique intense dans un champ magnétique, où ils sont déviés par la force de Lorentz pour suivre une trajectoire courbe. Ces électrons frappent la surface de l'alliage métallique cible (Cr ou Au), lui transférant de l'énergie jusqu'à ce que le métal chauffe et commence à s'évaporer. Le métal vaporisé s'élève et se condense au contact de la surface plus froide du substrat, formant un film uniforme [32].

Pour chaque dépôt, une couche d'adhésion de 5 nm de chrome (Cr) est d'abord déposée, suivie d'une couche d'or (Au) de 50 ou 100 nm. Le chrome est utilisé en raison de sa forte

affinité pour l'oxygène, ce qui permet une bonne liaison avec le substrat en verre de type SiO_2 [33, 34]. Cette couche d'adhésion améliore la stabilité et la performance globale des contacts en or, qui autrement adhèrent mal en raison de la nature chimiquement inerte de l'or.

3.5 Mesures de la conductivité électrique

La conductivité électrique σ est l'inverse de la résistivité ρ, définie par,

$$\rho = R \cdot \frac{A}{l} \tag{0.22}$$

où R est la résistance, A la section transversale et l la longueur de l'échantillon [35]. La conductivité est donc donnée par :

$$\sigma = \frac{1}{R} \cdot \frac{l}{A} \tag{0.23}$$

En raison de la nature hétérogène des films déposés par goutte à goutte, des valeurs effectives de W, L et t (largeur, longueur et épaisseur) sont utilisées. Compte tenu de la formule de la résistance ohmique $R = \frac{V}{I}$, la conductivité d'un matériau en ce qui concerne la détection à quatre sondes est définie comme suit :

$$\sigma = \frac{I}{V}\frac{L}{W \cdot t} \tag{0.24}$$

Une méthode à quatre pointes est appliquée pour mesurer précisément la conductivité. Le courant est injecté via les contacts extérieurs, tandis que la tension est mesurée entre les contacts intérieurs, éliminant ainsi la résistance de contact [36]. Les contacts en or sont déposés par évaporation sous faisceau d'électrons sur des substrats en verre et en silicium. Le schéma de ce montage est présenté dans la figure 6.

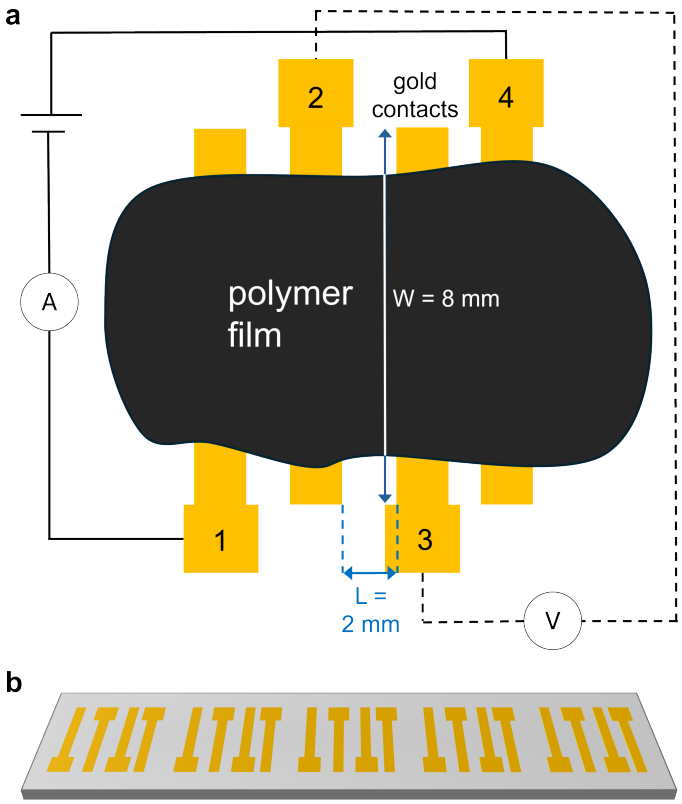

FIGURE 6 **a** Schéma du dispositif de mesure à quatre sondes sur une lame de verre. Entre les contacts 1 et 4, un courant de détection est appliqué, tandis que le gradient de tension est mesuré entre les contacts 2 et 3. L représente la longueur du canal et W la largeur du canal. **b** montre cinq jeux de contacts en or déposés pour le montage sur une lame de verre.

3.6 Méthode de mesure du coefficient de Seebeck

Le coefficient de Seebeck est mesuré en induisant un gradient de température à travers le polymère à l'aide d'une bobine chauffante en or. Un courant (jusqu'à 300 mA) génère un échauffement par effet Joule, créant ainsi une différence de température progressive le long du film polymère, due à la faible conductivité thermique du verre comparée à celle de l'or ($\kappa_{glass} = 0.8$ $Wm^{-1}K^{-1}$, contre $\kappa_{gold} = 314$ $Wm^{-1}K^{-1}$). La tension thermoélectrique induite est mesurée à l'aide d'un appareil Keithley 2636B SMU, tandis que la différence de température est relevée par des thermocouples de type K. La puissance de chauffage est augmentée par paliers, et la tension est moyennée sur des intervalles stables. Le montage est illustré dans la figure 7.

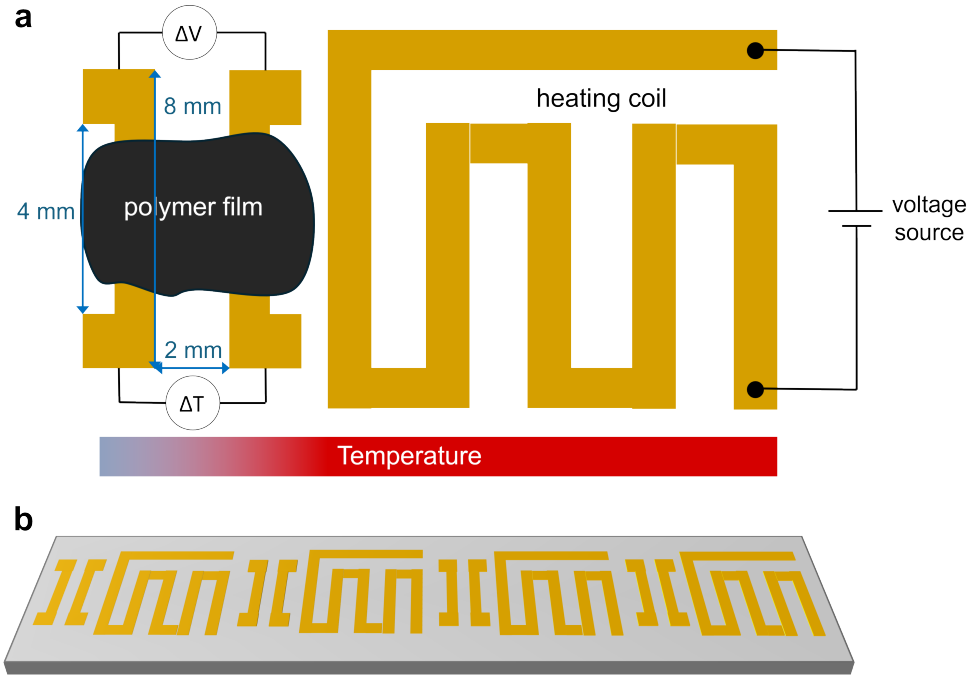

FIGURE 7 Schéma du dispositif de mesure du coefficient Seebeck sur une lame de verre. **a** Une source de tension est fixée aux deux extrémités de la bobine chauffante pour chauffer le côté droit du film polymère. Le gradient de tension généré est mesuré par un SMU Keithley, en même temps que le gradient de température mesuré par un thermomètre avec des thermocouples de type K. **b** montre quatre ensembles de contacts en or déposés pour le montage sur une lame de verre.

3.7 Mesures des transistors à effet de champ (FET)

Deux configurations sont utilisées pour déterminer le type de porteurs de charge et la mobilité dans les polymères étudiés. Les deux reposent sur des substrats en silicium fortement dopés n (n^{++}) avec une couche diélectrique de SiO_2. La première utilise des masques d'ombre pour évaporer les contacts en or, avec un canal de L=2 mm et W=8 mm. La seconde, fournie par le Fraunhofer IPMS, comprend 16 FETs avec électrodes interdigitées et longueurs de canal variables (de 2.5 à 20 µm), chacun ayant une largeur totale de 10 mm. Ces configurations permettent de comparer des dispositifs fabriqués localement avec des dispositifs standardisés (voir figure 8).

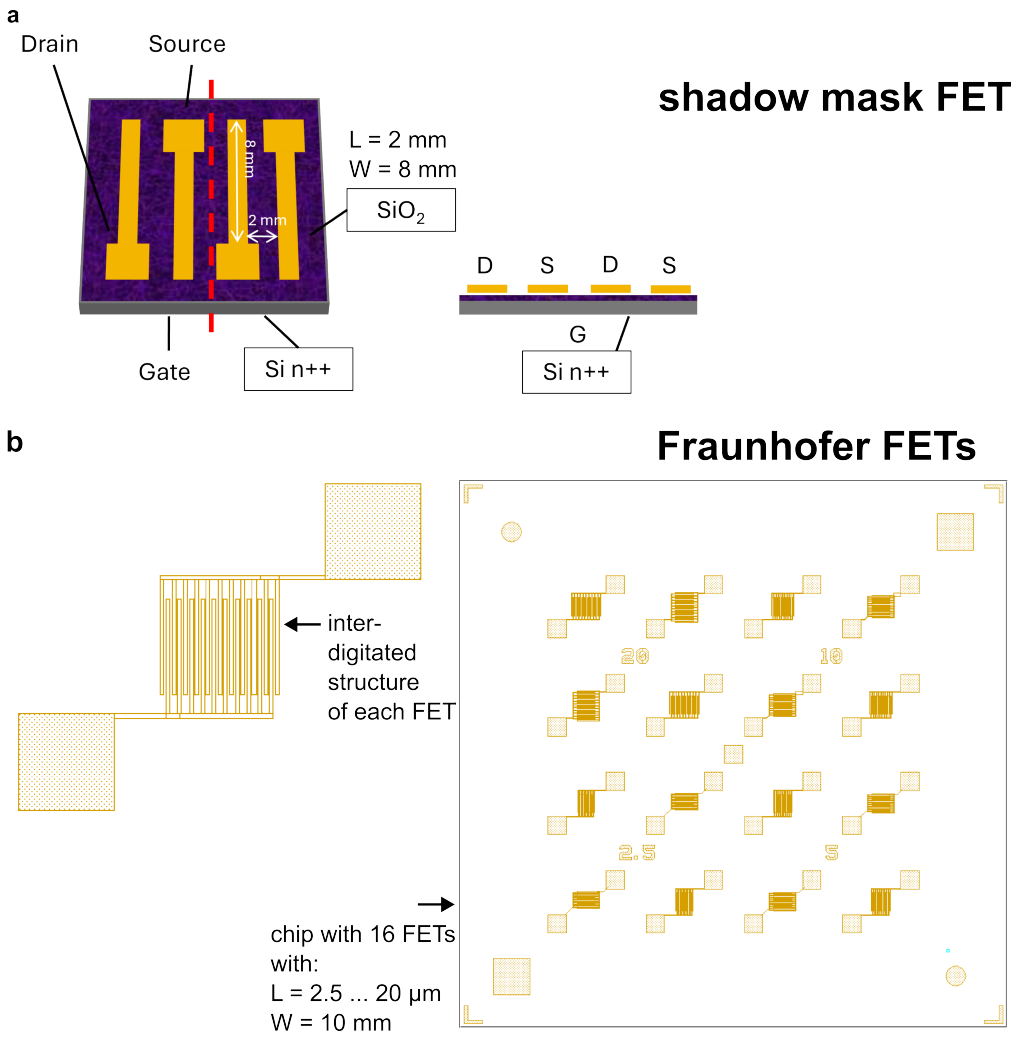

FIGURE 8 **a** montre des transistors à effet de champ (FET) assemblés avec le même masque d'ombre que celui utilisé pour les échantillons de mesure de la conductivité. Des contacts en or, pour la source S et le drain D, d'une épaisseur de 50 nm sont évaporés par faisceau d'électrons sur du Si (gris) fortement dopé n (n^{++}), avec une couche isolante de 285 nm de SiO_2 (violet) sur le dessus. **b** montre un substrat prêt à l'emploi de Fraunhofer. Un substrat de 1.5x1.5 cm^2 comprend 16 FET avec des longueurs de canal variables de 2.5, 5, 10 et 20 µm pour un ensemble de quatre FET chacun. Chaque FET a une largeur de canal cumulée de 10 mm, en raison de la structure interdigitée des électrodes. La couche isolante SiO_2 est plus fine que **a** avec 230 nm.

3.7.1 Traitement de surface au trichlorosilane d'octadécyle (OTS)

L'OTS ($CH_3(CH_2)_{17}SiCl_3$) est utilisé pour améliorer la mobilité à effet de champ et le courant I_{ds} dans les films polymères. Il augmente les liaisons π à l'interface, ce qui améliore les performances jusqu'à 8 fois pour les couches de pentacène [37, 38], et environ 100 fois pour le pérylène [39]. La méthode utilisée suit celle de Wang et Lieberman [40]. Les substrats sont d'abord nettoyés, traités à l'ozone, puis immergés dans une solution d'OTS dans du toluène (5 mmol) à 60°C pendant 1 h, et laissés au repos 48 h dans la boîte à gants. Enfin, ils sont rincés dans du toluène propre et chauffés à nouveau pour éliminer le solvant.

4 Résultats et discussion

Après avoir établi le cadre théorique et méthodologique, ce chapitre aborde les principaux résultats de l'étude. Il présente tous les résultats pertinents obtenus grâce à la topographie de surface optique et mécanique, aux mesures de la conductivité et du coefficient Seebeck et à l'analyse des transistors à effet de champ. Les résultats sont discutés et évalués par rapport à la littérature correspondante et actuelle.

4.1 Analyse de la topographie des films polymères

L'analyse de surface est réalisée par microscopie optique, profilométrie et microscopie à force atomique (AFM). La première méthode est utilisée pour obtenir une vue d'ensemble du P3HT et du PBDF purs, ainsi que des solutions mélangées à l'échelle du millimètre, afin d'analyser la solubilité et la séparation des phases des deux polymères. La profilométrie permet de balayer les films polymères dans une seule dimension, ce qui permet de visualiser la structure de la surface, comme la rugosité et l'homogénéité de l'épaisseur du film jusqu'à l'échelle du nanomètre. La dernière méthode, l'AFM, est utilisée pour obtenir une compréhension plus précise de la topographie du polymère à l'échelle du nanomètre. En particulier, la séparation des phases et l'alignement des amorphes ou des chaînes peuvent être résolus avec une qualité beaucoup plus élevée et différents canaux d'information, par rapport aux autres méthodes.

4.1.1 Images de microscope optique

Des images au microscope ont été capturées afin d'analyser la morphologie de films polymères réalisés à partir de solutions pures et mélangées de P3HT et de PBDF. Les films polymères ont été préparés entièrement dans une boîte à gants, et les observations au microscope ont été effectuées en conditions ambiantes à l'extérieur de celle-ci.

Des films de PBDF avec des concentrations de 7 mg/mL et 3.5 mg/mL ont été préparés, cette dernière concentration ayant été obtenue en diluant la solution d'origine avec du DMSO afin de la réduire de moitié. Les deux films ont été déposés par cinq gouttes successives de 10 µL, pour un total de 50 µL, conformément à la procédure utilisée pour les échantillons standard déposés par dépôt à la goutte. Dans les deux cas, de nombreuses particules solides de tailles comprises entre 90 et plus de 300 µm sont visibles.

En revanche, les films de P3HT à 5 mg/mL ne présentent pas les mêmes types de particules solides ; seules quelques petites taches noires, de quelques micromètres de taille, sont observables, probablement dues à une contamination survenue après la préparation.

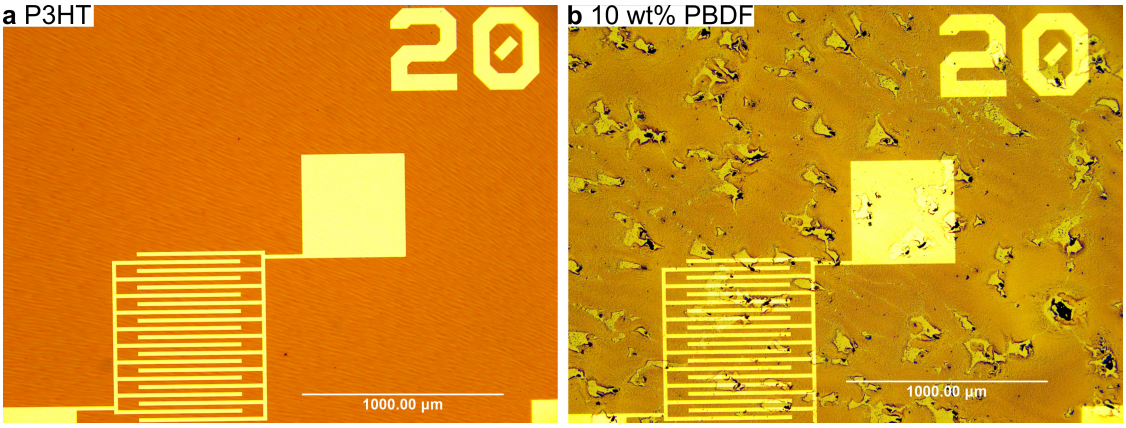

FIGURE 9 Comparaison entre les échantillons de FET enrobés par centrifugation à 3000 rpm pendant 60 s. L'échantillon **a** est un revêtement de P3HT pur, l'échantillon **b** est une solution dopée au PBDF à 10 wt%. Les particules noires sont des paillettes de PBDF non dissoutes.

La Figure 9 compare deux films réalisés par l'enduction centrifuge sur des substrats du Fraunhofer, avec une rotation de 3000 rpm pendant 60 s. La sous-figure **a** montre un revêtement uniforme de P3HT pur, tandis que la sous-figure **b** présente un échantillon dopé contenant 10% en poids de PBDF. Ce dernier montre la présence de flocons de PBDF non dissous, similaires aux grosses particules observées dans les échantillons de PBDF déposés par dépôt à la goutte, ce qui indique une dissolution incomplète ou une agrégation lors du processus de l'enduction centrifuge.

4.1.2 Profilométrie

Pour déterminer l'épaisseur du film t, paramètre essentiel pour le calcul de la conductivité électrique σ, une mesure de profilométrie a été réalisée à l'aide du profilomètre Ambios XP2, qui offre une résolution latérale de 100 nm et applique une force de 10 mg. Comme c'est typique pour le dépôt à la goutte, les profils montrent une courbure depuis le centre jusqu'aux bords [41], ainsi que de nombreuses inhomogénéités. La majorité des variations d'épaisseur se situent à l'échelle du micromètre et sont dues à la rugosité intrinsèque de surface induite par la méthode de dépôt. Les irrégularités plus importantes—jusqu'à dix micromètres—sont probablement causées par des particules de poussière ou autres contaminants, en particulier puisque les échantillons ont dû être transportés hors de la boîte à gants et entre laboratoires, augmentant ainsi le risque de contamination.
Les résultats montrent une forte variabilité, certaines barres d'erreur dépassant 100% de la valeur moyenne, ce qui est cohérent avec les irrégularités de surface observées. L'épaisseur moyenne mesurée sur l'ensemble des échantillons était de 1773.25 nm.

4.1.3 Microscopie à force atomique (AFM)

La microscopie à force atomique (AFM) a été réalisée à l'aide de leviers en silicium dopé au n-antimoine, recouverts d'aluminium (modèle TESPAW-V2 de Bruker), mesurant 127 µm de long, 35 µm de large, avec une constante de raideur de 42 N/m. Les balayages ont été effectués à une vitesse lente (0.977 Hz) afin de maximiser la résolution, en ciblant des zones de 2×2 µm^2 sur des substrats Fraunhofer recouverts par l'enduction centrifuge. Chaque image a été prise sur un substrat distinct, avec des balayages AFM effectués entre les électrodes interdigitées des transistors à effet de champ (FET), en évitant les amas noirs visibles de PBDF. Les profils de hauteur ont été corrigés pour l'inclinaison à l'aide d'un ajustement de plan d'ordre 1 suivi d'un aplatissement d'ordre 1.

Les balayages ont montré que le film de P3HT pur présente une surface uniformément recouverte, tandis que les échantillons dopés en PBDF (à partir de 1% en poids) présentent des amas sombres de particules de PBDF non dissoutes, également visibles au microscope optique. Ces flocons ont tendance à s'accumuler entre les électrodes interdigitées et peuvent provoquer des courts-circuits électriques. Parmi les concentrations testées, le mélange à 15% en poids de PBDF présente la meilleure morphologie, avec des grains plus nombreux et uniformément répartis, ce qui indique un meilleur mélange des deux polymères. En revanche, l'échantillon à 25% présente des particules plus grandes et plus irrégulières, ce qui suggère une séparation de phase et un mélange moins homogène. Ces observations sont visibles dans la Figure 10.

Des balayages AFM supplémentaires ont été effectués directement sur les flocons sombres de PBDF. Ces régions présentent des surfaces nettement plus rugueuses — jusqu'à 200 fois plus élevées en hauteur mesurée que les zones planes — suggérant une possible dégradation de la pointe lors du balayage. Malgré cela, les images des erreurs de force maximale révèlent des détails supplémentaires, confirmant que les échantillons à 15% présentent des caractéristiques de surface plus homogènes que ceux à 1% et 25%.

Les valeurs de rugosité quadratique moyenne (R_q) calculées viennent appuyer ces observations. Entre les électrodes, tous les échantillons présentent des valeurs faibles similaires autour de 0.3 nm (à l'exception du 1%, légèrement plus élevé en raison d'anomalies). En revanche, sur les flocons de PBDF, la rugosité augmente fortement : 18.8 nm pour 15%, 37.1 nm pour 1%, et plus du double avec 72.0 nm pour 25%. Ces résultats suggèrent que le mélange contenant 15% de PBDF produit la morphologie de film la plus homogène parmi les échantillons testés.

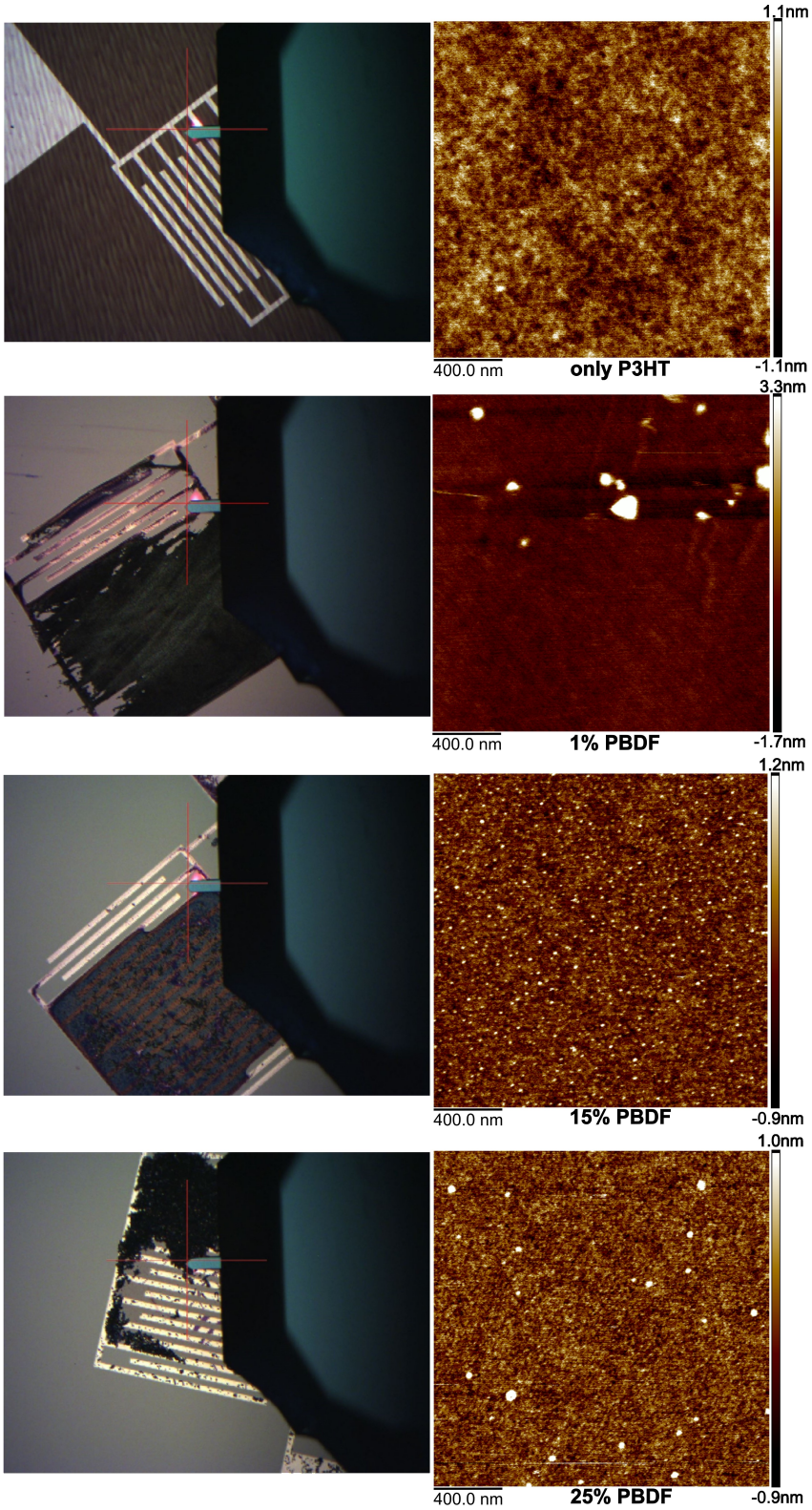

FIGURE 10 La partie gauche montre les positions de la pointe AFM pour les polymères respectifs. Le balayage pour 25% en poids a été effectué à l'extérieur de la couche noire, pas exactement à la position indiquée. La partie droite montre les profils de hauteur obtenus.

4.2 Évaluation thermoélectrique

4.2.1 Évaluation de la conductivité électrique

La conductivité électrique des films de P3HT dopés au PBDF a été évaluée en utilisant plusieurs échantillons déposés par dépôt de gouttes pour chaque wt%, en raison de la forte variabilité de l'uniformité du film et de la qualité des contacts. Les mesures I–V (Figure 11) montrent que, jusqu'à 25 wt%, la polarité du courant s'inverse entre tensions positives et négatives, avec une conductivité plus élevée près de zéro volt et plus faible aux tensions plus importantes. À 20 – 25 wt%, les pentes deviennent plus symétriques des deux côtés, indiquant l'apparition d'un comportement ohmique, qui est complètement observé pour 50 wt% et pour le PBDF pur. Globalement, la conductivité augmente progressivement avec la teneur en PBDF et se stabilise à 100 wt% (PBDF pur).

À titre de comparaison, le P3HT pur présente une conductivité d'environ 6.78nS/cm à 293.2K [31], soit 22 à 30 fois inférieure aux valeurs mesurées dans cette étude, bien que les valeurs issues de la littérature aient été obtenues par des mesures en paliers de courant plutôt que par balayages en tension. La conductivité du PBDF pur est rapportée à 2100 S/cm, avec des dimensions comparables pour une configuration à quatre sondes, selon l'étude originale de Tang et al. [42], soit environ 10 fois plus élevée. Il est intéressant de noter que pour les monocouches appliquées par centrifugation d'une épaisseur de 17 à 19 nm, la conductivité se situe entre 3100 et 3800 S/cm selon Ke et al. [12]. De plus, la conductivité augmente considérablement jusqu'à 6100 S/cm pour cinq couches empilées dans l'étude. Étant donné que les films déposés par dépôt de gouttes sont significativement plus épais — de l'ordre de plusieurs micromètres contre quelques dizaines ou centaines de nanomètres pour les films appliquée par centrifugation — on pourrait s'attendre à une conductivité plus élevée. Cependant, le dépôt de gouttes induit une forte variabilité de la morphologie et de l'épaisseur due à l'évaporation incontrôlée du solvant et aux facteurs humains (angle et hauteur de dépôt), entraînant des propriétés électriques et structurales non uniformes et une reproductibilité réduite. En revanche, le dépôt à la tournette permet la formation de films homogènes dans des conditions bien contrôlées, améliorant ainsi la reproductibilité et la comparabilité.

Ces observations sont corroborées par Na et al. (2015) [43], qui ont rapporté des erreurs standard de mobilité de 11 – 25% pour les films déposées par revêtement par centrifugation, contre 72% pour les films déposés par dépôt de gouttes. En outre, des temps de rotation plus courts (3 s contre 60 s) ont conduit à un ordre cristallin significativement plus élevé, démontré par diffraction des rayons X en incidence rasante bidimensionnelle (2D GIXD), entraînant des mobilités plus élevées (0.011–0.015cm^2/Vs contre 0.002–0.004cm^2/Vs). Les films drop-castés, en revanche, ont montré une plage de mobilité encore plus large allant de 0.002 à 0.019 cm^2/Vs.

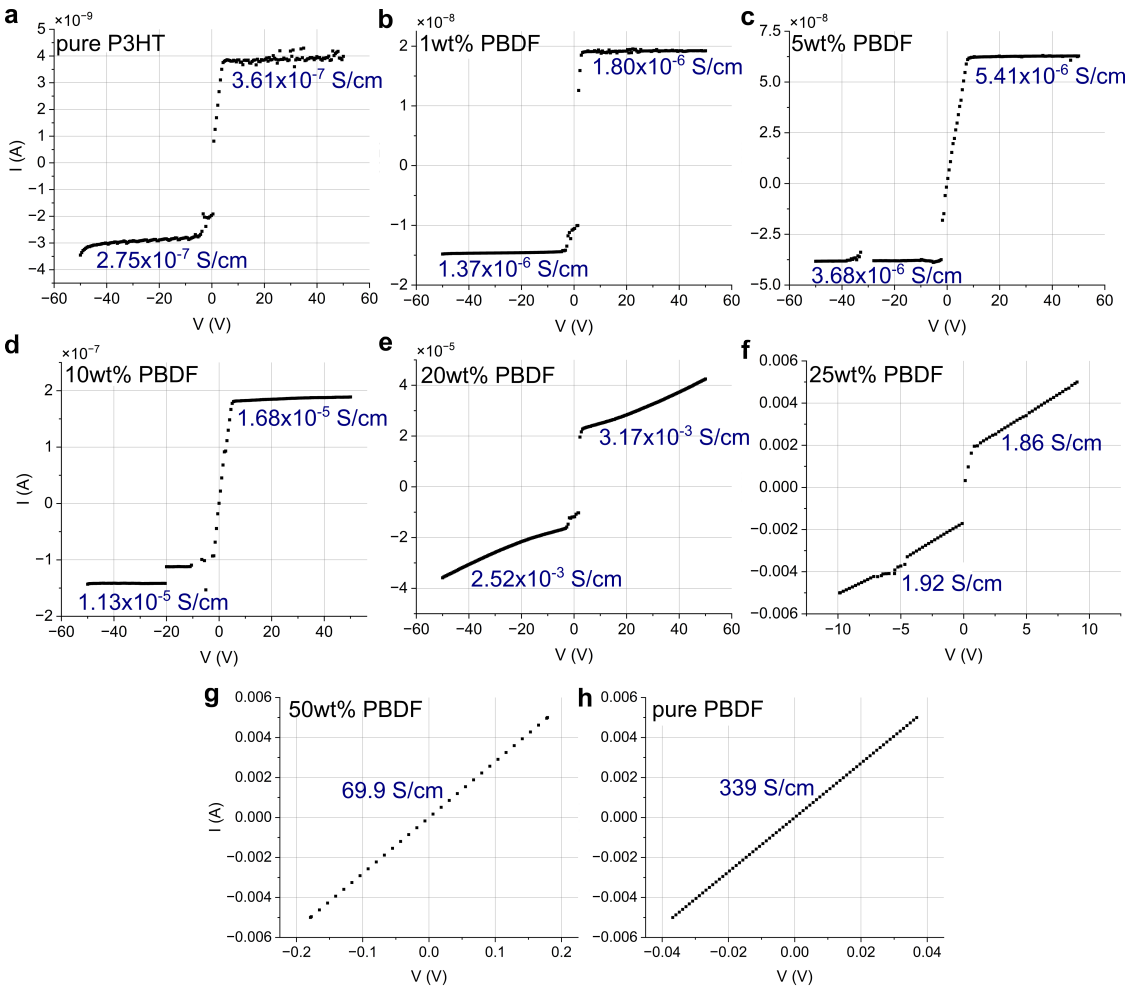

FIGURE 11 Comparaison des mesures I-V de solutions mélangées pour tous les pourcentages de poids testés de P3HT dopé au PBDF, du P3HT pur au PBDF pur. On essaie de maintenir la plage de tension entre -50 et 50 V, bien qu'elle doive être réduite si le courant atteint la limite fixée de 5 mA, comme c'est le cas pour 25 wt% et plus.

4.2.2 Évaluation du coefficient Seebeck

Les mesures du coefficient Seebeck S ont nécessité plusieurs échantillons par wt% de PBDF en raison de la sensibilité du dispositif. Les tests ont été réalisés sur une table optique afin de réduire les vibrations. Les résultats (Figure 12) montrent que $|S|$ diminue fortement de 160.6 µV/K à 1 wt% à 18.4 µV/K à 5 wt%, puis se stabilise autour de 20 – 27 µV/K jusqu'à 32 wt%. Le PBDF pur présente $|S|$ =14.9 µV/K, proche des valeurs rapportées (21 µV/K). Seuls les échantillons à 1 wt% et 5 wt% affichent une pente positive, indiquant un comportement de type p, tandis qu'à partir de 10 wt%, la pente devient négative, caractéristique d'une conduction de type n. La valeur de Seebeck du P3HT n'a pas pu être mesurée (signal bruité), bien que la littérature rapporte environ 1550 µV/K.

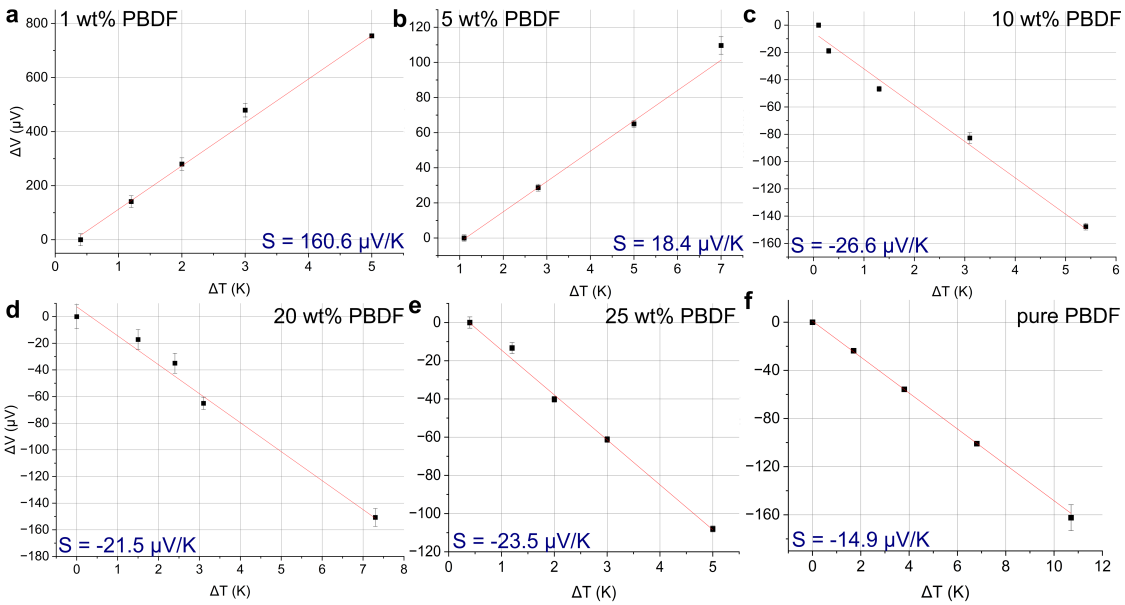

FIGURE 12 Ensemble des résultats des mesures du coefficient Seebeck S pour tous les pourcentages de poids testés de PBDF dopé au P3HT. Les pourcentages en poids de PBDF de 1 et 5 présentent une pente positive, comme prévu pour les matériaux de type p, tandis que tout pourcentage testé supérieur entraîne une pente négative, comme prévu pour un matériau de type n tel que le PBDF.

4.2.3 Résultats globaux pour la conductivité électrique, le coefficient Seebeck et le facteur de puissance

La Figure 4.11 présente les valeurs mesurées de la conductivité électrique σ, du coefficient Seebeck S et du facteur de puissance PF pour les mélanges de P3HT dopés avec du PBDF. La conductivité augmente progressivement avec la teneur en PBDF et se stabilise à mesure que la composition se rapproche du PBDF pur, avec une augmentation totale de plusieurs ordres de grandeur par rapport au P3HT pur. Les mesures effectuées pour les courants positifs et négatifs montrent des différences négligeables, de sorte que le PF a été calculé à partir des valeurs légèrement plus élevées du côté positif.
Bien que $PF = \sigma S^2$, l'effet dominant de l'augmentation de σ entraîne une hausse du facteur de puissance, malgré la relative stabilité de S après une baisse initiale de 160 µV/K (à 1 wt%) à 20 – 27 µV/K à partir de 5 wt%. Cette diminution de S correspond à une augmentation du dopage et à un déplacement du niveau de Fermi, comme décrit par, [23, 25]

$$S = -\frac{k_B}{e} \int \frac{E - E_F}{k_B T} \frac{\sigma'(E)}{\sigma} dE \tag{0.25}$$

où une concentration accrue de porteurs réduit $E - E_F$, ce qui diminue la thermopouvoir. [44] De manière empirique, des études antérieures rapportent $S \propto \sigma^{-1/4}$ et $PF \propto \sigma^{1/2}$ pour les systèmes organiques p- et n-type [25, 29, 45].

Deux régimes de conduction sont observés : la conduction de type p domine jusqu'à environ 5 wt% de PBDF, puis passe au type n à partir de 10 wt%. Cette transition coïncide avec une augmentation de la conductivité de deux ordres de grandeur en dessous de 10 wt%, contre près de cinq ordres au-dessus de ce seuil. À 1 wt%, un effet de dopage dans le P3HT est probablement responsable du PF le plus élevé dans la zone à faible PBDF, en raison d'une σ élevée et d'un S encore important. Les mesures FET présentées dans la section suivante confirment cet effet de dopage. Enfin, le fort contraste entre le P3HT pur ($S \approx 1550$ µV/K) et le PBDF ($S \approx 15$ µV/K) est cohérent avec leurs structures électroniques respectives, où une conductivité plus élevée correspond à une différence moyenne d'énergie des porteurs par rapport au niveau de Fermi plus faible [42, 46].

4.3 Analyse des transistors à effet de champ (FET)

Les caractéristiques I–V des FETs à base de P3HT et dopés avec PBDF ont été analysées pour des dispositifs fabriqués avec des masques d'ombre (canal de 2 mm) et des substrats Fraunhofer, en comparant les films obtenus par dépôt de gouttes, et par dépôt à la tournette. Le dépôt goutte-à-goutte a donné des résultats peu fiables, en raison soit de courants drain-source très faibles (< 1 nA) causés par un mauvais contact des pointes de mesure—en particulier lorsque les électrodes étaient entièrement recouvertes de polymère—soit de courants de fuite où $I_{ds} \approx I_g$, suggérant des courts-circuits à travers la couche diélectrique de grille. Par conséquent, les valeurs de I_{ds} issues des échantillons en dépôt goutte-à-goutte ne pouvaient pas représenter de manière fiable le transport intrinsèque dans le canal.

En revanche, le dépôt à la tournette a permis d'obtenir des films homogènes et des performances reproductibles. Tous les échantillons ont été prétraités avec de l'OTS pour améliorer la cohérence. Les courbes de transfert I_{ds}–V_{gs} pour le P3HT pur et pour 1 wt% de PBDF (Figure 13) montrent un comportement typique de FET p-type, avec une modulation de grille principalement visible à des valeurs négatives de V_{gs}, en accord avec la littérature [47, 48]. Le courant I_{ds} augmente lorsque la longueur de canal diminue (de 20 à 5 µm) en raison d'une résistance plus faible : par des facteurs d'environ 2.9 et 9.2 pour le P3HT, et 10 et 32 pour les échantillons dopés au PBDF. À chaque longueur de canal, le dopage au PBDF améliore significativement le courant (par exemple, 7.5 fois pour $L = 10$ µm), étend le régime linéaire et retarde la saturation par rapport au P3HT non dopé.

Les mobilités extraites dans la région linéaire (Table 1) confirment cette tendance : pour $L = 5$–10 µm, les dispositifs dopés au PBDF présentent des mobilités 5 à 10 fois supérieures à celles du P3HT pur, bien que les valeurs globales ($\sim 10^{-3}$–10^{-2} $cm^2V^{-1}s^{-1}$) restent un ordre de grandeur inférieur à celles rapportées par Wang et al. (2003) [48], mais comparables aux premiers travaux de Bao et al. (1996) [47].

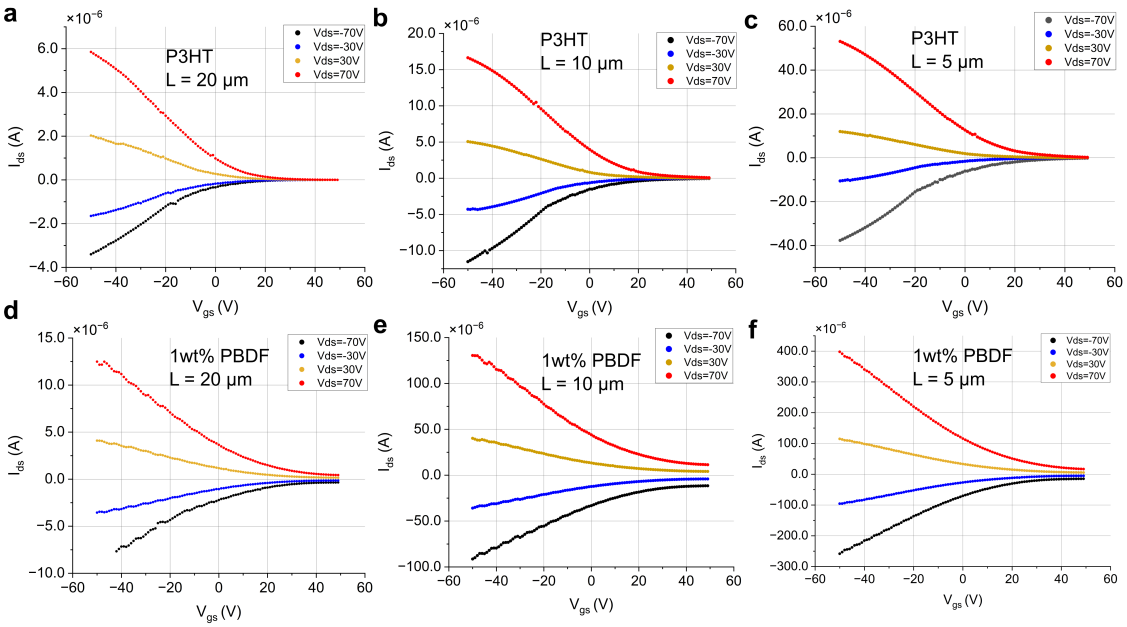

FIGURE 13 I_{ds}-V_{gs} avec une V_{ds} constante. I_{ds}-V_{gs} balayages avec des niveaux V_{ds} constants de P3HT et 1 wt% enrobés de spin. PBDF, pour des longueurs de canal de 5, 10 et 20 µm. Chaque couleur représente une valeur différente de V_{ds}. Les dispositifs avec 1 wt% PBDF atteignent un I_{textds} plus élevé que leurs homologues P3HT et ne montrent pas encore de comportement de saturation pour V_{textgs} = -50 V. Les mobilités de ces courbes sont indiquées dans le tableau 1.

Les rapports on/off (Table 2) chutent fortement après ajout de PBDF : tandis que I_{on} augmente modérément (jusqu'à 7.8 fois), I_{off} croît de plus de deux ordres de grandeur, réduisant les rapports de >3500 (P3HT, L = 20 µm) à 28 (dopé PBDF). Les tensions seuil (V_{Th}) se déplacent vers des valeurs plus positives avec le dopage, indiquant un déplacement du niveau de Fermi vers le HOMO du P3HT et nécessitant un biais de grille positif plus fort pour dépléter les porteurs de type p. Ces tendances suggèrent un dopage efficace via l'injection de porteurs libres supplémentaires, mais également une augmentation des courants de fuite.

TABLE 1 Mobilités linéaires μ_{lin} des échantillons FET avec P3HT pur et 1 wt% PBDF sur deux substrats Fraunhofer distincts pour des tensions V_{textds} de -70 à 70 V et des longueurs de canal de 5, 10 et 20 µm.

	P3HT	**1 wt% PBDF**
en $cm^2V^{-1}s^{-1}$	**5 µm**	
μ_{lin}(-70 V)	0.00399	0.03746
μ_{lin}(-30 V)	0.00243	0.03304
μ_{lin}(30 V)	0.00245	0.03795
μ_{lin}(70 V)	0.00430	0.05663
	10 µm	
μ_{lin}(-70 V)	0.00242	0.01112
μ_{lin}(-30 V)	0.00208	0.01072
μ_{lin}(30 V)	0.00207	0.01300
μ_{lin}(70 V)	0.00274	0.01789
	20 µm	
μ_{lin}(-70 V)	0.00229	0.00291
μ_{lin}(-30 V)	0.00232	0.00271
μ_{lin}(30 V)	0.00196	0.00270
μ_{lin}(70 V)	0.00234	0.00367

TABLE 2 Comparaison des valeurs I_{on} et I_{off}, ainsi que de leur rapport I_{on}/I_{off} et de la tension de seuil V_{Th} du P3HT et de 1 wt% PBDF. FETs.

pour V_{ds}=70 V	**P3HT**	**1 wt% PBDF**	**ratio : 1 wt% PBDF/P3HT**
I_{on}	en A		
5 µm	$5.3092 \cdot 10^{-5}$	$3.9794 \cdot 10^{-4}$	7.4952
10 µm	$1.6646 \cdot 10^{-5}$	$1.3049 \cdot 10^{-4}$	7.8391
20 µm	$5.8498 \cdot 10^{-6}$	$1.2488 \cdot 10^{-5}$	2.1349
I_{off}	en A		
5 µm	$2.2385 \cdot 10^{-7}$	$1.6800 \cdot 10^{-5}$	75.0539
10 µm	$7.3913 \cdot 10^{-8}$	$1.1362 \cdot 10^{-5}$	153.7318
20 µm	$1.6626 \cdot 10^{-9}$	$4.3988 \cdot 10^{-7}$	264.5715
I_{on}/I_{off}			
5 µm	237.17	23.68	0.09984
10 µm	225.21	11.48	0.05097
20 µm	3518.44	28.39	0.00807
V_{Th}	en V		
5 µm	12.6	17.5	1.3888
10 µm	12	21	1.75
20 µm	10.2	16.4	1.6078

Pour des concentrations de PBDF plus élevées ($\geq$10 wt%), la plupart des dispositifs perdent le contrôle par la grille et présentent un comportement I_{ds}–V_{gs} de type ohmique, attribué à l'accumulation de flocons de PBDF reliant les électrodes interdigitées (Figure 14). Parfois, un pontage partiel permet une certaine modulation (Figure 14**e**, mais les performances des FETs se dégradent globalement avec l'augmentation de la teneur en PBDF.

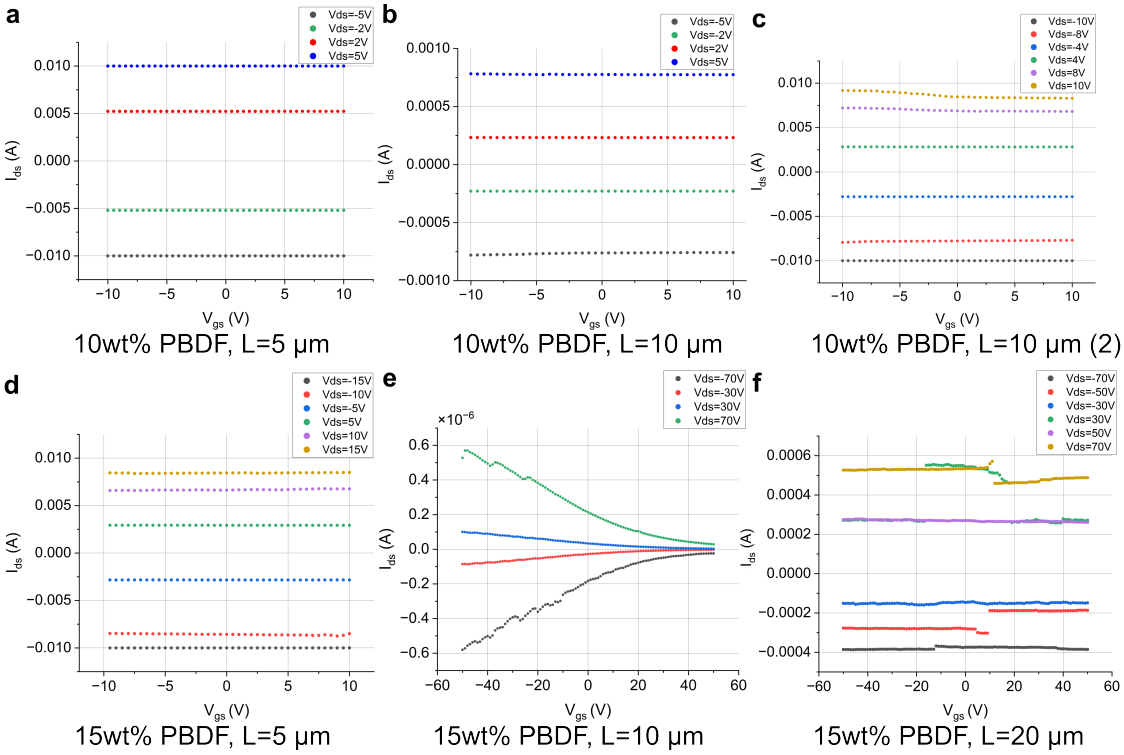

FIGURE 14 I_{ds}-V_{gs} balayages à V_{ds} constants des niveaux 10 et 15 wt% enrobés de spin. PBDF. **a** - **d** et **f** ne montrent aucune modulation du courant de drain lors de l'application d'une polarisation de grille due à l'accumulation de paillettes PBDF dans les interdigits. **e** montre une modulation de I_{ds} en fonction de la V_{gs} appliquée, comme c'est le cas pour les FETs avec seulement P3HT ou 1 wt%. PBDF.

En combinant ces résultats avec ceux de la conductivité et du coefficient Seebeck, le PBDF à 1 wt% améliore considérablement la mobilité et le courant du P3HT tout en maintenant le comportement FET, confirmant son rôle en tant que dopant. Cependant, des teneurs plus élevées en PBDF compromettent la fonctionnalité des dispositifs en raison de courts-circuits causés par les flocons, rendant l'évaluation des performances au-delà de 1 wt% peu fiable avec cette géométrie de FET.

5. Résumé et perspectives

L'objectif de ce travail était d'améliorer le facteur de puissance (PF) du semi-conducteur p-type P3HT par dopage via un mélange avec le conducteur n-type PBDF. Pour les films déposés par dépôt de gouttes sur substrats en verre, le PF a été amélioré d'un facteur de $3 \cdot 10^4$, passant de $2.0 \cdot 10^{-6}$ µWm^{-1}K^{-2} pour le P3HT avec 1 wt% PBDF à 0.06 µWm^{-1}K^{-2} à 25 wt% PBDF, principalement grâce à une augmentation significative de la conductivité électrique σ (de $2.0 \cdot 10^{-7}$S/cm à 1.1 S/cm), tandis que le coefficient Seebeck absolu $|S|$ est resté proche de 22 µV/K, à l'exception de 1 wt% PBDF (160.6 µV/K) et du PBDF pur (14.9 µV/K). L'analyse de σ, S et PF a révélé deux régimes de conduction : p-type jusqu'à 5 wt% et n-type au-delà de 10 wt%. L'augmentation de σ à 1 et 5 wt%, tout en conservant un comportement p-type, confirme un effet de dopage du P3HT.

L'analyse des FET a montré qu'à 1 wt% PBDF, la mobilité linéaire μ_{lin} augmente d'un facteur 5 – 10 par rapport au P3HT pur pour des longueurs de canal de 10 et 5 µm, tandis que des concentrations plus élevées donnent des résultats incohérents ou des réponses ohmiques typiques du PBDF pur. Les dispositifs à 1wt% n'atteignent pas la saturation dans la plage de V_{gs} testée (-50 à 50 V), contrairement au P3HT pur.

Plusieurs améliorations de procédé sont suggérées : pour le dépôt de gouttes, le préchauffage des substrats (30 – 50°C) avant dépôt pourrait éviter le débordement, et il faudrait développer des méthodes permettant un séchage rapide en une seule goutte afin d'améliorer l'homogénéité des films. Pour le revêtement par centrifugation, les problèmes d'homogénéité dans les mélanges avec PBDF nécessitent un meilleur contrôle de la solubilité via une optimisation du solvant, une filtration ou une dilution. Les filtres PVDF (0.2 – 0.45 µm) se sont révélés inadaptés en raison de la grande taille des particules de PBDF. L'ajustement des paramètres de rotation ou la recherche de solvants plus performants que le DMSO pourraient améliorer la qualité des films.

Les travaux futurs devraient se concentrer sur l'optimisation des concentrations de PBDF autour de 1 wt% (où le dopage est le plus efficace) et entre 5 – 10 wt% (pour déterminer le point de saturation), sur l'augmentation du nombre d'échantillons testés, ainsi que sur l'optimisation des protocoles de revêtement par centrifugation (par exemple, des temps de rotation plus courts comme suggéré par Na et al. [43]). De plus, tester des concentrations plus faibles de P3HT proches de 2mg/mL, comme rapporté par Jiang et al. [49], pourrait améliorer les performances des FET.

Contents

List of Figures

List of Tables

List of Acronyms

PF Power Factor.

S Seebeck Coefficient.

μ_{lin} Linear Charge Carrier Mobility.

μ Charge Carrier Mobility.

σ Electrical Conductivity.

zT Figure of Merit.

AFM Atomic Force Microscope.

Au Gold.

Cr Chromium.

e-beam Electron-Beam.

FET Field-Effect-Transistor.

HOMO Highest Occupied Molecular Orbital.

LUMO Lowest Unoccupied Molecular Orbital.

OSC Organic Semiconductor.

OTEG Organic Thermoelectric Generator.

OTS Octadecyltrichlorosilane.

P3HT Poly(3-hexylthiophen-2,5-diyl).

PBDF Poly(3,7-dihydrobenzo[1,2-b:4,5-b']difuran-2,6-dione).

PEDOT:PSS Poly(3,4-ethylenedioxythiophene) polystyrene sulfonate.

TEG Thermoelectric Generator.

wt% Weight Percentage.

1 Introduction

Global warming is one of the greatest challenges of our time. With the increase in electronic devices in everyday life, be it through smartphones, household appliances or modern cars worldwide, the amount of electronic waste and waste heat production is also on the rise. Waste heat is produced in all energy conversion processes, especially industrial heating (for washing, distilling, melting, etc.) as a by-product. [1] It is estimated that more than 60% of the energy generated in power plants and automobiles is lost in form of waste heat [2, 3], which contributes to useless dissipation and environmental pollution.

Thermoelectric generators (TEGs) offer ways to recycle unused heat and make it usable for electrical applications. To date, mainly inorganic materials are used, such as Bi_2Te_3, PbTe, SiGe or $FeSi_2$, thanks to their crystalline nature. This leads to significantly higher electrical conductivity compared to organic materials and their ability to be operated at higher temperatures, which is typically up to 600 K, compared to below 450 K for organics [2,4]. TEGs are characterized by the figure-of-merit zT (see equation 2.19), which should exceed a value of 1 to be considered useful for most applications. State of the art inorganic materials perform with zT values of close to 1 at room temperature, while this value is in the range of 0.4 for organic materials, in case of PEDOT:PSS [4, 5].

Ideal thermoelectric materials require high electric, but low thermal conductivity. The physical disadvantage of crystalline inorganic materials is the fact that an increase of electrical conductivity implies a corresponding increase of thermal conductivity according to the Wiedemann–Franz law. [13] Further downsides with the use of inorganic elements are their scarcity and thus price, environmental impact due to mining and production, as well as the high required processing temperatures, which complicate mass production. In addition, some used elements such as Te, Bi and Pb are toxic. [4,6,7] In this regard, Figure 1.1 shows an example of the periodic table of the elements in a distorted form with colors to illustrate their rarity and point out conflict materials. The more pronounced the red tone, the rarer an element is, to the point where it could be used up in 100 years. As the image shows, most elements used for modern electronics (indicated by a smartphone symbol) have at least limited availability or are seriously scarce, among which are also Bi, Pb and especially Te.

To tackle this, organic-based TEGs (OTEGs) are emerging. They have the advantages of not requiring rare earths, therefore being cheaper to produce, are mechanically flexible and have a low intrinsic thermal conductivity (typically below 1 $Wm^{-1}K^{-1}$ [8]), which boosts their thermoelectric performance. [3, 4]

There are existing prototypes of OTEGs, used in fabric in order to be used for body-heat

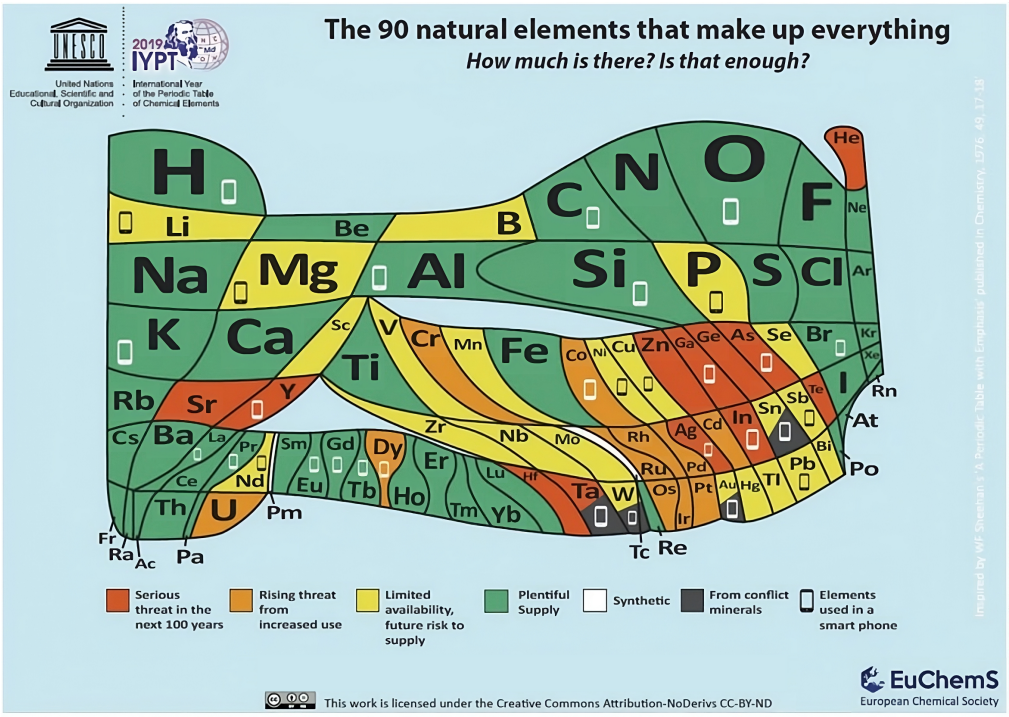

Figure 1.1 Periodic table of elements representing the scarcity of elements in colors from green to red. Conflict materials are marked in grey. All elements with a smartphone symbol are necessary for various smart devices. [6]

harvesting. Textiles, worn directly on the skin, offer an ideal platform for harvesting body heat to generate electricity. Conventional TE materials often suffer from limitations such as structural rigidity and poor processability, making them unsuitable for conforming to curved surfaces like the human body. Conjugated polymers exhibit good compatibility with textile fibres and can be coated onto fabrics, resulting in hybrid thermoelectric materials. [14] This heat can be used as a power source for wearable electronics, such as small medical sensors. A fabricated prototype designed to be scaled up to a power output of 13 µW with alternating legs of n- and p-type, of Na(NiETT) and PEDOT:PSS, was published in 2019 [15].

Nevertheless, the disadvantage of organic TE materials is their lower electrical conductivity and hence, power factor. Typical values for OTE materials are in the range of 100 to 3000 $\mu Wm^{-1}K^{-2}$ [9], compared to up to 10,000 $\mu Wm^{-1}K^{-2}$ at room temperature for the inorganic material NbFeSb [16]. To improve the thermoelectric performance of OTEs, different doping strategies are being researched, such as acid or electrochemical doping, or doping through blending in solution [4]. In this work, the latter method is investigated on example of the frequently used Poly-3-hexylthiophene (P3HT) and the novel Poly-3,7-dihydrobenzo[1,2-b:4,5-b´]difuran-2,6-dione (PBDF), due to to their favourable energy alignment.
These two materials are tested for their electrical conductivity, Seebeck coefficient and thermopower in measurement setups specifically designed for this purpose. In this regard, the

polymers are blended in multiple concentrations of different weight percentages (wt%) to compare their properties. The fabrication includes designing and using shadow masks for thermoelectric characterization, metal evaporation, blending the polymers in a glovebox and depositing them on glass or silicon substrates, for either thermoelectric or field-effect-transistor (FET) characterization. The latter is thereby used to determine the charge carrier type and mobility via the gate-effect.

2 Principles of organic thermoelectrics

This chapter discusses the physical and chemical origin of the electrical and thermal conductivity in organic semiconductors, as well as the principles of doping methods. It furthermore explains the working principle of thermoelectric generators, which are the central devices that this study focuses upon.

2.1 Electronic properties of semiconducting organic materials

Organic semiconductors (OSCs) are materials composed of carbon-based conjugated molecules and polymers that exhibit semiconducting behavior. These materials are fundamentally different from their inorganic counterparts due to their unique molecular structures and bonding characteristics. Although they possess semiconducting properties, the electrical conductivity of OSCs is typically quite low, which can limit their suitability for practical electronic applications. This limited conductivity arises primarily from relatively wide band gaps and the weak van-der-Waals forces that hold the molecules together.

Depending on their electronic structure, OSCs can exhibit p-type, n-type or ambipolar behavior, determined by their intrinsic tendency to donate or accept electrons. The backbone of these materials features alternating single and double bonds, forming a conjugated system with sp^2-hybridized carbon atoms. In this structure, the sp^2 orbitals participate in σ-bonds, while the unhybridized p_z orbitals form delocalized π-bonds. The number of π-electrons and the extent of π-orbital overlap within the polymer play a critical role in defining its electronic properties, including ionization potential, electron affinity, and the energy gap between the highest occupied molecular orbital (HOMO) and the lowest unoccupied molecular orbital (LUMO). Several key parameters are used to describe the electronic behavior of OSCs. The ionization energy (IE) refers to the energy required to remove an electron from the HOMO level. Conversely, the electron affinity (EA) is the energy released when an electron is added to the LUMO, forming a negatively charged state. Another important concept is the density of states (DOS), which defines the number of electronic states available at each energy level. In general, conjugated molecules are characterized by lower ionization potential and higher electron affinities compared to their non-conjugated counterparts [50], contributing to their semiconducting nature. Figure 2.1 visualizes all the mentioned quantities and energy levels, as well as the positions of σ- and π-bonds for two carbon atoms and π-π interaction between polymer chains. [17]

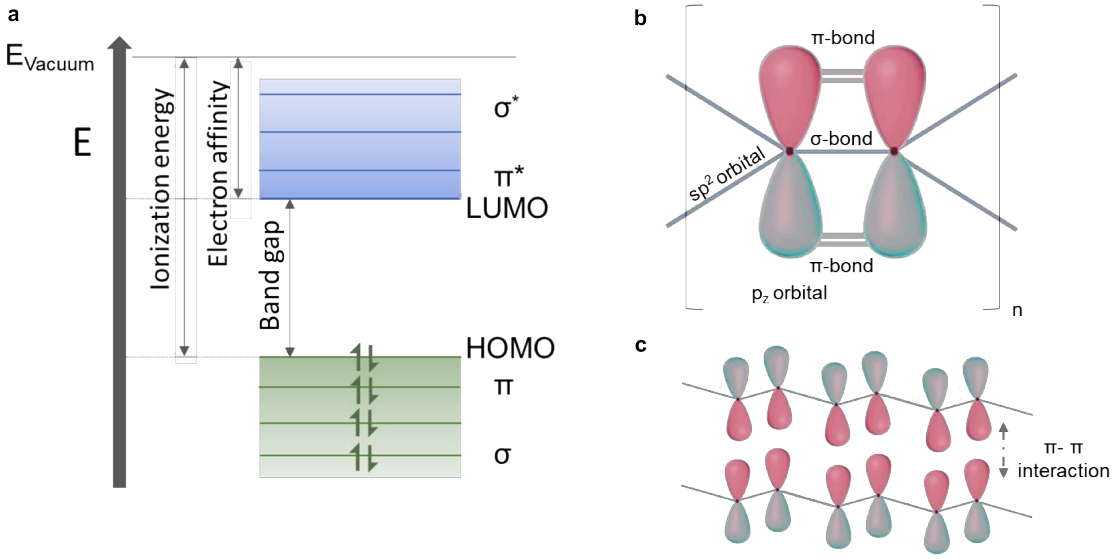

Figure 2.1 Visualization of σ- and π-bonds for carbon atoms and polymer chains. **a** shows the the positions of ionization energy, electron affinity and band gap with respect to the occupied molecular orbitals up to the highest one (HOMO) and the unoccupied molecular orbitals, starting with the lowest (LUMO). σ and π refer to the binding orbitals, contrary to the antibinding orbitals σ* and π*. **b** represents the different positions of σ- and π-bonds in the p_z-orbital between two carbon atoms and the adjacent sp^2-orbitals. **c** continues this constellation for longer polymer chains, additionally pointing out π-π interaction between chains. [17]

In thin films of OSCs, intermolecular charge transfer is observed due to the overlap of electronic wave functions between adjacent molecules. Delocalized π-orbitals along the polymer chain or organic molecule is important to increase intramolecular charge transport. [18] The efficiency of charge transport is influenced by the length of the conjugated chains. Longer chains tend to enhance charge mobility due to increased long-range order and hence, a continuous pathway for charge carriers. However, they can also introduce challenges such as molecular entanglement, which may create structural defects and hinder efficient charge transport. [17, 19] To optimize charge carrier transport in OSCs, several design strategies can be employed. These include engineering the molecular structure, adjusting molecular weights, tailoring the band gap, and modifying solubility through the incorporation of side chains. Such modifications can directly impact the molecular organization and, consequently, the electronic properties of the material. [51]

A key interaction promoting molecular order is π-π stacking between aromatic rings, which stems from weak van-der-Waals forces. Despite this, OSC films typically exhibit a low degree of crystallinity, with structural defects and impurities that inhibit band-like transport. These imperfections create localized electronic states, known as traps, which limit charge mobility.

Overall, charge transport in organic semiconductors is a complex phenomenon that involves interactions on multiple scales, including intramolecular, intermolecular, and intergrain levels. Transport between grains, often referred to as hopping, further complicates the conduction mechanism, underscoring the importance of molecular and structural design in the development of efficient organic semiconductors.

2.1.1 Doping mechanisms in organic semiconductors

The electrical conductivity of OSCs is primarily governed by two factors: the concentration of charge carriers and the efficiency with which these carriers are transferred through the material. One of the most effective methods for enhancing conductivity is doping, which can raise conductivity values up to 10^4 S/cm. [17] However, achieving efficient and precisely controlled doping remains a significant challenge for electronic applications, as it requires fine-tuning the interactions between dopant molecules and the host semiconductor matrix. Dopant-OSC interactions have a profound impact on the energy levels of the molecules within the solid state. These interactions are highly dependent on both the spatial distance and the mutual orientation of the dopant and the OSC molecules. [52] To enhance charge carrier densities, doping can be carried out by introducing either electron donor or electron acceptor species into the organic semiconductor. Various strategies exist for this purpose, including molecular doping, charge transfer doping, surface doping, electrochemical doping, and thermal doping. [53, 54]

One of the primary doping mechanisms is **charge transfer doping**, in which a dopant molecule either donates or accepts an electron to or from the semiconductor. This process relies on the energetic alignment between the molecular orbitals of the dopant and the host OSC. Specifically, p-type doping occurs when the HOMO of the OSC lies above the LUMO of the dopant, allowing electron transfer from the OSC to the dopant. Conversely, n-type doping takes place when the LUMO of the OSC lies below the HOMO of the dopant, facilitating electron transfer from the dopant to the semiconductor [53, 54]. This technique is used and analyzed for the polymers encompassed in this work.

2.1.2 Charge injection in organic semiconductors

The electronic performance of OSC devices is strongly influenced by both device geometry and contact resistance. These parameters play a crucial role in determining how efficiently charge carriers can be transported and injected within the system. When two materials with different Fermi levels E_F are brought into contact - such as a metal electrode and an organic semiconductor - electrons drift from the material with the higher Fermi level to the one with the lower one. Specifically, the energy levels of the metal contacts and the organic semiconductor must be well-matched to minimize energy barriers and maximize charge carrier

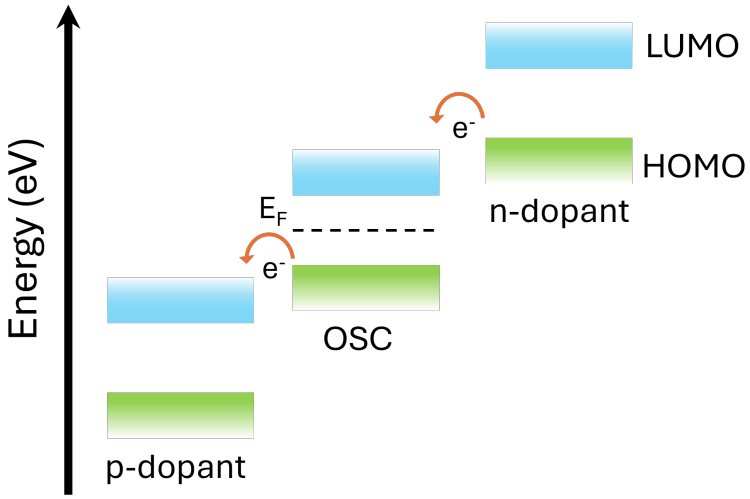

Figure 2.2 Schematic of **charge transfer doping** in OSCs, which is also the technique used in this work. It is based on an energetic difference in the HOMO-LUMO gap of the dopants with respect to the OSC. In case of n-doping, electrons are donated from the dopant to the OSC. For p-doping, the OSC donates electrons to the accepting dopant.

mobility across the interface.

The concept of a Schottky barrier Φ_b is commonly used to model the charge injection process at the metal-organic interface. This barrier arises due to the difference in work functions between the metal and the OSC, leading to a potential barrier that impedes the flow of charge carriers. The width and height of this barrier depend on the charge carrier concentration in the OSC. When the organic semiconductor has a high concentration of charge carriers, the transport mechanism is typically dominated by tunnelling through a narrow depletion region, with depletion width W_d on the order of 2 – 3 nm. In contrast, when the charge carrier concentration is low, the dominant transport mechanism becomes thermionic emission. [17] This mechanism requires charge carriers to overcome the Schottky barrier thermally and is associated with larger depletion widths, in the order of tens of nanometres, making charge injection less efficient. The effective height of the Schottky barrier can be reduced by applying an external voltage across the metal-organic junction. While this technique improves charge injection, it also introduces the need for an external power supply, which reduces the overall efficiency of the device.

2.1.3 Charge carrier characteristics of semiconductor materials in field-effect transistors (FETs)

In order to determine the type of charge carriers that contribute to conduction in a material and measure their mobility, field-effect-transistor (FET) devices can be used. FETs are three-terminal devices that include a source (S), a drain (D) and a gate (G) contact; contrary to

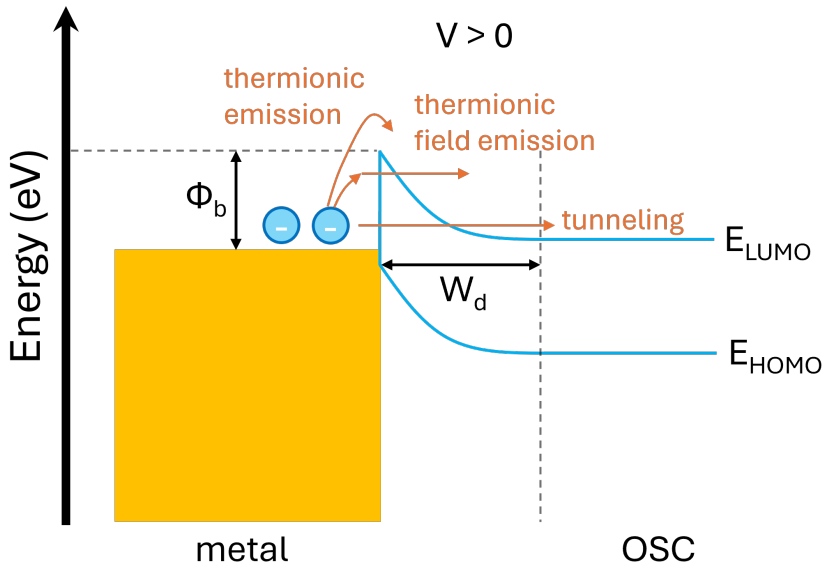

Figure 2.3 Schematic of the interface between a metal contact and an OSC. The Schottky barrier Φ_b arises from the difference in work functions between the metal and OSC. If the OSC has a high concentration of charge carriers, the depletion width W_d becomes small, leading to tunnelling as the dominant transport. In the opposing case, Φ_b needs to be overcome thermally as well for low carrier concentrations. The barrier can be reduced by applying an external voltage $V > 0$, which leads to the curvature representation of the energy levels.

only two types of contacts (drain and source) that are needed for conductivity measurements. The current between D and S, represented as I_{ds}, depends on the voltage V_{ds} between the drain and source contacts, as well as the voltage between gate and source V_{gs}. FETs can generally be divided into four categories, with respect to their channel type (p or n) and if they are normally-on or normally-off. The minimum gate voltage, that is required to enable a conductive channel between drain and source, is called threshold voltage V_{Th}. It can be defined as the voltage at which a significant accumulation of charge carriers occurs at the interface between the organic semiconductor and the gate dielectric, forming a conducting channel. When reaching V_{Th}, I_{ds} starts to flow for any transistor type. For normally-off transistors, the achievable I_{ds} levels increase with increasing steps of V_{gs}, while it works the opposite way for normally-on transistors. In this case, I_{ds} starts at its maximum value and can be decreased by decreasing V_{gs}. Transistors of p- and n-type can be differentiated by the direction of the resulting I_{ds}-V_{ds} or I_{ds}-V_{gs} curve. n-channel FETs open their channel for positive voltages of V_{ds}, showing an increase in I_{ds}, while it is the other way around for p-channel FETs. These show a negative increase of I_{ds} for negative values of V_{ds}. All described cases are shown in Figure 2.5.

FETs can be operated in linear (or ohmic) and depletion mode. The linear region is reached, when $V_{gs} > V_{Th}$ and $V_{ds} << V_{gs} - V_{Th}$. In this region, the FET works like a resistor that is

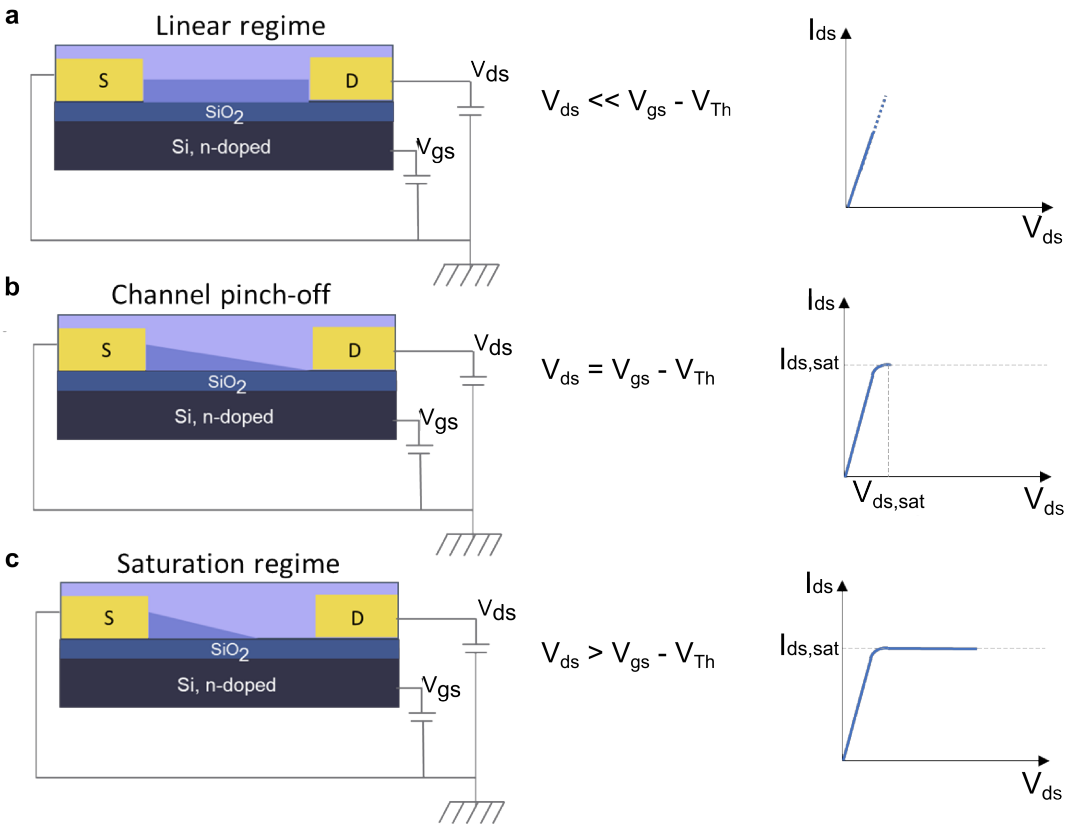

Figure 2.4 Schematic of the two regions of FETs. **a** shows the linear region for drain voltages V_{ds} below the gate voltage V_{gs} minus the threshold voltage V_{Th}. **b** shows the point of channel pinch-off, at which V_{ds} is equal to $V_{gs} - V_{Th}$ where the device begins to saturate, before the saturation regime in **c**. [17]

controlled by the gate voltage relative to the drain voltage. The current I_{ds} can be modelled as: [18, 20]

$$I_{ds} = \mu C_i \frac{W}{L} \left((V_{gs} - V_{Th}) V_{ds} - \frac{V_{ds}^2}{2} \right) \tag{2.1}$$

with the charge mobility μ, the channel length L, channel width W and gate insulator capacitance C_i per unit area. The mobility can graphically be extracted from the linear slope $m_{lin} = \frac{\partial I_{ds}}{\partial V_{gs}}$ in an I_{ds}-V_{gs} graph:

$$\mu = m_{lin} \frac{L}{W} \frac{1}{C_i} = \frac{\partial I_{ds}}{\partial V_{gs}} \frac{L}{W} \frac{1}{C_i} \tag{2.2}$$

The saturation region is reached when $V_{gs} > V_{Th}$ and $V_{ds} \geq (V_{gs} - V_{Th})$, right after the pinch-off region of $V_{ds} = V_{gs} - V_{Th}$. In this region I_{ds} between source and drain does not only flow through a narrow channel, but spreads out across the substrate, as the the drain-source voltage V_{ds} is higher than the gate voltage V_{gs}, which creates the conductive channel in the

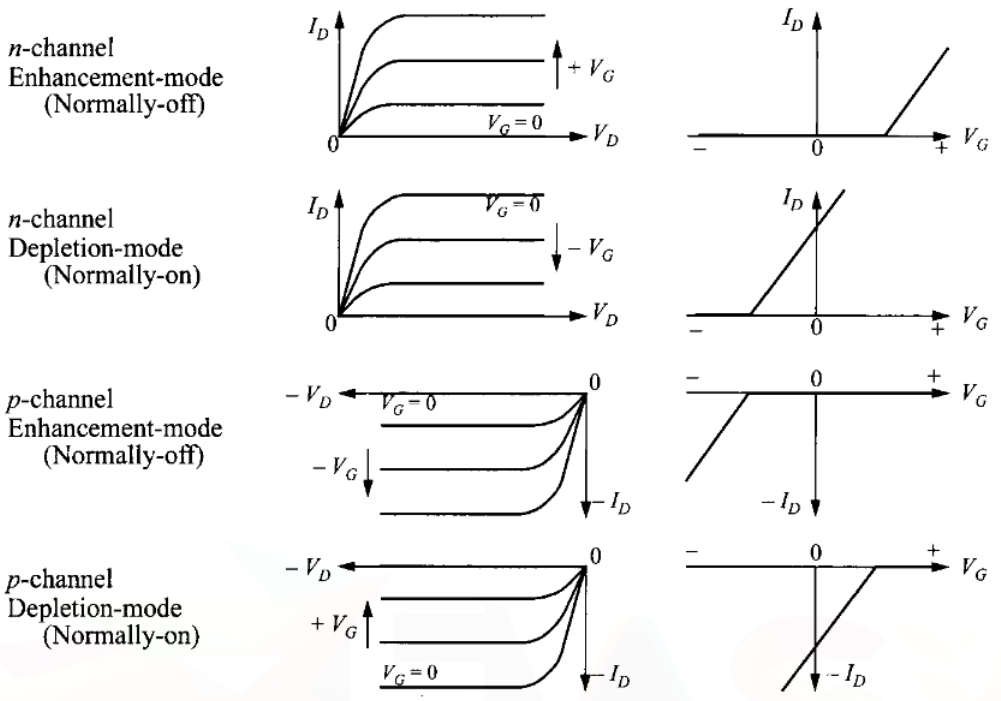

Figure 2.5 Schematic graphs of typical curves for normally-on and normally-off p- and n-type FETs. [55] A key distinction lies in the polarity of the drain current I_D with respect to the drain voltage V_D: n-channel FETs exhibit a positive I_D for positive V_D, whereas p-channel FETs display negative I_D for negative V_D, reflecting the opposite direction of majority carrier transport in the two channel types.

first place. In this region I_{ds} is very weakly dependent on V_{ds} and can be modelled as: [18,20]

$$I_{ds} = \frac{\mu C_i}{2}\frac{W}{L}(V_{gs} - V_{Th})^2(1 + \lambda V_{ds}) \tag{2.3}$$

with the modulation parameter λ, which is used to adjust the dependence of I_{ds} on V_{ds}. For this region, the voltage V_{ds} is increased until the current I_{ds} saturates. The mobility can be extracted in a similar way with a $\sqrt{I_{ds}}$-V_{gs} graph, as it depends quadratically on V_{gs} [20]. Hereby, the slope $m_{sat} = \frac{\partial\sqrt{I_{ds}}}{\partial V_{gs}}$ is used instead of m_{lin}:

$$\mu = m_{sat}^2 \frac{2L}{W}\frac{1}{C_i} = \left(\frac{\partial\sqrt{I_{ds}}}{\partial V_{gs}}\right)^2 \frac{2L}{W}\frac{1}{C_i} \tag{2.4}$$

Figure 2.4 distinguishes the different FET regimes and summarizes the mathematical conditions that apply for each regime.

Characteristics of organic field-effect transistors (OFETs)

A significant difference about the energy levels of organic materials, compared to inorganic ones, is the distribution of their electrons within their molecular orbitals (MOs). Each MO has a certain distribution of electrons within its density of states (DOS), which underlies a small variation from molecule to molecule. Due to a large number of overlapping MOs from all participating molecules in a disordered/amorphous film, this results in a statistical distribution of energy states. In this case, the central limit theory of statistics is applicable, which predicts that the distribution resulting from a random spread of values is a normal Gaussian distribution centred around a mean value, [21]

$$g(\epsilon) = \frac{1}{\sqrt{2\pi}\sigma}\exp\left(-\frac{(\epsilon-\epsilon_0)^2}{2\sigma^2}\right) \tag{2.5}$$

with the mean energy ϵ_0 and the standard deviation (or in this case disorder parameter) σ. Since the filled orbitals end with the HOMO and the sequence of unfilled ones starts with the LUMO, they are also called the frontier orbitals. They take a critical role in the electrical processes of the molecule. For many organic molecules one finds that the first excited state can be well described by a superposition containing a predominant contribution, 80–95%, of the configuration with one electron in the HOMO, one in the LUMO. [21] Figure 2.6 shows the energy diagrams of crystalline semiconductors, metals and organic semiconductors in comparison. Crystalline semiconductors (a) are characterized by a valence and conduction band, with the Fermi level situated in the middle between those. Electrons located in the valence band can overcome the bandgap, usually in the range of a few eV for typical inorganic crystalline semiconductors [56], by doping, thermal excitation, photon absorption or applying an electric field. In metals (b), the Fermi level itself aligns with the conduction band due to the high number of free electron states, which allows for freely moving electrons in the material. The distinction between crystalline and organic semiconductors lies in the difference between conduction/valence band in the former and the MOs in the latter ones. In amorphous, organic materials the distribution of slightly energetically different MOs leads to their separation into distinguished levels.

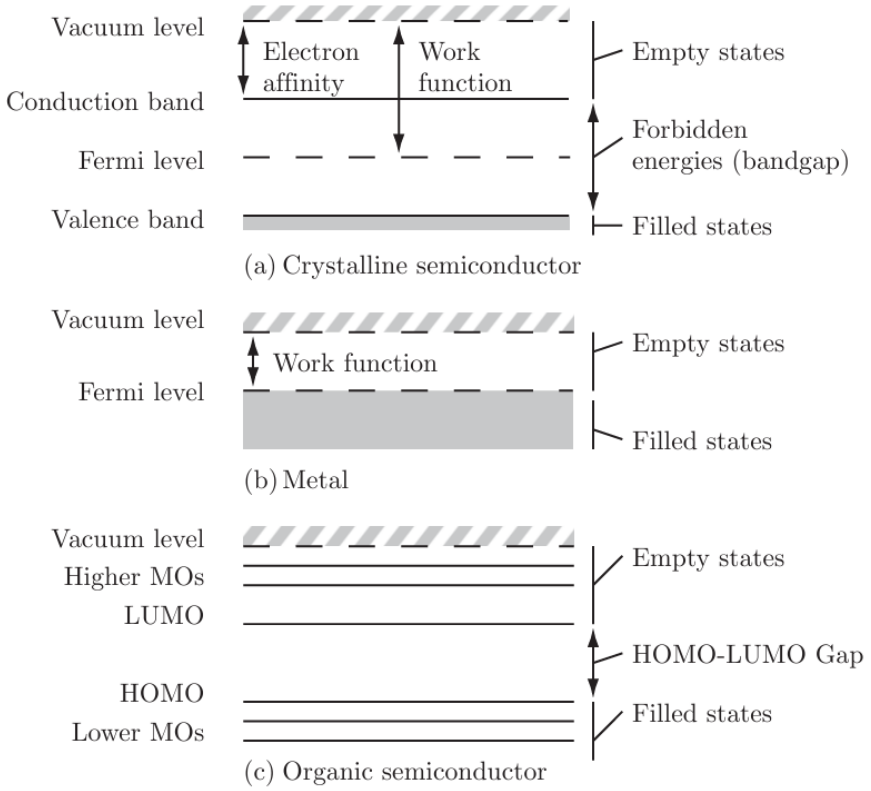

Figure 2.6 A schematic diagram of the energy levels and filled/empty states for (a) a band-transport semiconductor, (b) a metal, and (c) an organic semiconductor in the absence of thermal excitation or doping. In crystalline and organic semiconductors, an energy gap exists, whereas for a metal, energy levels immediately above the filled states are permitted. Carriers ejected beyond the vacuum level can be at any energy. [18]

One of the key operational junctions in OFET devices is the interface between the source and drain contacts and the channel. Any barrier at this interface acts in series, hindering charge transport through the device. Additionally, the formation and structure of the source and drain electrodes can directly influence the properties of the transistor channel. Crystal growth initiated at these electrodes, along with the fabrication processes used to pattern them, can significantly impact overall device performance. As for the electrodes, gold is a popular choice, since its large work function provides reasonable access to the HOMO of many materials [18].

2.2 Thermoelectric properties of organic materials

2.2.1 Seebeck effect

The Seebeck effect can be understood as the electromotive force that develops across two points of an electrically conducting material when there is a temperature difference between them. The Seebeck coefficient S is defined as the magnitude of induced thermoelectric voltage as an effect of a temperature difference across a material. In order to determine the Seebeck coefficient, both the temperature difference along the material ΔT and the induced voltage ΔV must be measured simultaneously. For small values of ΔT, the coefficient is defined as [17, 22]:

$$S = -\frac{\Delta V}{\Delta T} \tag{2.6}$$

The sign convention can be better understood in the representation

$$S = -\frac{V_{left} - V_{right}}{T_{left} - T_{right}} \tag{2.7}$$

as the end with the higher temperature has the lower voltage and vice versa, meaning the voltage gradient within the material points against the temperature gradient. The voltage shift exclusively from the Seebeck effect in the investigated material cannot be measured directly, since the measured value also contains the contribution from the measurement leads. This effect is used in thermocouples to measure temperatures, meaning that for accurate results materials with a stable Seebeck coefficient over time are desirable.
In case of thermoelectric materials, the sign convention leads to a positive slope of S in case of p-type materials, with holes moving from the hotter to the colder side and thus generating a positive voltage difference. The slope turns negative for n-type materials, with electrons moving from the hotter to the colder side and thus generating a negative voltage difference.

More generally, the Seebeck coefficient can be described as the portion of electric current driven by a temperature gradient. Thereby, the current density J can be expressed as the portion caused by an electric field $\mathbf{E}$ and the temperature gradient $\frac{dT}{dx}$, as well as the heat current J_Q, which also depends on the thermal conductivity κ [22]:

$$J = \sigma \mathbf{E} - \sigma S \frac{dT}{dx} \tag{2.8}$$

$$J_Q = (T\sigma S)\mathbf{E} - (\kappa_0 + \kappa_L)\frac{dT}{dx} \tag{2.9}$$

Current is caused to flow due to a difference in temperature T_1 and T_2 between two contacts. Hence, we can describe the difference of the Fermi-Dirac distribution with two different points

of temperature as [23],

$$f_1 - f_2 \approx f_0(E_F, T_1) - f_0(E_F, T_2) \tag{2.10}$$

$$\approx -\frac{\partial f_0}{\partial T}\Delta T \tag{2.11}$$

$$\approx \frac{f_0(T_1) - f_0(T_1 + \Delta T)}{\Delta T}\Delta T \tag{2.12}$$

$$\approx -\frac{E - E_F}{T}\left(-\frac{\partial f_0(E)}{\partial E}\right)\Delta T \tag{2.13}$$

which stems from a finite difference approximation to the derivative of the Fermi function with respect to temperature. The resulting current flow I can be expressed in terms of the Landauer expression [24],

$$I = \frac{2e}{h}\int T(E)M(E)[f_1(E) - f_2(E)]dE \tag{2.14}$$

which integrates over all energy channels of a material (n- or p-type). $T(E)$ is the transmission (between 0 and 1) which is the fraction of passing I, $M(E)$ is the number of available current channels, $f(E)$ is the Fermi-Dirac distribution, the factor $2e$ covers the spin of two electrons with elemental charge e and h is Planck's constant. Together with 2.13, it can be expressed as,

$$I = -\left[\int\left(\frac{E - E_F}{eT}\right)\sigma'(E)dE\right]\Delta T \tag{2.15}$$

with the differential conductivity σ', which describes the energy-dependent conductivity, whereas $\sigma = \int \sigma'(E)dE$ is the overall electric conductivity. Combining these statements, the Seebeck coefficient can now be expressed as an equation that is averaging the energy, weighting the energy by the amount of current that flows at a certain energy [23, 25],

$$S = -\frac{\int\left(\frac{E-E_F}{eT}\right)\sigma'(E)dE}{\int\sigma'(E)dE} = -\int\frac{E - E_F}{eT}\frac{\sigma'(E)dE}{\sigma} \tag{2.16}$$

which can also be expressed in terms of the average energy E_J at which electrons flow:

$$S = -\frac{E_J - E_F}{eT} \tag{2.17}$$

In semiconductors, the Fermi energy lies below the conduction band, meaning that the average energies of conduction-participating electrons are much higher than the Fermi energy ($E_J >> E_F$), resulting in a very large absolute Seebeck coefficient, according to 2.17. In conductors (or heavily doped semiconductors), the Fermi energy lies within the conduction band, meaning that the difference between the average energy and Fermi level becomes negligible ($E_J \approx E_F$), which leads to a very small Seebeck coefficient. These trends are depicted in Figure 2.7.

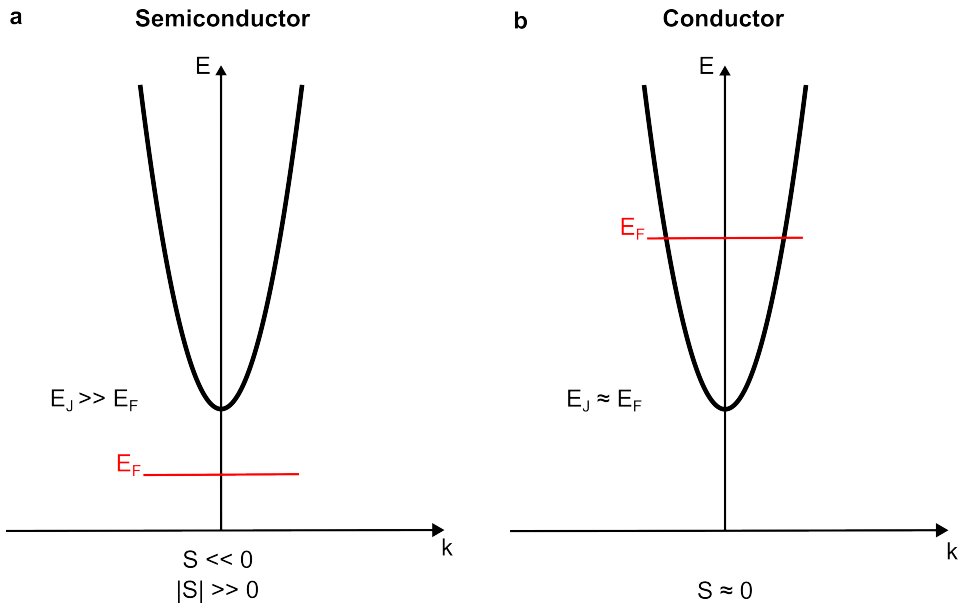

Figure 2.7 Visualization of the relation between the Seebeck coefficient S and the average electron energy E_J with respect to the Fermi level E_F. **a** shows the case for a regular semiconductor, with E_F being located below the conduction band and **b** the case of a conductor or heavily doped (n-type) semiconductor, with E_F being situated within the band and hence, reducing the energy difference $E_J - E_F$.

2.2.2 Thermoelectric generators

Thermoelectric generators (TEG) are structures that convert heat into electrical energy, which are therefore used to recycle waste heat through partial conversion into electrical power. The physical principle of action is based on the Seebeck effect. Due to the higher thermal movement of the charge carriers on the warm side of a material, compared to the cold side, a gradient in the charge carrier density is formed, which leads to a voltage difference. A thermoelectric material is typically sandwiched between a hot ($T = T_h$) and a cold ($T = T_c$) electrode. [17] The maximum efficiency of any thermoelectric device η_{TE} can be expressed as a function of the Carnot efficiency $\eta_c = (T_h - T_c)/T_h$,

$$\eta_{TE} = \eta_c \frac{\sqrt{1+zT} - 1}{\sqrt{1+zT} + 1 - \eta_c} \tag{2.18}$$

The dimensionless factor zT is called figure of merit, which is a measure of performance of a material depending on the Seebeck coefficient S, its electrical conductivity σ, the temperature T and the thermal conductivity κ: [3, 26]

$$zT = \frac{S^2 \sigma T}{\kappa} \tag{2.19}$$

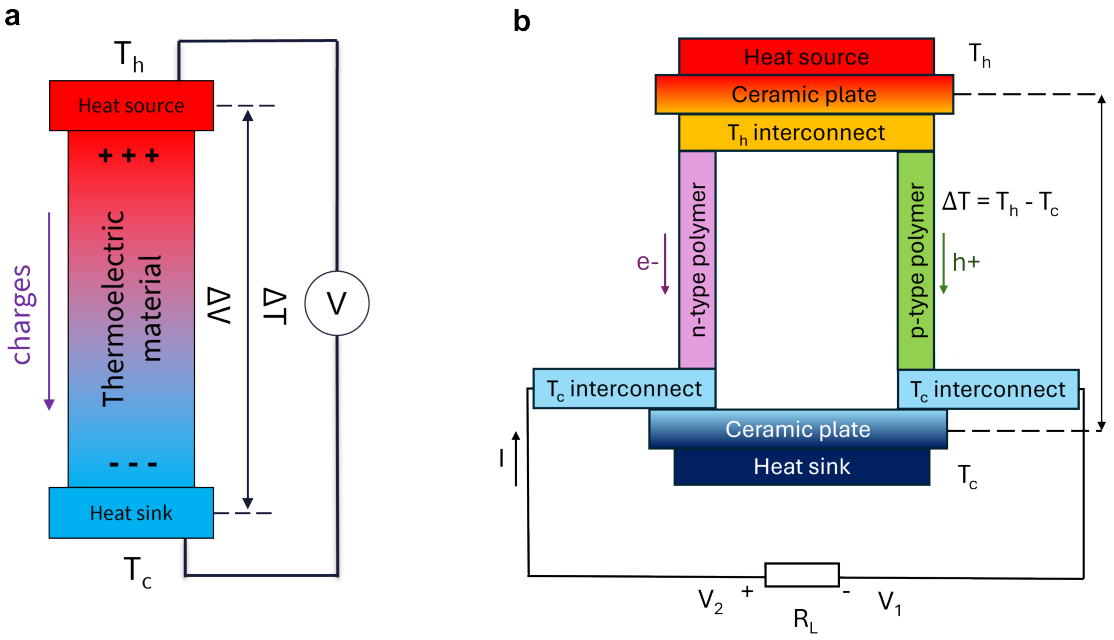

Figure 2.8 Schematic of the functional principle of a thermoelectric generator (TEG). **a** shows a basic example for a one-leg TEG. It functions based on the Seebeck effect, according to which a voltage difference ΔV is induced by an external temperature gradient ΔT. Two-leg structures, as in **b**, are commonly used in repetition of hundreds or thousands of elements to accumulate the generated output power.

Accordingly, the efficiency of a TEG increases with high electrical conductivity σ and high Seebeck coefficient S and low thermal conductivity κ. However, a precise determination of thermal conductivity is often difficult, which is why the power factor PF

$$PF = S^2\sigma \tag{2.20}$$

is often used, due to its independence of κ. [17]

Figure 2.8 shows the functional principle of a TEG element. Due to the heat flux of the heat source to the heat sink, a drift of the electrons in the n-type leg and holes in the p-type leg is formed from the warm to the cold side. This creates an electrical current I, triggered by the opposing charge carriers that collect on the cold end. An external load R_L is driven in a closed circuit between n- and p-side, which can be used to power electrical applications. [3,14]

2.2.3 Principles of heat transport in organic semiconductors

Heat carriers in organic semiconductors are mainly phonons and electrons, which collide with one another and thereby produce a heat transfer phenomenon. The total thermal conductivity κ in a material is the sum of the contributions by phonons κ_{ph} and electrons κ_e:

$$\kappa = \kappa_{ph} + \kappa_e \tag{2.21}$$

In undoped or lightly doped OSCs, electrons only have little contribution to the total thermal conductivity. [27] In crystalline materials, such as many inorganic or organic single-crystal ones, κ_{ph} can be predicted by the phonon gas model, [28]

$$\kappa_{ph} = \frac{1}{3} C v_g l = \frac{1}{3} C v_g^2 \tau \tag{2.22}$$

which includes the specific heat capacity per unit volume C_g, the phonon group velocity v_g, the phonon mean free path l in the first form, and the phonon relaxation time τ in the second one. However, phonon-related characteristics are difficult to describe in amorphous materials due to their lack of long-range ordered periodicity. Compared with inorganic semiconductors composed of covalent bonds, the interaction between OSCs stems from noncovalent ones, such as π-π interactions, hydrogen bonds and van-der-Waal interactions, which are altogether weaker than covalent bonds. Moreover, OSCs are in single crystal, polycrystalline, and amorphous structures. Therefore, current theoretical models are difficult to describe heat transport characteristics of organic semiconductors accurately. [27]
κ behaves differently for amorphous and more ordered, semi-crystalline polymers. As Figure 2.9 shows, κ rises steeply for semi-crystalline polymers compared to a moderate decrease in the amorphous ones. A possible explanation is better phonon wave propagation, and therefore heat transport, in materials with higher crystalline-like order. Overall, the heat conductivity changes only by a small amount within the order of one magnitude, compared to eight magnitudes for the mobility μ_{FET}. Considering that μ and σ are related by the product of charge carrier density n, elemental charge e and μ: $\sigma = ne\mu$, it shows that the thermal conductivity only changes by a small value, compared to the electrical one. [8]

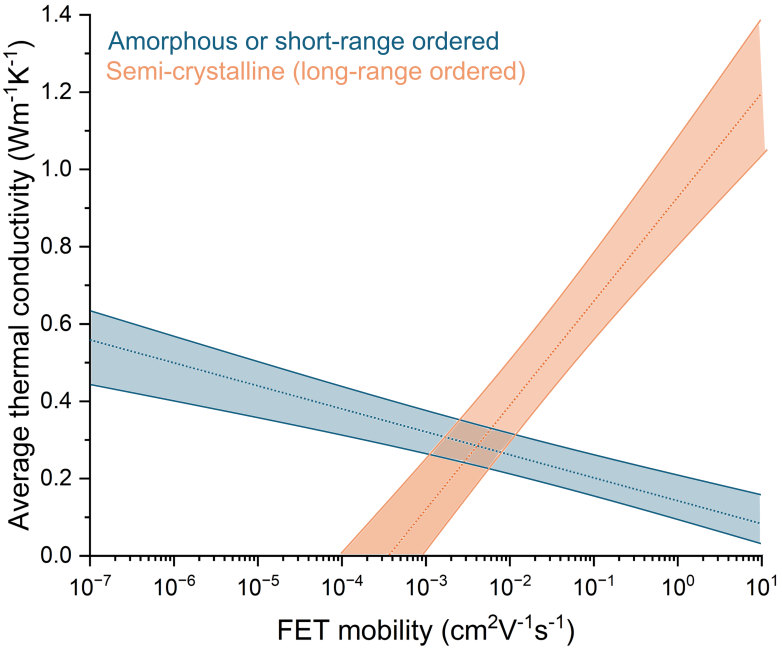

Figure 2.9 Relation of the average thermal conductivity κ and the charge carrier mobility μ_{FET} for multiple, here not further specified, π-conjugated polymers and small molecules. [8] κ shows a slowly falling slope within the same order of magnitude for amorphous materials with increasing μ_{FET}, contrary to semi-crystalline ones with a higher and rising slope.

3 Methods

Building upon the theoretical principles outlined in the previous chapter, this section details the experimental procedures and materials used throughout the study. The focus lies on the organic polymers selected for investigation, the fabrication techniques and layouts used for conductivity, Seebeck coefficient and field-effect-transistor samples and the specific measurement techniques employed to characterize their properties.

3.1 Organic polymers encompassed in this study

3.1.1 Poly-3,4-ethylenedioxythiophene polystyrene sulfonate (PEDOT:PSS, p-type conductor)

Poly-3,4-ethylenedioxythiophene (PEDOT) is a widely studied conducting polymer. It has high stability, moderate band gap and low redox potential. Its major disadvantage is low solubility. Therefore, it can be combined with polystyrene sulfonate (PSS) to create the composite p-type conductor PEDOT:PSS. Both molecules are shown in Figure 3.1**a**, with PEDOT on the left and PSS on the right. PSS acts as a counter-ion to balance the charge in the molecule and improve water solubility. For this work, 2.8 wt% dispersion in H_2O from Sigma Aldrich is used. PEDOT:PSS has the highest reported efficiency among conductive organic thermoelectric materials with a zT of 0.42. [5] In combination with further organic compounds it is suitable for touchscreens, organic light-emitting diodes (OLEDs) or organic solar cells for example, to replace traditionally used inorganic materials. PEDOT:PSS is used in this work to verify the functionality of the two setups for the electrical characterization and determination of Seebeck coefficients of polymers, as the parameters of this polymer are well studied.

3.1.2 Poly-3-hexylthiophene (P3HT, p-type semiconductor)

Poly 3-hexylthiophene (P3HT) is a polymer with known high hole-mobility. It possesses both amorphous, and ordered crystalline regions. [29] It is well-soluble in chloroform up to a concentration of 38 mg/mL. [30] The molecular structure is shown in Figure 3.1**b**. In this work it is used at 5 mg/mL.

Its HOMO has been determined to lie at -5.08 eV, measured with cyclic voltammetry [10], or at -4.9 eV measured with ultraviolet photoelectron spectroscopy (UPS) and Angle-resolved X-ray photoelectron spectroscopy (AR-XPS) [11]. The conductivity of pure P3HT between 20 - 30°C is in the range of 6.7 - 9.4 nS/cm. [31] In this work the product LT-S909 from the

Luminescence Technology Corp. is used. The molecular weight of P3HT is calculated from the weights of its respective atoms to 165.28 g/mol.

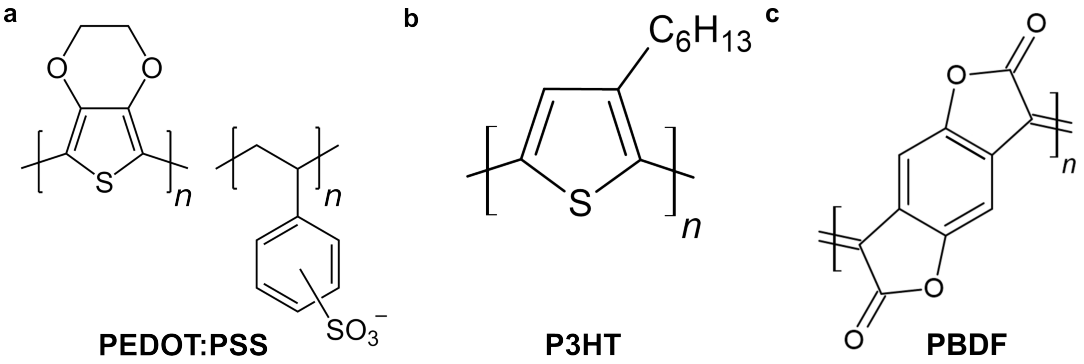

Figure 3.1 Sketches of the encompassed polymers in this study.

3.1.3 Poly-3,7-dihydrobenzo[1,2-b:4,5-b´]difuran-2,6-dione (PBDF, n-type conductor)

PBDF is a solution-processable n-type organic conductor from copper-catalyzed cascade reactions. It is a shelf-stable polymer under storage temperatures of -20 to 65°C. PBDF exhibits low sheet resistance down to 45 Ω/sq and a high transmittance in visible range of T_{550} >80%, which rivals the parameters of indium tin oxide. [12] It is to-date the organic n-type conductor with the lowest LUMO level, which makes it the only known n-polymer to be thermodynamically stable. Its molecular structure is shown in Figure 3.1**c**.

A polymer is considered kinetically stable when its LUMO is below -4.0 eV to avoid water and oxygen reduction reactions and be prone to degrade upon exposure to heat. It is theoretically postulated that the level must be below -4.9 eV to achieve thermodynamically stable n-type charge transport. [12] Another source mentions a required electron affinity of more than 4 eV, to avoid reaction with water and oxygen and associated trap states. [25] The conductivity of PBDF depends on the copper acetate loading and therewith lies between 12-2100 S/cm [12, 42], which renders it much more conductive compared to P3HT by a factor of more than 10^9. Together with a Seebeck coefficient of -21 µV/K, it can reach power factors of 90 $\mu Wm^{-1}K^{-2}$. [42] In this work it is applied in a solution with dimethyl sulfoxide (DMSO) in a concentration of 7 mg/mL. One PBDF molecule has a molecular weight of 186.12 g/mol.

Doping mechanism through the energy scheme of P3HT and PBDF

The close proximity of the HOMO of P3HT and the LUMO of PBDF, within the statistical distribution of the orbital's energy values, can enable charge transport between the polymers. Figure 3.2 visualizes the charge transfer mechanism in a simplified schematic.

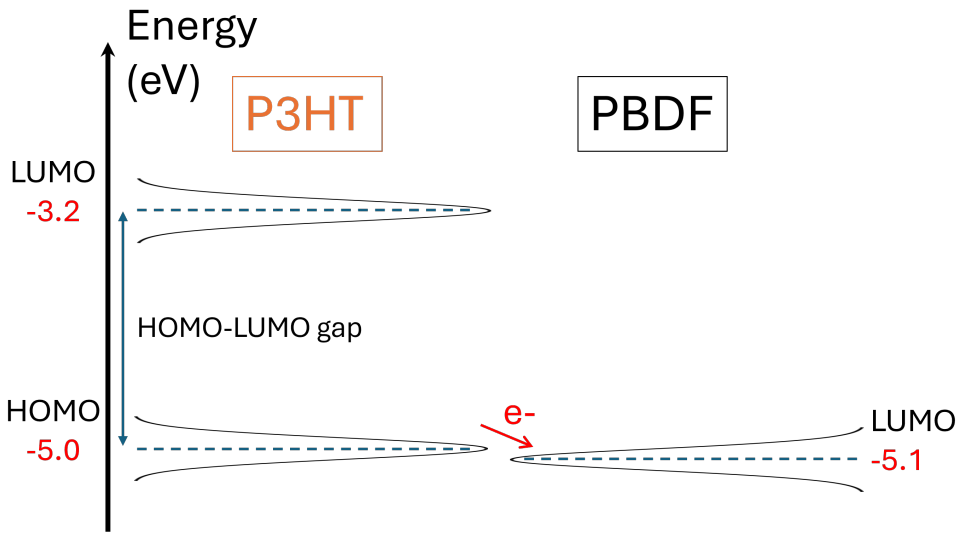

Figure 3.2 Representation of the HOMO and LUMO energy orbitals of P3HT and PBDF with respect to one another. If both polymers are brought together close enough, the potential barrier between them becomes vanishingly small which makes electron tunnelling between the HOMO of P3HT an LUMO of PBDF theoretically possible.

3.2 Glovebox

The glovebox is an isolated environment from the normal outside atmosphere. For this work, the model 'Universal' from Vacuum Technology Inc. (VTI) was used. It has lower pressure (about 1/1000 of atmospheric pressure), a nearly homogeneous nitrogen-filled environment and negligible contents of water and oxygen (< 0.01 ppm H_2O and O_2 under regular conditions). These parameters are used to enable equally clean conditions for all samples. It also achieves an anhydrous and anaerobic environment to prevent any interactions with oxygen and prevent samples from being moistened with water.

The system uses a copper catalyst to remove oxygen out of the internal atmosphere by the reaction: $O_2 + 2\,Cu \longrightarrow 2\,CuO$. Over time, the catalyst gets saturated with CuO, as it does not react back into Cu itself. It therefore needs to be regenerated twice a year under regular use. The regeneration process requires hydrogen, which reacts with CuO to copper and water: $CuO + H_2 \longrightarrow Cu + H_2O$.

3.3 Polymer blending and drop-casting

P3HT is doped by PBDF through blending in this work. The entire preparation and blending process is carried out in a glovebox. Therefore, solid P3HT fibres are first dissolved in chloroform in a vial in a 5 mg/mL concentration. The solution is stirred for at least 30 min to become homogeneous. After, a desired volume of it is added into a second vial for the blending process. PBDF, which is used in an already prepared DMSO solution, is then added according to the desired amount. The blended solution is finally stirred for at least another

30 min. Both of the used solvents are miscible according to miscibility tables [57]. Depending on the desired mass concentration in mg/mL, the weight percentage (wt%) of the doping polymer (PBDF) to the base polymer (P3HT) is calculated. Considering a base polymer A and a doping polymer B, the weight percentage is

$$\text{wt\%} = \frac{m_B}{m_A + m_B} \cdot 100 = \frac{V_B \cdot c_B}{V_A \cdot c_A + V_B \cdot c_B} \cdot 100 \tag{3.1}$$

Therefrom, the required volume of doping polymer solution B for a given volume of base polymer solution is

$$V_B = \frac{0.01\text{wt\%} \cdot V_A \cdot c_A}{c_B(1 - 0.01\text{wt\%})} \tag{3.2}$$

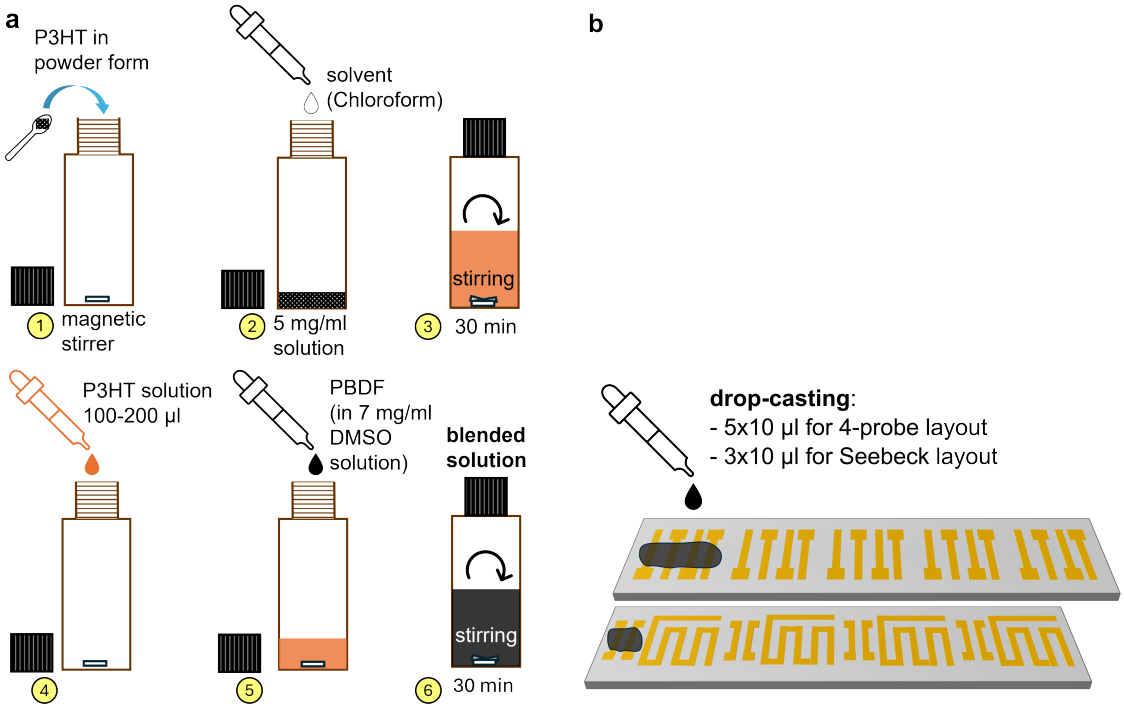

Figure 3.3 **a** Depiction of the polymer blending process for P3HT with PBDF inside the glovebox. **b** Drop-casting process of polymer solutions onto gold contacts for electric and thermoelectric characterization. Each of the samples (meaning five on the upper, and four on the lower glass substrate) is coated and used separately.

Figure 3.3**a** represents the polymer preparation and blending process. **b** shows the following drop-casting step onto gold contacts for (thermo-)electric characterization. The solution is applied in multiple stacked layers, meaning 3x10 µL in case of the Seebeck measurement samples and 5x10 µL for the conductivity samples, as the polymer-covered region is about half the size for the former ones. Applying more solution results in partial coverage of the heating coil, which bridges it with the measurement contacts, enhances the thermal conductivity between both sets of contacts and thereby falsifies the measurement.

3.4 Electron-beam metal deposition

The contacts for all electrical measurements were deposited by electron-beam (e-beam) deposition with the 'AXXIS' evaporator from Kurt J. Lesker. It includes a 6" sample holder, which is fully covered with six glass slides for each deposition run. Before each deposition, a magnetic metal plate is used as a holder for the slides and shadow masks on top of them. The shadow masks are then fixed on the glass slides with small magnets. The slides themselves need to be fixed to the metal plate with vacuum tape, as well as the plate to the e-beam device's sample holder with another set of tape. Figure 3.4 illustrates the composition of the described layout for an e-beam run.

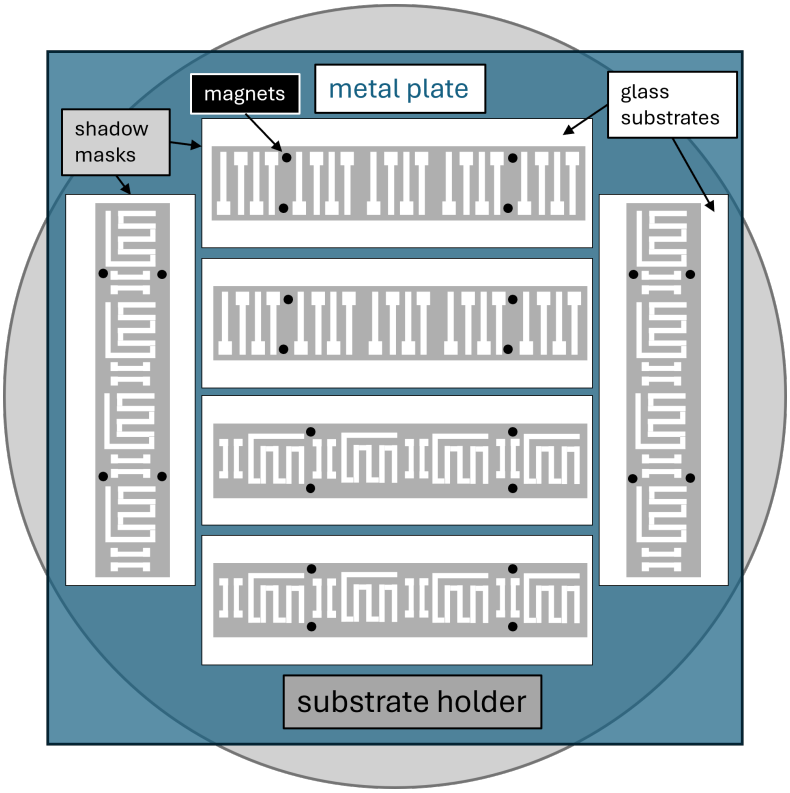

Figure 3.4 Schematic of the shadow masks, glass slides and metal plate assembly for an e-beam deposition run.

The e-beam process itself uses a heated filament to generate an electron beam, which is directed onto a target to be evaporated. The electrons coming from the filament are attracted by a strong electric field into the effective range of a magnetic field, to make use of Lorentz force. Said force guides the electrons in a circular motion onto the ingot material (in this case chromium (Cr) or gold (Au)) to heat it, until it starts to evaporate. The evaporated material rises, as illustrated in Figure 3.5, until it reaches the target substrate surface. In contact with the cold surface, it condensates and deposits there.

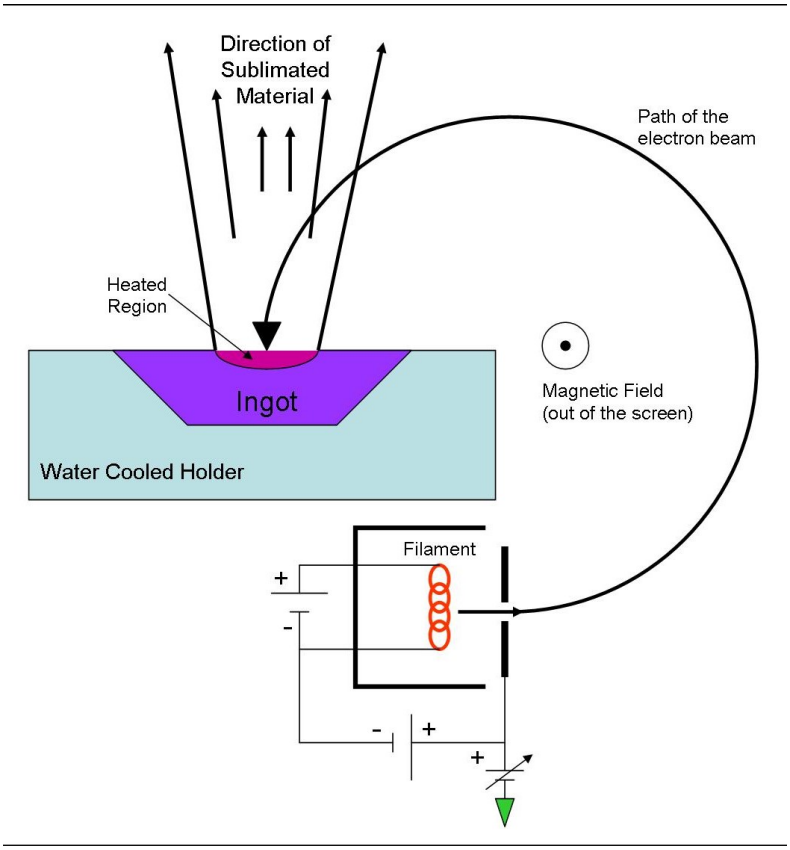

Figure 3.5 Schematic of the e-beam deposition process. The ingot is held in position by a positive potential relative to the filament. A magnetic field is applied to move the electrons into a circular path by means of the Lorentz force onto the ingot material. It thereby heats up until it evaporates in direction of the substrate. [32]

For the deposition, Cr and Au are used as contact materials. First, a 5 nm thick layer of Cr is deposited, followed by a 50 or 100 nm thick layer of Au. Cr is thereby used to enhance the adhesion between Au and the glass surface. It has a high oxygen affinity and therefore bonds well with the SiO_2 glass [33, 34], compared to the noble metal Au.

3.5 Electrical conductivity measurements

Electrical conductivity σ is the fundamental property of a material to conduct electricity. It is the inverse of the specific resistivity ρ of a material. The resistivity is defined as the product of the absolute resistance R and the product of the cross-sectional area A and the length l of a material. [35]

$$\rho = R\frac{A}{l} \tag{3.3}$$

Accordingly, the conductivity is defined as the inverse:

$$\sigma = \frac{1}{R}\frac{l}{A} \tag{3.4}$$

In the ideal case, the cross-section and physical composition of the investigated sample are uniform, leading to both parallel and constant electric field and current density across the entire shape. This does not apply in reality, especially in case of drop-casted polymer solutions. Therefore, the cross-sectional area has to be averaged within the effective measurement range. Considering the general formula for Ohmic resistance $R = \frac{V}{I}$, the resistivity of a material with respect to four-probe sensing is defined as:

$$\rho = \frac{V}{I}\frac{W \cdot t}{L} \tag{3.5}$$

and the conductivity as:

$$\sigma = \frac{I}{V}\frac{L}{W \cdot t} \tag{3.6}$$

whereas W and L represent the width and length of the measured channel, and t the thickness of the film. For this work, the four-probe sensing technique is used to determine a sample's conductivity. It requires four contacts that are linearly placed along the sample. Here, gold is used as contact material, which is evaporated by e-beam deposition through a shadow mask onto glass and Si substrates. The current flows through two outer contacts near the sample edges and the potential difference is gauged across the remaining two inner contacts, hence the lead and contact resistance get eliminated as both circuits are separated [36]. Figure 3.6**a** represents the wiring for the setup to measure current flow and voltage gradient across a sample. The conductivity is then calculated according to Equation 3.6. Figure 3.6**b** shows the placement of five sets of four-probe gold contacts on a glass slide.

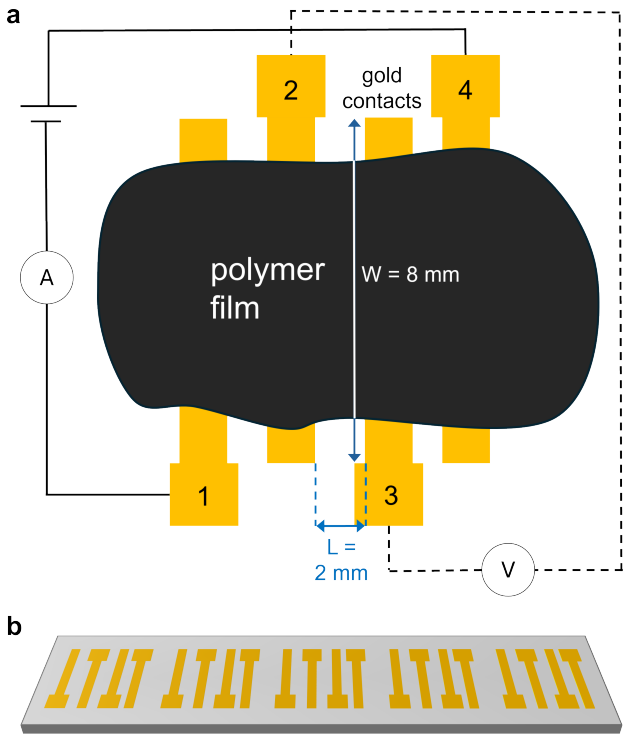

Figure 3.6 **a** Schematic for the four-probe measurement setup on glass. Between contacts 1 and 4, a sensing current is applied, while the voltage gradient is measured between contacts 2 and 3. L represents the channel length and W the channel width. **b** shows five deposited sets of gold contacts for the setup on a glass slide.

3.6 Seebeck coefficient measurement method

For the measurements a design with gold contacts for the voltage and temperature measurements, as well as a heating coil is used. A voltage source connected to both ends of the coil passes a defined current of up to 300 mA through the gold to generate Joule heating. As glass has a low thermal conductivity (κ_{glass}=0.8 Wm^{-1}K^{-1}, compared to κ_{gold}=314 Wm^{-1}K^{-1}), the temperature on the polymer side close to the heating coil slowly increases over time, but faster than on the opposite end. This creates a temperature gradient across the polymer film which induces a corresponding voltage. Two probes are connected to either side of the polymer to measure the induced voltage across the film with a Keithley 2636B SMU (the identical instrument used for conductivity measurements). Simultaneously, two thermocouples on the opposite set of contacts measure the temperature gradient. The voltage source is set to multiple levels of heating power, with a one to three minutes waiting interval after each level, so that a constant temperature gradient between both contacted sides of the polymer sample is temporarily established. That gradient can reach values of more than 10 K for the maximum used heating power. The measured voltage is averaged over each of those intervals. Figure 3.7**a** represents the wiring for the setup, whereas 3.7**b** shows four sets of Seebeck measurement layouts on a glass slide.

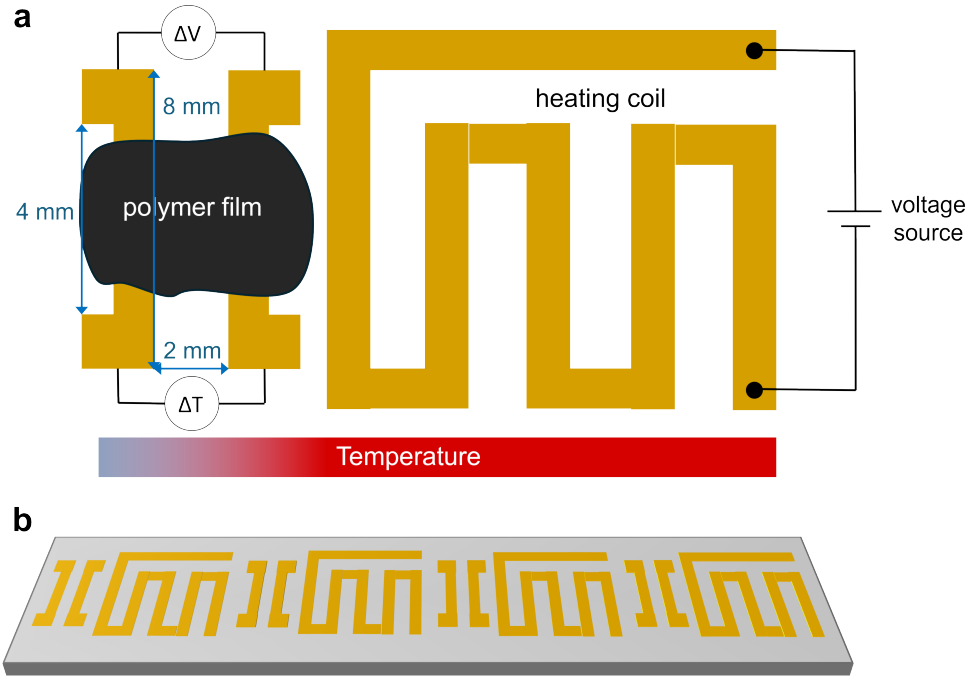

Figure 3.7 Schematic for the Seebeck coefficient measurement setup on glass. **a** A voltage source is attached to the two ends of the heating coil to heat the right side of the polymer film. The generated voltage gradient is measured by a Keithley SMU, simultaneously to the temperature gradient measured by a thermometer with K-type thermocouples. **b** shows four deposited sets of gold contacts for the setup on a glass slide.

3.7 Field-effect transistor (FET) measurements for charge carrier type and mobility

Two types of layouts are used to characterize the mobility and charge carrier type of the polymers encompassed in this work. Both layouts are used on highly n-doped (n^{++}) Si substrates with a SiO_2 insulation layer. The first layout is based on the same shadow masks that are also used for the conductivity measurements to ensure the same channel geometry and therefore comparability of the resulting I-V curves for voltage sweeps. It is represented in Figure 3.8**a**. As FETs are 3-terminal devices, compared to 2-terminal ones used for the conductivity measurements, a pair of gold contacts each is used as source and drain, while Si at the bottom acts as gate contact. The shadow mask parameters result in a channel length L of 2 mm and width W of 8 mm.

Figure 3.8**b** shows the second layout. It is not fabricated locally, but provided by the Fraunhofer Institute for Photonic Microsystems IPMS. The layout consists of 16 independent FETs which are structured on a Si chip, again with the bottom as gate contact. A pair of four FETs each has the same length L, with values of 2.5, 5, 10 and 20 µm. The contacts build up an interdigitated structure between the source and drain pads, which sum up to a width of $W = 10$ mm for each FET. These samples from Fraunhofer are used in comparison to the self-fabricated samples with shadow masks.

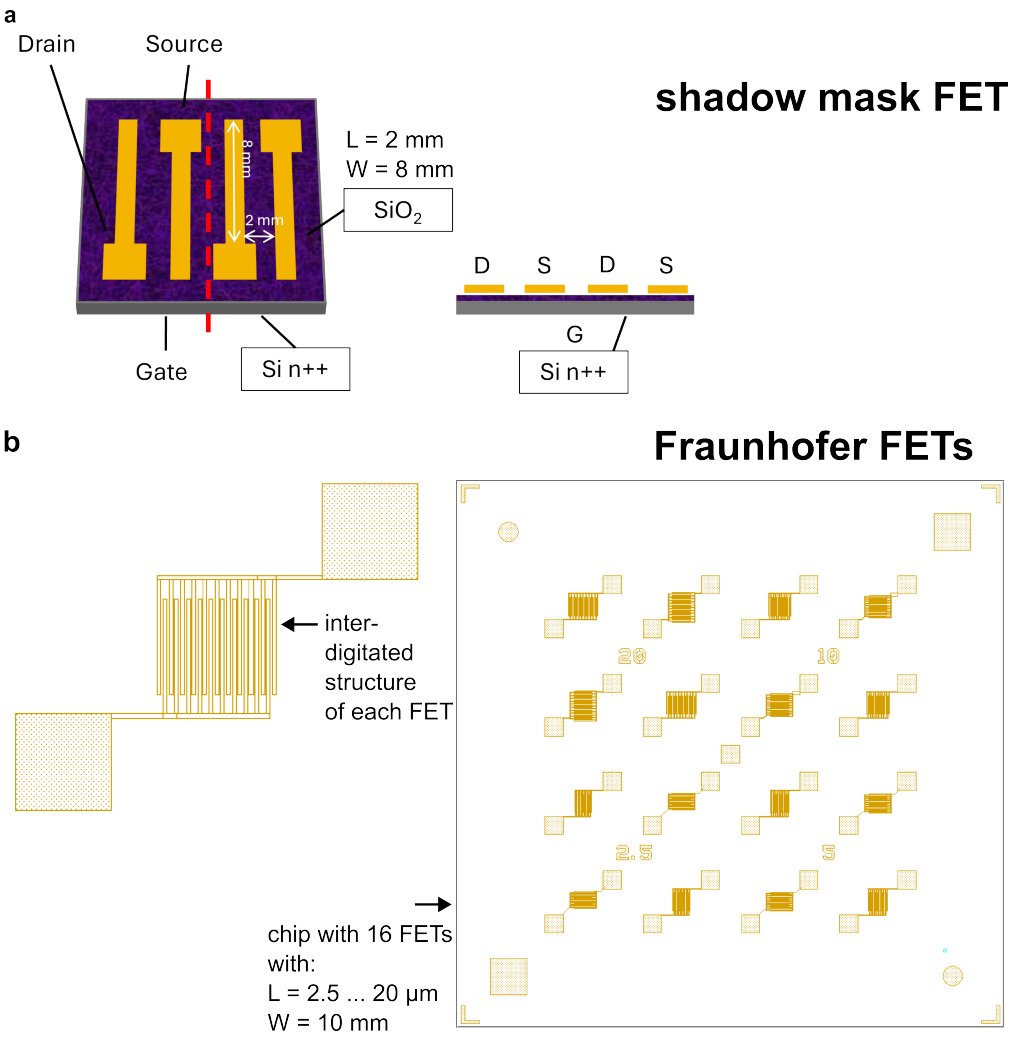

Figure 3.8 **a** shows field-effect transistors (FETs) assembled with the same shadow mask design that is used for the conductivity measurement samples. Gold contacts, for source S and drain D, with a thickness of 50 nm are evaporated by e-beam onto highly n-doped (n^{++}) Si (grey), with a 285 nm insulating layer of SiO_2 (violet) on top. **b** shows a ready-made substrate from Fraunhofer. A 1.5x1.5 cm^2 substrate includes 16 FETs with varying channel lengths of 2.5, 5, 10 and 20 µm for a set of four FETs each. Each FET has an accumulated channel width of 10 mm, due to the interdigitated structure of the electrodes. The insulating SiO_2 layer is thinner compared to **a** with 230 nm.

3.7.1 Octadecyltrichlorosilane (OTS) treatment

Octadecyltrichlorosilane (OTS) is an organosilicon compound with the formula $CH_3(CH_2)_{17}SiCl_3$. It is applied on SiO_2 to enhance the electronic properties of the polymer films, meaning the field-effect mobility μ_{FET} and drain-source current. It has been observed to improve these properties for pentacene layers by a factor of up to 8, due to an increase of the number of π-bonding states in the active layer [37, 38]. In case of perylene an increase of 100 times could be observed [39]. The OTS procedure used for this work is adapted from Wang and Lieberman 2003 [40], who reported good results in terms of surface smoothness, contact angle and surface coverage on SiO_2 after soaking substrates in 5 mmol OTS solution for 48h. Before the OTS solution is applied on silicon substrates, these are cleaned with acetone and isopropanol for 10 min each in a sonicator, followed by a 5 min clean with DI-water and a heating process at 140°C for another 5 min to evaporate excess water. The substrates then undergo a 10 min ozone treatment to make the SiO_2 surface more reactive to chemical bonding. The whole process up to this point is done in-air. After ozone treatment, the substrates are immediately transferred into the glovebox to begin the OTS treatment. In this work, OTS is used in a concentration of 9.7 µL of OTS dissolved in 5 mL of toluene, which corresponds to about 5 mmol. Up to six substrates can be treated simultaneously in the solution. They are inserted in a jar with it, sealed and then heated at 60°C for 1 h. After, the solution is left to rest for 48 h in the glovebox. Each substrate is then transferred into a second, clean jar filled with 10 mL of toluene to be stirred and cleaned. The substrates are then together heated again at 60°C for 1h to remove the solvent and keep just the OTS coated substrates.

4 Results and Discussion

After establishing the theoretical and methodological framework, this chapter turns to the core findings of the study. It presents all relevant obtained results throughout optical and mechanical surface topography, conductivity and Seebeck coefficient measurements and field-effect transistor analysis. The findings are discussed and evaluated with respect to corresponding and current literature.

4.1 Polymer film topography analysis

Surface analysis is conducted via optical microscopy, profilometry and atomic force microscopy (AFM). The first method is used to achieve a top view of pure P3HT and PBDF, as well as blended solutions on a micrometer scale. This is important to spot any mesoscopic evidence of poor solubility or phase segregation of both polymers. Profilometry allows scans across polymer films in one dimension, making it possible to measure the film thickness up to a few nanometres. The last method, AFM, is used to get a more accurate understanding of the polymer topography in the nanometre range. Especially phase segregation and the general morphology and roughness can be resolved at a much smaller scale than optical microscopy .

4.1.1 Optical microscope images

The microscope images in Figure 4.1 show three separate drop-casted films on a glass substrate in comparison. All solutions are prepared and drop-casted in the glovebox. The images are then taken outside the glovebox, under ambient conditions.

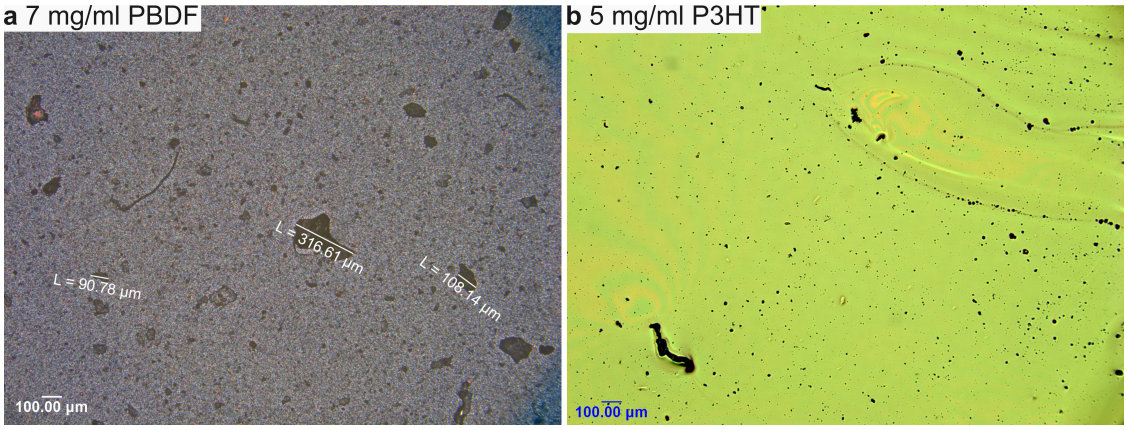

Figure 4.1 Microscope images of separates of 7 mg/mL PBDF in **a** and 5 mg/mL P3HT in **b** on glass in comparison. PBDF solution contains significant undissolved particles in size of more than 300 µm.

Figure 4.1 shows films of PBDF in 7 mg/mL and P3HT in 5 mg/mL concentration in comparison. Both films were applied in five times 10 µL drops, up to a total of 50 µL, which is the same procedure as for the regular drop-casted samples. PBDF includes a number of solid aggregates with sizes from 90 to >300 µm. In contrast, the P3HT film does not include particles of the same yellowish color contrast than the film itself. Visible small black spots of a few micrometres in size are attributed to contaminants, that were introduced onto the dried film post-preparation.

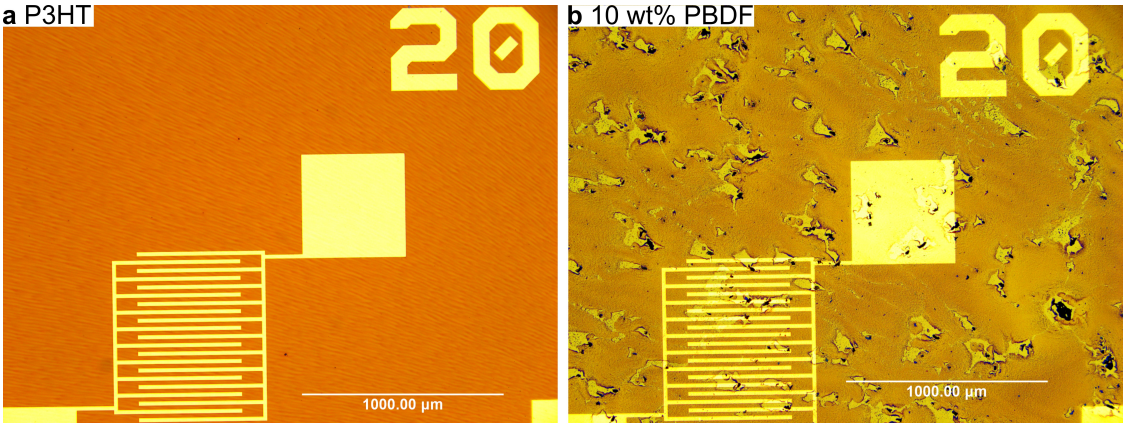

Figure 4.2 Comparison between spin-coated FET samples at 3000 rpm for 60 s. Sample **a** has a pure P3HT coating, sample **b** is a 10 wt% PBDF-doped solution. The black particles are aggregates of PBDF.

Figure 4.2 shows two spin-coated samples on Fraunhofer substrates with a one minute spin at 3000 rpm. 4.2**a** shows a purely P3HT-coated sample, while 4.2**b** is a blended sample with 10 wt% PBDF. The blended sample in **b** includes similar PBDF particles as the drop-casted films of pure PBDF in solution in Figure 4.1.
Polyvinylidene difluoride (PVDF) filters with pore sizes of 0.2 and 0.45 µm were tested on pure PBDF in DMSO solution. It was not possible to squeeze the solution through a syringe through the filters, which suggests common particle sizes $>$0.45 µm, as it is also expected from the microscope images. Hence, filtration did not prove possible within this thesis.

4.1.2 Profilometry

To determine the film thickness t, which is a necessary parameter to calculate the conductivity σ, an Ambios XP2 profilometer is used. It has a lateral resolution of 100 nm and is used at a force of 10 mg. Figure 4.3 shows two examples of a thickness profile of a drop-casted 1 wt% and 5 wt% PBDF-doped P3HT solution, in 4.3**a** and 4.3**b** respectively. The drops show a curvature from the center outwards to their edges, which is typical for drop-casting [41], contrary to e.g. spin-coating. The profiles show multiple inhomogeneities, most of which differ up to a micrometer. Those correspond to normal irregularities on the polymer surface, due to the drop-casting method itself.

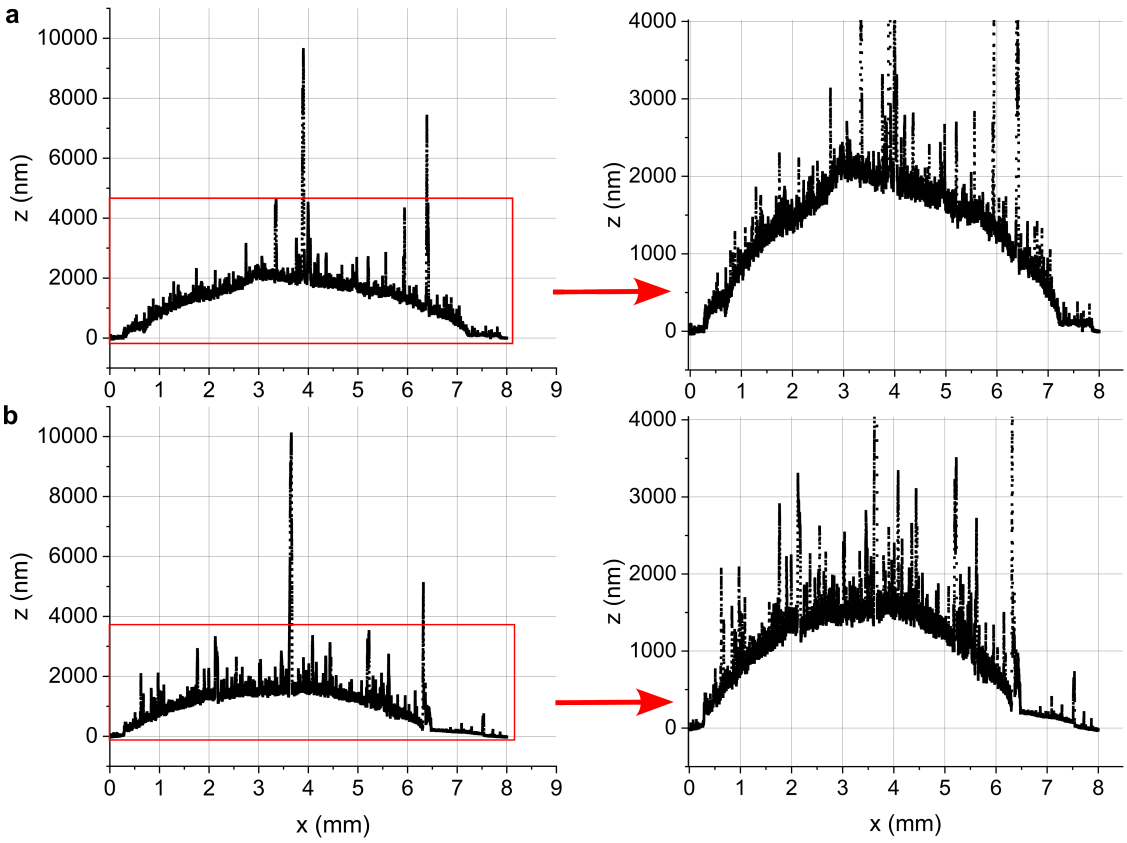

Figure 4.3 **a** and **b** exemplary show profilometer scans across the surface of 50 µL drop-casted PBDF-doped P3HT films on four-probe samples, once with the entire data on the left and once zoomed into the more homogeneous profile on the right. Both films show a number of particles with a much higher thickness, which correspond to impurities and foreign particles.

Figure 4.4 is a collection of thickness measurements across different PBDF-doped P3HT films. It can be seen that the error bars can exceed over 100% of their respective mean value (especially for sample #6), which aligns with the irregularities in the exemplary profiles from Figure 4.3. The overall mean thickness for the samples measured by a profilometer is 1773.25 nm. This value is used for the film thickness t for all σ-calculations according to Equation 3.6.

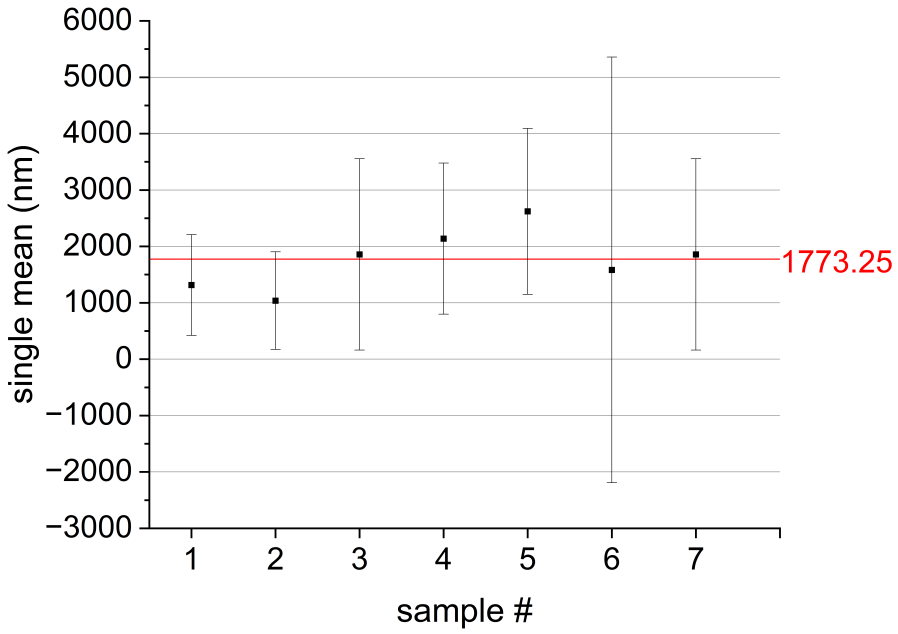

Figure 4.4 Selection of mean thickness values for each measured PBDF-doped P3HT film profile. Especially #6 shows a high fluctuation around its mean value. This is due to single inhomogeneities, wrinkles and particles that influence the result, as Figure 4.3 shows. The mean value for the scanned samples is at 1773.25 nm.

4.1.3 Atomic force microscopy (AFM)

Atomic force microscopy (AFM) was carried out with antimony n-doped silicon cantilevers with an aluminium coating (model TESPAW-V2 from Bruker). Those have a length of 127 µm, width of 35 µm and a spring constant of 42 N/m. Each scan was carried out at a slow rate of 0.977 Hz to achieve best possible resolution for the smallest features on the films. Figure 4.5 shows a collection of 2x2 μm^2 AFM scans of Fraunhofer substrates that are spin-coated with P3HT and PBDF-doped P3HT. Each image shown includes one chosen set of interdigits of the L = 20 µm contact pads. In addition, each image is taken on a separate Fraunhofer substrate, meaning that for each wt% of blended solution, a new entire substrate was coated. The height scans on the right were edited by using *NanoScope Analysis* with a 1st order Plane Fit, then a 1st order Flatten, to correct errors caused by tilt. Each scan was taken in between the interdigit fingers on the substrate, therefore not on the visible black clusters.

The images on the left show multiple features across different wt%. First of all, the pure P3HT substrate appears to be the only one with a homogeneous coverage over the entire surface. Starting from 1 wt% PBDF, some black aggregates do appear especially within the interdigited contacts. Considering that PBDF flakes of several hundred µm size are common, as discovered with the optical microscope, the build-up seen here is very likely to cause electrical shortcuts between the interdigit fingers.

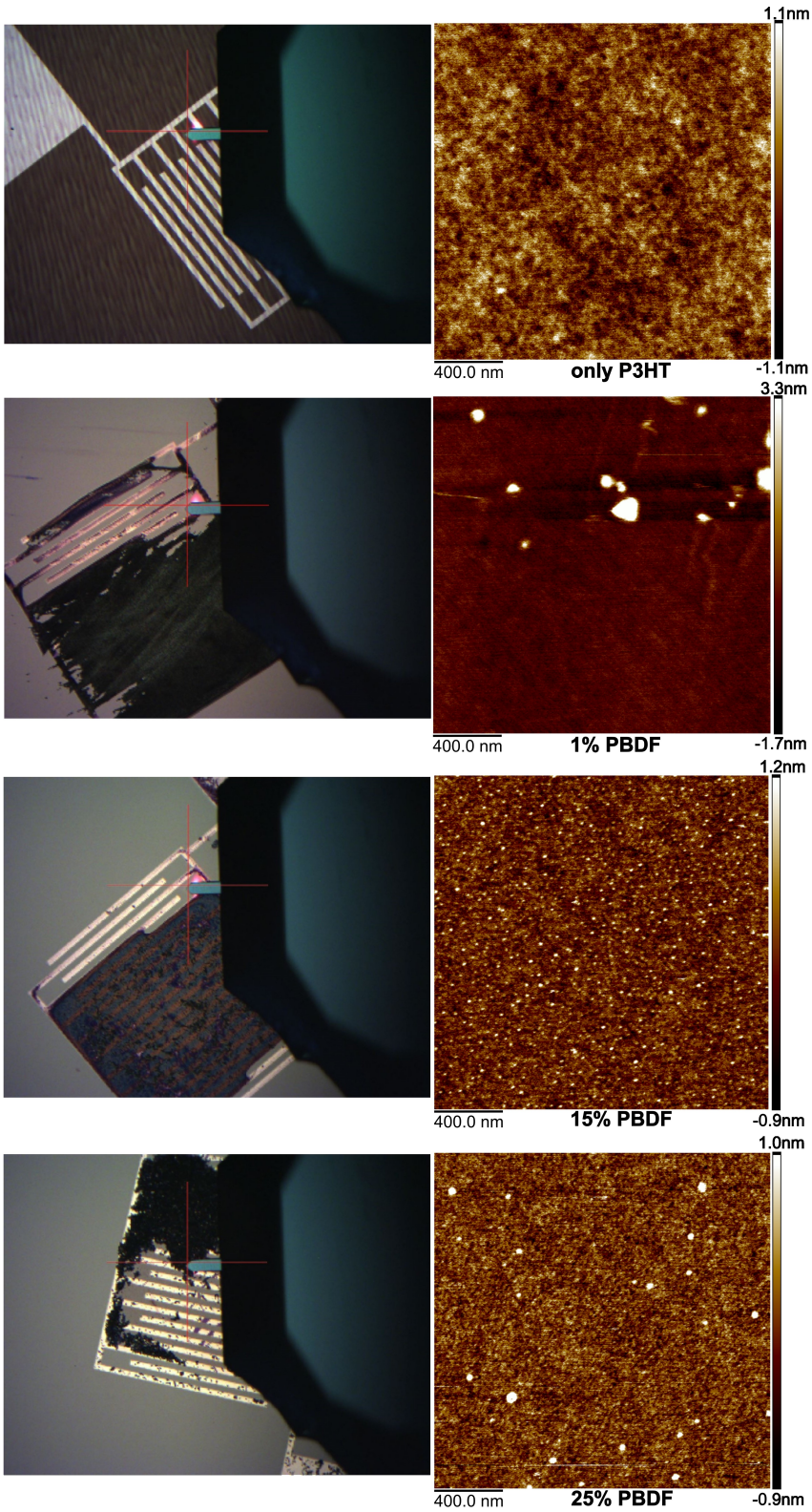

Figure 4.5 Collection of AFM scans of pure P3HT and PBDF wt% from 1 to 25, spin-coated on Fraunhofer substrates. The left side shows the positions of the AFM tip for the respective polymers. The scan for 25% was done outside the black layer, not exactly on the position shown. The right side shows the resulting height profiles.

Secondly, the quality of the solution blend appears to be the best for 15 wt% among the tested concentrations. This is due to the number, size and alignment of the visible white grain features among all scans. These grains can be both, contaminations and Si splinters, but also polymer particles. The overall structure of height differences in only P3HT differs from the rest and appears more amorphous, which is fitting with the overall sample coverage in the microscope image. Considering that the number of grains appears to be significantly higher for 15 wt%, compared to 25 wt% and especially 1 wt%, it can be concluded that the majority of those represent PBDF particles instead of contaminations. In addition, the size of white grains varies visibly more for 25 wt% compared to 15 wt%, which can be due to more alignment of PBDF strings that separate from the rest of the blend, leading to a less homogeneous blend of P3HT and PBDF. The blending quality can also be seen in the three different black flakes from 1 - 25 wt%. The flake for 15 wt% shows the smoothest edges and is transparent enough for the interdigits to be visible. The other two concentrations show rougher films with less defined edges. Especially for 25 wt%, the flake is spread-out with long PBDF strings that build up across all interdigits. This aligns with findings when attempting to drop-cast blended solutions of more than 30 wt% PBDF. The PBDF strings separate from the liquid rest of the solution after touching the surface.

Figure 4.6 shows AFM scans of the aggregates from Figure 4.5. The left images show edited height profiles, treated with the same fits as mentioned before. As the surfaces are much rougher than the previous ones, it is likely that the tip used for scanning broke off, resulting in poorer resolution. Nevertheless, the measured heights are up to 200 times higher than for the substrate scans (up to 234 nm, compared to ≈ 1 nm). Therefore, the right column shows the peak force error profiles of the same scans, which reveals more details about hidden surface structures. As can be assumed from the previously mentioned optical images, the sample with 15 wt% PBDF has the most homogeneous structure. This aligns with the maximum height difference found here, ranging from -63 to 77 nm for 15 wt%, compared to -234 to 231 nm for 25 wt% or -127 to 122 nm for 1 wt%. Regarding the peak force error profiles, it can be assumed that the number PBDF clusters rises from 1 to 15 wt%, while their size significantly increases from 15 to 25 wt%. Also, their distribution within the 2x2 µm^2 imaging range appears more homogeneous for 15 wt% compared to the other two, with regard to the elevations. This aligns with the found quadratic mean roughness R_q values for all samples, shown in Table 4.1.

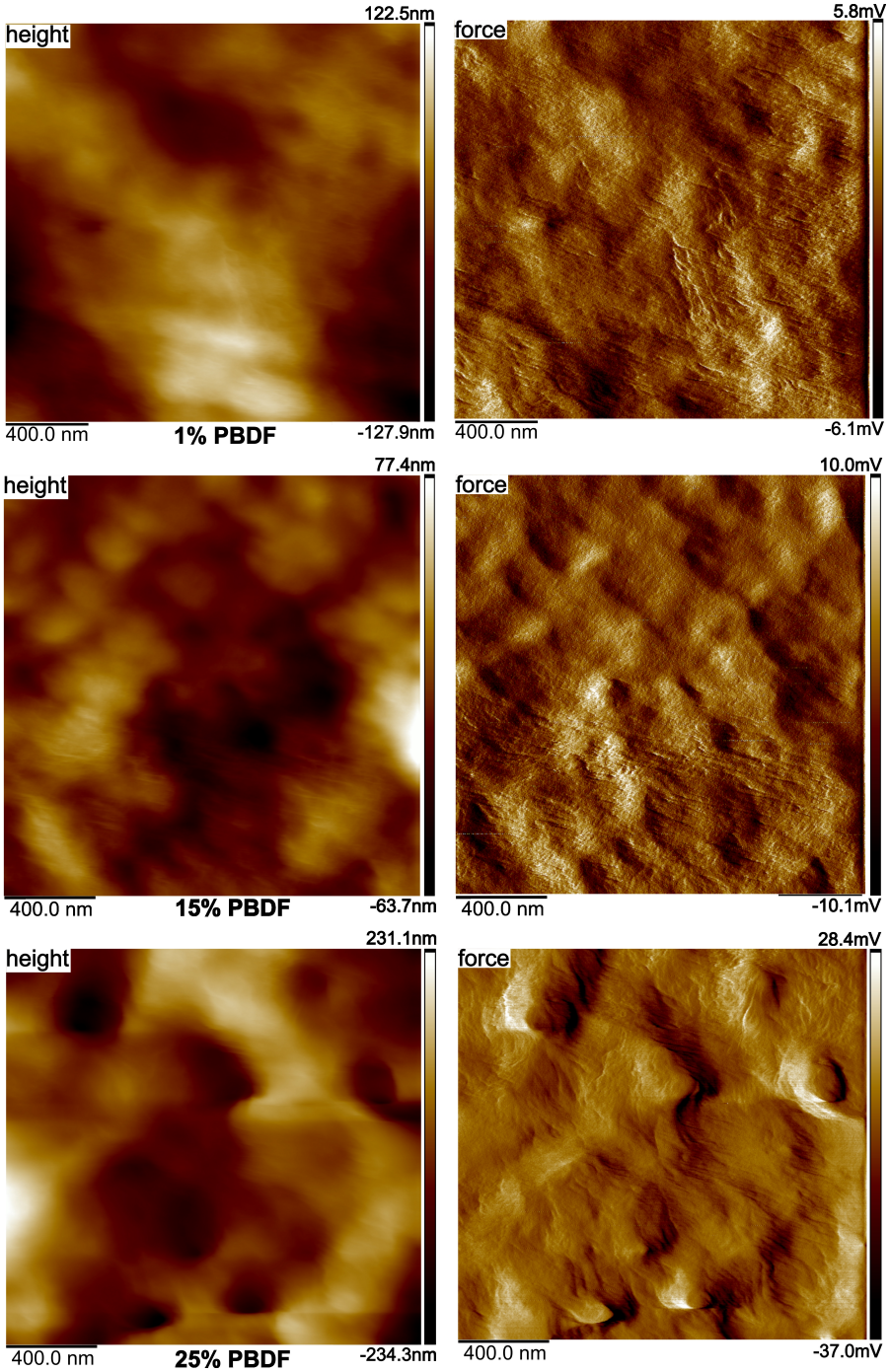

Figure 4.6 Comparison of the black layers of 1 to 25 wt% PBDF on the same substrates as shown in Figure 4.5. The left panels display the height profiles, which exhibit limited resolution due to significant surface roughness. The right panels show the corresponding peak force error images, providing enhanced visualization of surface features and finer structural details.

Table 4.1 Collection of all measured quadratic mean roughness R_q values of the AFM scans from Figures 4.5 and 4.6. The first section refers to AFM scans in-between the interdigit FET contacts and visible PBDF flakes. The 'PBDF flakes' section refers to scans directly on those flakes.

wt% PBDF	**R_q [nm]**
0	0.320
1	0.510
15	0.291
25	0.302
PBDF flakes	
1	37.1
15	18.8
25	72.0

The R_q values for all four surface scans between the fingers show similar values around 0.3 nm (with a slight exception of 1 wt%, due to two large grains). On the contrary, the aggregates show R_q values in range of factor 100 higher, with 15 wt% here again showing a significantly lower value with 18.8 nm, especially compared to 72.0 nm for 25 wt%.

4.2 Thermoelectric evaluation

4.2.1 Electrical conductivity evaluation

In order to obtain measurable results for each tested wt% of PBDF in P3HT solution, each wt% required fabrication of several drop-casted samples. The reason is a large variability with the drop-casted film distribution across all four-probe-contacts, an electrically conductive coverage between a gold contact and the polymer, as well as good electrical contact between the probes and the contacts. Figure 4.7 shows the I-V curves of the best tested samples for each wt%. In each case up to 25 wt%, the polarity of I switches between negative and positive voltages. The conductivity for more than a few volts on either side of 0 is nearly equal, and much lower compared to near proximity around 0. For wt% of 20 and 25, the curves start to rise with approximately equal slopes on either side, still with a similarly higher conductivity around 0. This trend complies with the ohmic behaviour that is observed for 50 wt% and pure PBDF. Overall, the conductivity increases gradually for higher wt% until it saturates at 100 wt% (meaning pure PBDF), as shown in Figure 4.11.

The reported conductivity of pure P3HT lies around 6.78 nS/cm at 293.2 K [31], which is by a factor of 22 - 30 smaller than the here measured values for negative and positive voltages. However, in the source study the conductivity has been determined through current step measurements with a waiting time of $\sim$2 s between the steps, instead of voltage sweeps as have been applied in this work. The conductivity of pure PBDF is reported with 2100 S/cm, with comparable four-probe-setup dimensions (W = 10 mm, L = 3.6 mm, t = 3342$\pm$156 nm), by the original study from Tang et al. [42], which is $\tilde{1}0$ times higher. Interestingly, for spin-coated single layers with thicknesses of 17 - 19 nm, the conductivity lies between 3100 - 3800 S/cm according to Ke et al. [12]. Additionally, the conductivity increases significantly up to 6100 S/cm for five stacked layers in the study. When only the thickness is considered, it would be expected that drop-casted films show at least similar, to higher conductivities than the thickest spin-coated films, as the thickness of the former is in the region of multiple micrometers, compared to tens up to hundreds of nanometres for spin-coated ones. However, drop-casting includes a greater variability in morphology and thickness due to uncontrolled solvent evaporation, inconsistent film formation dynamics and depends on human factors, such as positioning, drop-angle and drop-height. This can lead to non-uniform electrical and structural properties across samples, reducing reproducibility. In contrast, spin-coating provides more consistent processing conditions, enabling the formation of uniform films with better control over thickness and morphology, thereby enhancing reproducibility and comparability between samples. A study from Na et al. 2015 [43] tested multiple P3HT FET devices with different spinning times and reported standard errors of the mobilities of 11 - 25%, depending on the spinning time, but 72% for drop-casted devices. Also, for spin-coating shorter spinning times (of 3 s versus 60 s) led to significantly higher crystalline order within the polymer film, determined with two-dimensional grazing incidence X-ray diffraction (2D

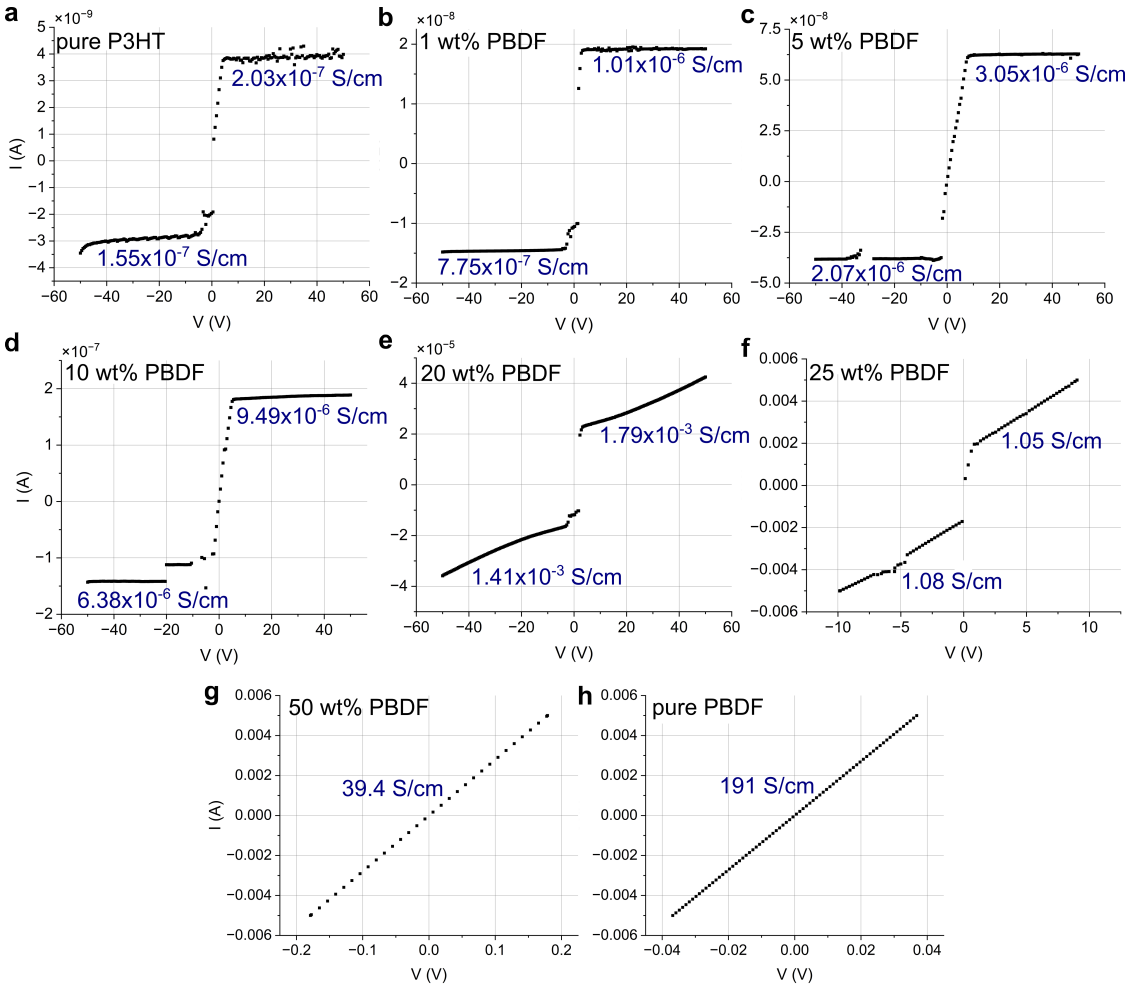

Figure 4.7 Comparison of I-V measurements of blended solutions for all tested weight percentages of PBDF-doped P3HT, from pure P3HT to pure PBDF. It is attempted to keep the voltage range between -50 to 50 V, although it needs to be reduced if the current runs into the set limit of 5 mA, as happens for 25 wt% and above.

GIXD). This led to higher mobilities in the 3 s spin-coated films (0.011 - 0.015 $cm^2V^{-1}s^{-1}$) versus the 60 s ones (0.002 - 0.004 $cm^2V^{-1}s^{-1}$). Consequently, drop-casted films have a higher variation of mobility between 0.002 - 0.019 $cm^2V^{-1}s^{-1}$.

4.2.2 Seebeck coefficient S evaluation

Verification of the setup with PEDOT:PSS

First of all, a verification for the Seebeck coefficient setup is carried out using PEDOT:PSS as a sample polymer due to its well-established values of S and the power factor PF in literature [2, 58]. Figure 4.8 shows two measurements conducted on the same sample of PEDOT:PSS, with a layout corresponding to Figure 3.7. The voltage-time diagrams on the left show the measured voltage profile over time for one continuous measurement each.

For Subfigure 4.8**a**, ΔT is first increased up to a value of ΔT = 30 K, then decreased to ΔT = 10 K. Hence, the evolution of the Seebeck coefficient S is determined for a rising and falling temperature. In 4.8**c**, ΔT is increased and stabilized around ΔT = 18 K first, then decreased near ΔT = 1 K. 4.8**a** and 4.8**c** show the respective plots for each averaged voltage level for the time interval indicated by red markers. A linear fit is used to approximate the averaged voltages with respect to the temperature, depicted in 4.8**b** and 4.8**d**. The slope corresponds to S. It differs by 0.36 µV/K between both fits with 18.83 µV/K and 18.47 µV/K respectively. Jing et al. [2] reports a S value of 6.7 µV/K for single-layer inkjet-printed PEDOT:PSS films on glass and mentions values between 10 - 49 µV/K for inks from different fabricators, scientific reports and substrates. Ink from Sigma-Aldrich on glass was reported with S = 49 µV/K [58]. One study reports S with 11.6 µV/K for pristine PEDOT:PSS from drop-casting [59]. Therefore, the measured values fit the expectations from literature.

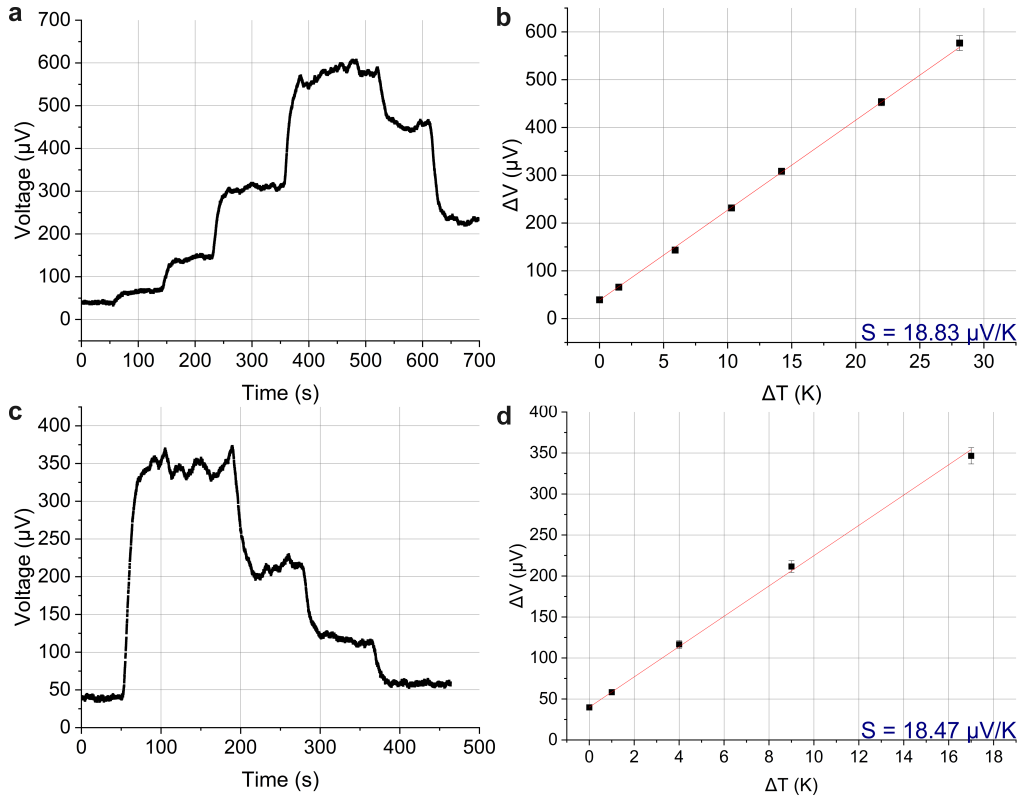

Figure 4.8 Seebeck coefficient measurements on PEDOT:PSS. **a** and **c** show the measured voltage profiles over time with increasing temperature levels in steps of single-digit kelvin. **b** and **d** show the averaged voltage levels over the corresponding temperature gradients with a linear fit. The obtained slope is equal to the Seebeck coefficient.

Results for PBDF-doped P3HT

As for the four-probe conductivity measurements, several samples per wt% were required to obtain measurable results, for similar reasons. In addition, the contact between the thermocouples and gold pads is more sensitive to vibration than the probe needles used for voltage and current sensing. Therefore, the measurements were conducted on an optical table to dampen vibrations caused by humans and devices around the setup.

The results for tested wt% from 1 to 25 and pure PBDF are shown in Figure 4.9. Contrary to the obtained values for σ, the absolute value for S decreases from 160.6 µV/K for 1 wt% down to 18.4 µV/K for 5 wt%, from where it appears to stabilize around 20 - 27 µV/K. Data for S could only be obtained up to 32 wt%, as the blended solution of both polymers begins to disperse for higher wt% and becomes hardly measurable. An exception is the value of 50 wt% that was successfully measured in four-probe-setup, but unsuccessfully in the Seebeck setup. PBDF itself exhibits a slightly lower value of $|S|$ with 14.9 µV/K, which is comparable to 21 µV/K in the original study from Tang et al. [42].

Taking into account the sign of S, only wt% 1 and 5 exhibit a positive slope, indicative of p-type conduction behavior, similar to that observed in PEDOT:PSS. Starting from 10 wt%, the slope switches to negative, which is indicative for n-type materials like PBDF.

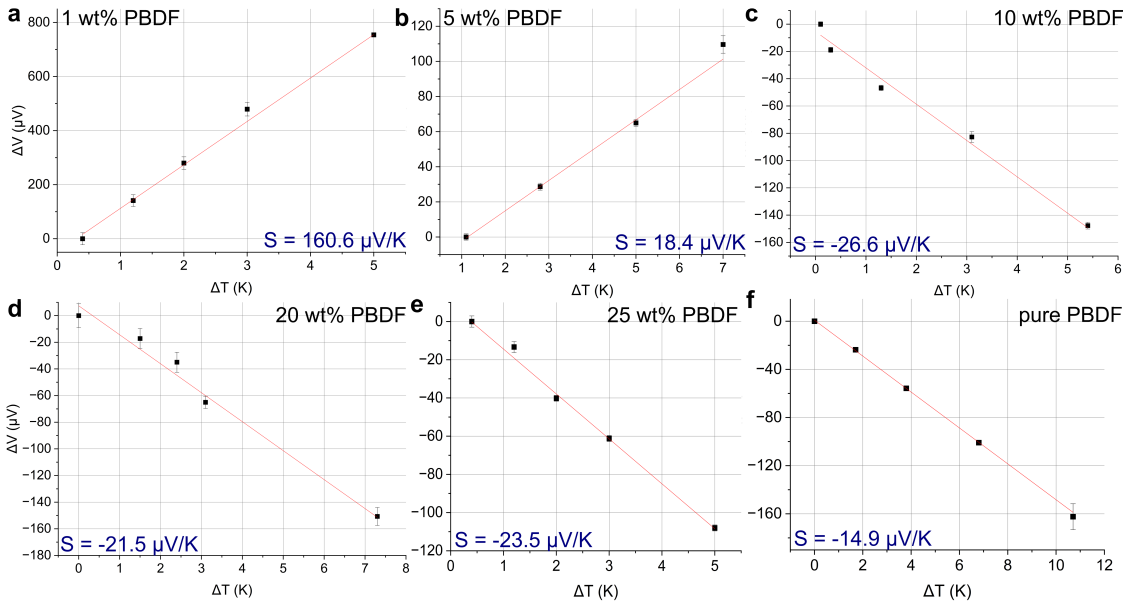

Figure 4.9 Collection of Seebeck coefficient S measurement results for all tested weight percentages of PBDF-doped P3HT. PBDF wt% of 1 and 5 have a positive slope, as the p-type PEDOT:PSS in 4.8, while any higher tested percentage results in a negative slope, as expected from a n-type material, which also occurs for pure PBDF.

Interestingly, the value of S of P3HT itself could not be measured with the available setup, as figure 4.10 shows. Its voltage profile over time only results in noise, not in distinctive voltage

levels, as in figure 4.8. According to Zou et al. [46], pristine P3HT has a relatively high S of 1550±125 µV/K. This leads to the conclusion that PBDF achieves a doping effect on P3HT up to 5 wt%, while holes are still the main charge carrier type. Starting with 10 wt%, the slope and therefore main charge carrier type, switches to electrons as for pure PBDF.

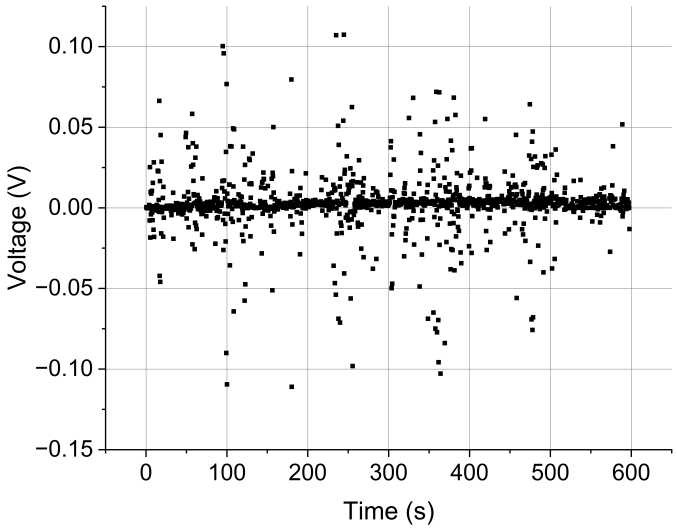

Figure 4.10 Voltage profile versus time elapsed with increasing temperature steps for pure P3HT. Only noise could be measured, when using the same method as for all measurements of S. For all other blends and PBDF, the V-t profile shows distinctive steps like PEDOT:PSS in Figure 4.8.

4.2.3 Overall results for electrical conductivity, Seebeck coefficient and power factor

Figure 4.11 shows a summary of the obtained conductivity σ values in **a** and combined Seebeck coefficient S and power factor PF values in **b**. As previously mentioned from the analysis of σ, σ rises gradually and saturates the closer it gets to 100 wt% (meaning pure PBDF). The terms 'negative' and 'positive' correspond to the sign of current I in Figure 4.7. As expected, these two values do not differ much and overlap with their respective error bars. Therefore, PF in **b** is calculated using the slightly better performing 'positive' values.
Although the power factor depends quadratically on S, with $PF = \sigma S^2$, due to the large increase of σ over multiple orders of magnitude and S remaining relatively stable, PF also increases with wt%. Studies suggest an empirical relation of $S \propto \sigma^{-1/4}$ from analysis of multiple p-type polymers, such as PEDOT, polythiophenes, PA/PANI, CNT composite, a few n-type materials of the same categories [25, 29], and also [6,6]-phenyl-C61-butyric acid methylester (PCBM) in doping [45]. Hence, a relation of $PF \propto \sigma^{1/2}$ is reported. Deriving a relation of thermopower as a function of conductivity σ for various transport mechanisms is non-trivial, and many proposed relations of $S(\sigma)$ are not derived from models, but fit the data and qualitatively related to transport. [29]

[htb]

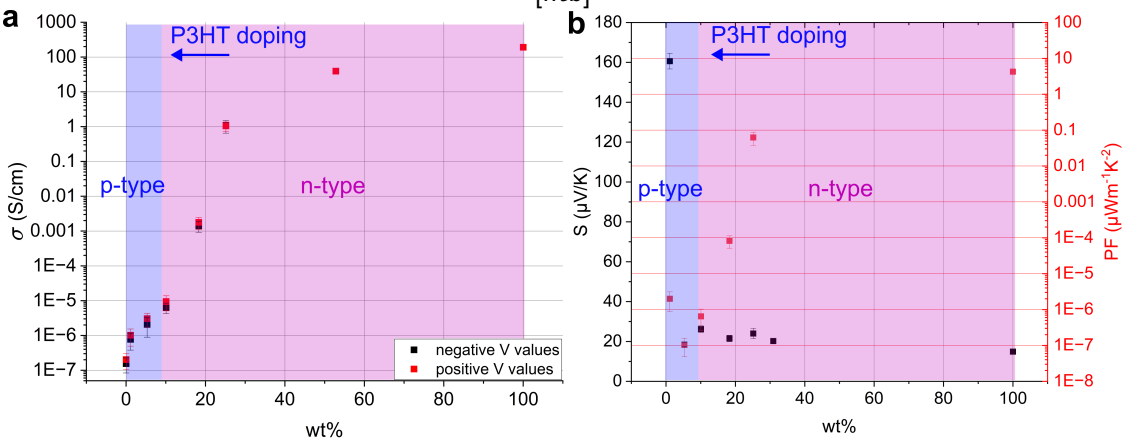

Figure 4.11 Summary of the achieved values for conductivity σ in **a** and absolute values of Seebeck coefficient S (black), together with power factor PF (red) in **b**. The terms 'negative' and 'positive' correspond to the sign of I in Figure 4.7. The vertical axis for σ in **a** is logarithmic, like the red vertical axis for PF in **b**. The blue and violet regions mark the expected wt% of PBDF, until which P3HT is doped while remaining a p-type semiconductor, before n-conduction from PBDF becomes predominant.

The mobility of carriers in organic materials is related microscopically to the electronic coupling between molecules and interchain transport in polymers, and macroscopically to the ability of these carriers to cross domain boundaries, similar to polycrystalline inorganic semiconductors. Thus, the observed electrical conductivities of organic materials can vary profoundly depending on the processing conditions. Considering the most basic model of thermopower in homogeneous materials, σ and S are dictated by the density of states (DOS) and position of E_F, whereas only carriers close to E_F contribute to transport. S can be defined as the average entropy per charge carrier in the form of, [23, 25]

$$S = -\frac{k_B}{e} \int \frac{E - E_F}{k_B T} \frac{\sigma'(E)}{\sigma} dE \tag{4.1}$$

which is equivalent to Equation 2.16. It follows, that the larger the difference between the energy of conducting carriers and the Fermi level, the larger the Seebeck coefficient. If σ and, hence, the charge carrier concentration, increases, the Fermi level E_F is effectively shifted towards the conduction band edge (in case of n-type doping), or valence band edge (in case of p-type doping). The closer E_F gets to either edge, the smaller the energy difference $E - E_F$ becomes, as more carriers participate in transport. The smaller energy difference results in less generated voltage ΔV per unit temperature difference ΔT, which leads to a lower value of S. [44]

Comparing the results of all three quantities (σ, S and PF), the graphs can be divided into two regions of predominant p-type and n-type conduction. As the Seebeck results show, the predominant charge carrier type switches from 5 to 10 wt% PBDF. The precise wt% can lie in-between these values. This is graphically visible in a change of trend, as the conductivity rises by about two orders of magnitude up to 10 wt%, but five orders for higher values up to 25 wt% alone. The first value of PF at 1 wt% is higher than the two following ones due to a potential doping effect in P3HT, which leads to both, a $\sim$8 times higher S compared to the following PBDF-predominant values and $\sim$10 times higher σ compared to pure P3HT. This effect is also confirmed by FET measurements in the follow-up section. Apart from that, as explained by Equation 4.1, the fact that the poorly conducting P3HT has a Seebeck coefficient that is more than 100 times higher than that of the highly conducting PBDF (1550 versus 14.9 µV/K) appears reasonable.

4.3 Field-effect transistor (FET) analysis

In this section, the I-V results for the drain-source and gate-source channels of both, the shadow mask fabricated 2 mm channel length and Fraunhofer-made FET samples are evaluated and compared. The results are divided upon drop-casted and spin-coated samples, as both methods lead to significantly different curves. The representation of the shown quantities is as follows: Drain-source current and voltage I_{ds},V_{ds}, gate-source current and voltage I_g,V_g. All measurements were performed under nitrogen atmosphere, inside a glovebox (H_2O and O_2 levels $<$0.1 ppm).

Drop-casted samples

Drop-casting on multiple samples of both categories (shadow mask and Fraunhofer) did not prove reliable. For each tested sample, I_{ds} was either very low, below 1 nA, or within a nominal range up to 1 µA, but in each case with comparable I_g values. Drain currents below 1 nA in a supposedly conductive material (and in an FET geometry with W = 10 mm) indicate poor electrical contact between the measurement probes and the tested device. This happens especially for drop-casted Fraunhofer samples, as the drop size is large compared to the electrodes, which leads to entire electrode pads being covered by polymer. This situation is depicted in Figure 4.12. For the second case, if $I_{ds} \approx I_g$, it indicates electrical leakage through the insulating layer. Consequently, the recorded I_{ds} values are likely compromised and do not reflect the intrinsic charge transport within the polymer channel.

Spin-coated samples

Spin-coating polymer blends onto the Fraunhofer substrates, on the other hand, proved useful and delivered more ideal results. For each sample, the liquid polymer blends were deposited on the substrates in one drop of 100 µL and spin-coated in two steps of 500 rpm for 5 s

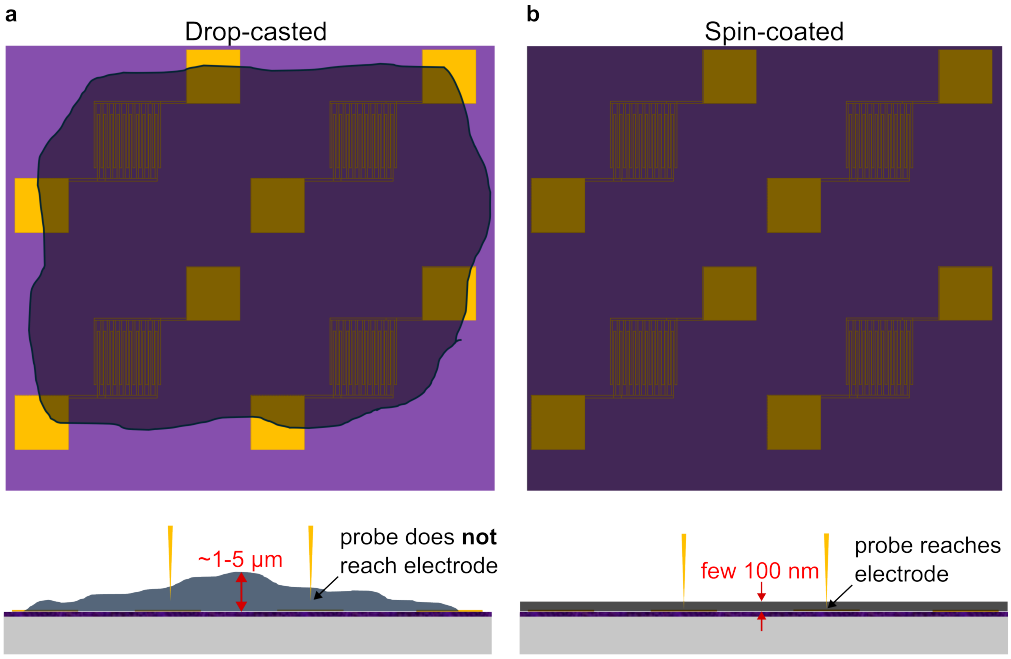

Figure 4.12 Schematic visualization of Fraunhofer substrates covered by drop-casted polymer solution in **a** versus spin-coated one in **b**. The side views in the lower part show the difference in homogeneity and thickness of the resulting dried films for both methods, which mostly leads to the tip not being able to reach the gold contacts for drop-casted samples.

first, then 3000 rpm for 55 s. Each tested sample shown in the figures is prepared with a pre-treatment of OTS prior to spin-coating, as it delivered more consistent results.

Figure 4.13 shows I_{ds}-V_{gs} graphs for different V_{ds} voltages of pure P3HT coated samples in **a** - **c** and 1 wt% PBDF samples in **d** - **f**. For all samples the gate effect is well visible for negative V_{gs} values, which fits the behavior of p-FETs as it is also expected of P3HT [47,48]. The gate-effect occurs in both directions of V_{ds}, although higher I_{ds} values are achieved for positive V_{ds}. When comparing the maximum I_{ds} among the P3HT samples from L = 20 µm to L = 5 µm, these increase by factors of 2.9 and 9.2 with respect to 20 µm. An increase in current for lower channel lengths, and therefore lower resistance, is reasonable. The same effect occurs with 1 wt% PBDF to a greater extent with increasing factors of 10 and 32, with respect to L = 20 µm. When comparing the maximum I_{ds} values for each channel length of P3HT with the corresponding PBDF-doped one, for 20 µm the doped sample has twice as much current, the 10 µm sample 7.5 times as much and the 5 µm sample with $\tilde{7}$.3 times. Taking into account the linear and saturation regimes, each P3HT sample exhibits electric channel formation starting around 20 V towards negative voltages, while this already happens starting from 40 V for the doped samples. In addition, the doped devices demonstrate an extended linear regime relative to the undoped ones. At voltages below -40 V, the P3HT curves begin to saturate (which is particularly evident for V_{ds} = 70 V), while the PBDF-doped

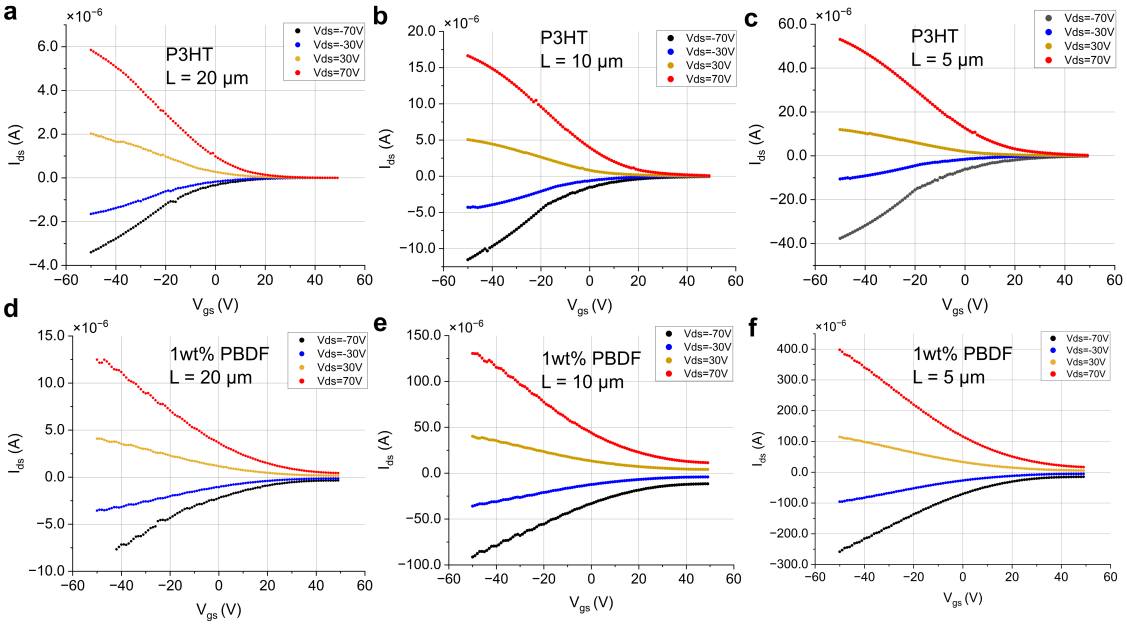

Figure 4.13 I_{ds}-V_{gs} sweeps with constant V_{ds} levels of spin-coated P3HT and 1 wt% PBDF solution, for channel lengths 5, 10 and 20 µm. Each color represents a different V_{ds} value. The devices with 1 wt% PBDF achieve higher I_{ds} than their P3HT counterparts and do not show saturation behavior for V_{gs} = -50 V yet. The mobilities of these curves are shown in Table 4.2.

devices maintain a predominantly linear response under the same conditions.

Table 4.2 Linear mobilities μ_{lin} of FET samples with pure P3HT and 1 wt% PBDF on two separate Fraunhofer substrates for V_{ds} voltages from -70 to 70 V and channel lengths 5, 10 and 20 µm.

	P3HT	**1 wt% PBDF**
in $cm^2V^{-1}s^{-1}$	**5 µm**	
μ_{lin}(-70 V)	0.00399	0.03746
μ_{lin}(-30 V)	0.00243	0.03304
μ_{lin}(30 V)	0.00245	0.03795
μ_{lin}(70 V)	0.00430	0.05663
	10 µm	
μ_{lin}(-70 V)	0.00242	0.01112
μ_{lin}(-30 V)	0.00208	0.01072
μ_{lin}(30 V)	0.00207	0.01300
μ_{lin}(70 V)	0.00274	0.01789
	20 µm	
μ_{lin}(-70 V)	0.00229	0.00291
μ_{lin}(-30 V)	0.00232	0.00271
μ_{lin}(30 V)	0.00196	0.00270
μ_{lin}(70 V)	0.00234	0.00367

From the linear region of each sample, the charge carrier mobility μ_{lin} can be extracted, according to Equation 2.2. The mobility values of each tested V_{ds} step are listed in Table 4.2. At first, only the regular devices, in the two middle columns, will be discussed. Comparing μ_{lin} between only P3HT and 1 wt% PBDF, the values of PBDF-doped samples are in the order of 5 - 10 higher for $L = 5$ and 10 µm, which complies with the higher I_{ds} values as beforementioned. With increasing L, μ_{lin} decreases further in case of 1 wt% PBDF, much less so for pure P3HT, for which the values remain similar, except for slightly higher ones for 5 µm. For 20 µm, the mobilities of P3HT and PBDF-doped samples are almost similar, although the latter ones remain higher. Overall, the values of μ_{lin} are around a factor of 10 smaller than those reported Wang et al. in 2003 with comparable devices (bottom-contacts, spin-coating and dissolved in chloroform) [48], although Bao et al. in 1996 reported $9.2 \cdot 10^{-3}$ $cm^2V^{-1}s^{-1}$ for spin-coated devices [47] which is still higher, but in the same order of magnitude.
Besides μ_{lin}, the on- and off-currents I_{on} and I_{off}, and there within their ratio I_{on}/I_{off}, can be extracted from the same graphs. The values have been extracted for $V_{ds} = 70$ V and are listed in Table 4.3. It shows, that the values for both, I_{on} and I_{off}, increase for 1 wt% PBDF. However, while the increase of I_{on} is a factor of 7.8 for the 10 µm channel, I_{off} increases by 153.7 times. The largest difference in increasing factor occurs for the 20 µm channel, as the factor is only 2.1 for I_{on}, but 264.5 for I_{off}. This indicates effective doping of P3HT in the form of injecting free charge carriers, especially as in an off-state the current I_{off} is significantly higher with PBDF, than without it. As I_{off} is increased much more than I_{on}, in conclusion the on/off ratio in pure P3HT is up to a factor of 10.3 higher compared to 1 wt% PBDF on the 5 µm FET. The P3HT-FET of 20 µm shows a relatively high on/off ratio with

3518.44, indicating a well-functioning device. 1 wt% PBDF lowers the on/off ratio in all FETs to values from 11.48 to 28.39, which is especially low in case of the 20 µm FETs.
The intercept of the same linear fit used to extract μ_{lin} with V_{gs}, delivers the threshold voltage V_{Th}, which is also listed in Table 4.3. Upon doping with PBDF, a shift toward more positive voltages is observed, indicating a shift of the Fermi level toward the HOMO of P3HT. In other words, shifting toward more positive voltages means that a stronger positive gate bias to deplete the p-type carriers and turn the device off is required. This interpretation is supported by the observation that the gate-induced channel modulation still occurs at negative gate voltages.

Altogether, the I_{on}/I_{off}-ratio for pure P3HT FETs is comparable to results from Wang et al. 2003 [48] and Jiang et al. 2011 [49]. The on/off-ratio for Wang et al. before a heat treatment is in the range of 80 - 1000 for channel lengths of 5 - 25 µm (and a comparable SiO_2 thickness of 200 nm), which is a similar trend and range as for the devices in this work, although their linear mobilities are by a factor of 40 - 50 higher than those in this work. Jiang et al. compared the values for different concentrations of P3HT from 0.5 - 8 mg/mL, all on substrates with SiO_2 oxides of 300 nm. They report a maximum on/off-ratio of $\sim 1.2 \cdot 10^4$, paired with their highest mobility of $1.4 \cdot 10^{-2}$, which both decrease for lower and higher concentrations. Considering that a constant concentration of 5 mg/mL is used in this work, their reported on/off-ratios of ∼530 to ∼91 for 4 and 8 mg/mL respectively, are comparable to the values for channel lengths 5 and 10 µm here.

Higher concentrations of PBDF do not exhibit consistent results, unlike 1 wt% PBDF compared to pure P3HT. Figure 4.14 show FET examples with 10 and 15 wt%. For all FETs, the current limit is set to 10 mA. **a** shows one sample with $L = 5$ µm, **b** - **c** show two different samples with $L = 10$ µm for 10 wt% PBDF. Comparing **a** and **c**, both devices enter the limit for I_{ds}, but for approximately twice the V_{ds} for 10 µm, compared to 5 µm. Regarding **b**, for the same V_{ds} levels the second 10 µm sample on the same substrate, I_{ds} only reaches about $1/10$ of the values compared to those of $L = 5$ µm and about $1/4$ of those of the second 10 µm sample. Subfigures **d** - **f** show channel lengths 5, 10 and 20 µm for 15 wt% PBDF. **d** has a similar behavior to **c**, although with lower I_{ds} for the same V_{ds}. **e** is an exception with respect to the other doped FETs, showing similar behavior to 1 wt% PBDF samples, although the I_{ds} values are 10 times lower than those of regular P3HT in this work.

Overall, the majority of FETs tested for 10 wt% PBDF and beyond show no modulation of the drain current upon application of a gate bias which is indicative of a conductive behavior that starts at that doping concentration. In fact, I_{ds}-V_{gs} characteristics where the current level is high and it does not depend on the gate field are typical for conductive materials, such as pristine PBDF. Based on optical and atomic force microscopy images, the electrical performances of FET devices were found to depend on the number and size of PBDF aggregates that accumulate on the interdigit contacts. PBDF aggregates that reach lengths of multiple

Table 4.3 Comparison of the I_{on} and I_{off} values, as well as their ratio I_{on}/I_{off} and threshold voltage V_{Th} of P3HT and 1 wt% PBDF FETs.

for V_{ds}=70 V	**P3HT**	**1 wt% PBDF**	**ratio: 1 wt% PBDF/P3HT**
I_{on}	in A		
5 µm	$5.3092 \cdot 10^{-5}$	$3.9794 \cdot 10^{-4}$	7.4952
10 µm	$1.6646 \cdot 10^{-5}$	$1.3049 \cdot 10^{-4}$	7.8391
20 µm	$5.8498 \cdot 10^{-6}$	$1.2488 \cdot 10^{-5}$	2.1349
I_{off}	in A		
5 µm	$2.2385 \cdot 10^{-7}$	$1.6800 \cdot 10^{-5}$	75.0539
10 µm	$7.3913 \cdot 10^{-8}$	$1.1362 \cdot 10^{-5}$	153.7318
20 µm	$1.6626 \cdot 10^{-9}$	$4.3988 \cdot 10^{-7}$	264.5715
I_{on}/I_{off}			
5 µm	237.17	23.68	0.09984
10 µm	225.21	11.48	0.05097
20 µm	3518.44	28.39	0.00807
V_{Th}	in V		
5 µm	12.6	17.5	1.3888
10 µm	12	21	1.75
20 µm	10.2	16.4	1.6078

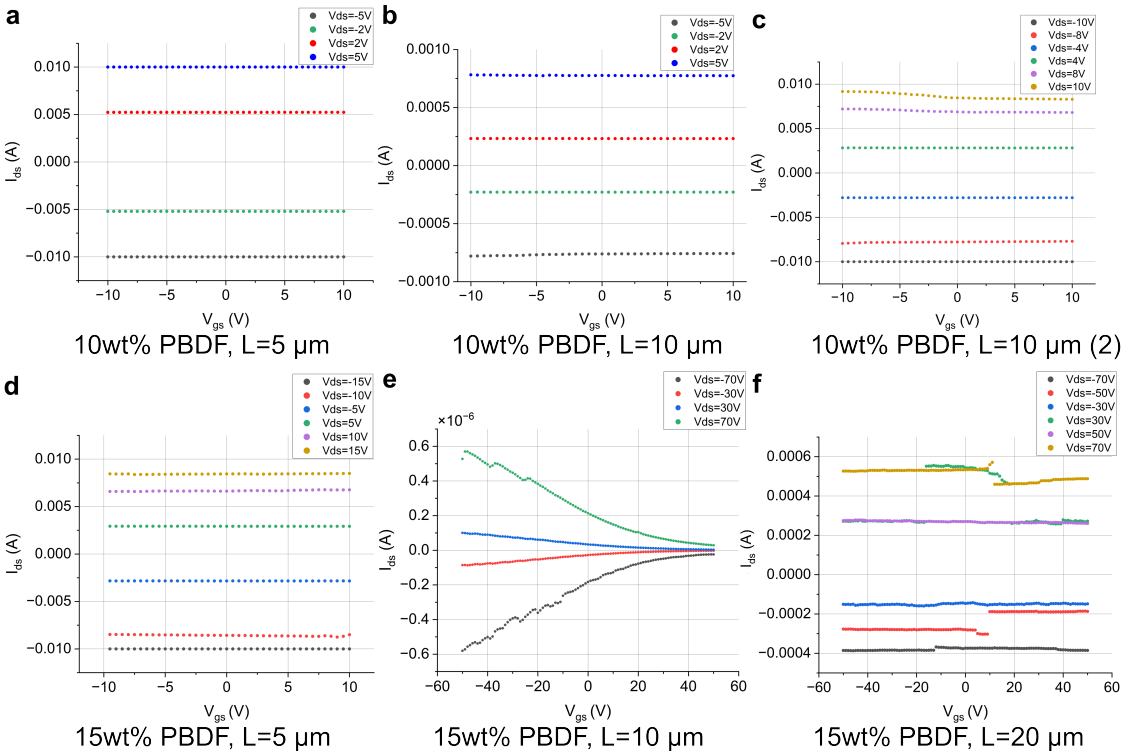

Figure 4.14 I_{ds}-V_{gs} sweeps with constant V_{ds} levels of spin-coated 10 and 15 wt% PBDF solution. **a** - **d** and **f** show no modulation of the drain current upon application of a gate bias due to accumulation of PBDF flakes in the interdigits. **e** shows modulation of I_{ds} upon applied V_{gs}, as occurs for FETs with only P3HT or 1 wt% PBDF coating.

hundred of micrometers can likely bridge 20 µm long channels, thereby suppressing/masking the field effect. In some cases, such as 4.14**e**, interdigitated electrodes are only partially bridged - or not bridged at all - which results in a gate-controlled transport for lower wt% down to pristine P3HT.

In combination with the results for σ and S in the previous section, this reinforces the conclusion that PBDF has a strong doping effect on P3HT , by boosting its mobility already at 1 wt% PBDF. Potential higher doping effects up to 10 wt% can most likely not be verified with the present FET layout, as the size of PBDF flakes is too large compared to the maximum interdigitated channel length of 20 µm.

5 Summary and Outlook

The goal of this work was to achieve an improvement of the power factor PF of the p-type semiconductor P3HT by doping through blending with the n-type conductor PBDF. Results show that PF can be improved by a factor of $3 \cdot 10^4$, from $2.0 \cdot 10^{-6}$ $\mu W m^{-1} K^{-1}$ of 1 wt% PBDF in P3HT to 0.06 $\mu W m^{-1} K^{-1}$ of 25 wt% PBDF for drop-casted PBDF-doped P3HT on glass substrates. This improvement comes from a rise in electrical conductivity σ by $5.5 \cdot 10^6$ S/cm from $2.0 \cdot 10^{-7}$ S/cm to 1.1 S/cm, starting from pure P3HT alone, as the absolute Seebeck coefficient $|S|$ remains at the same level of around 22 µV/K, except for 1 wt% PBDF with 160.6 µV/K and pure PBDF with 14.9 µV/K. The analysis of S with respect to the slope showed, that the values of σ,S and PF can be divided into two regions of predominant p-type and n-type conduction. The predominant charge carrier type switches between 5 to 10 wt% PBDF from P3HT-typical p- to PBDF-typical n-type conduction. The increase in σ for 1 and 5 wt%, while the blend remains p-type, indicates doping of P3HT without PBDF becoming the predominant conducting polymer.

The linear charge carrier mobility μ_{lin} could be determined for P3HT and 1 wt% PBDF, while higher wt% of PBDF delivered inconsistent results that show either similar responses to applied gate voltage V_g or no gate response at all, as is the case for ohmic behaving pure PBDF. μ_{lin} for 1 wt% shows an increase by 5 to over 10 times the values of pure P3HT for channel lengths of 10 µm and 5 µm respectively and slightly increased mobility values for 20 µm. The factor of increased μ_{lin} from P3HT to 1 wt% PBDF appears to halve for a doubling of channel length. In addition, within the measured range of V_{gs} from -50 to 50 V, the FETs with pure P3HT begin to saturate at the outmost voltages, whereas FETs with 1 wt% PBDF do not saturate yet.

Considering the dimensions of the layouts for the shadow masks, for this work a length of 2 mm was chosen as acceptable compromise between thermoelectrically measurable samples and good dissolved polymer coverage of the electrodes. Using smaller channel lengths of possibly 1 mm would be favourable, to not lose too much charge carrier mobility for accurate measurements. Furthermore, the drop-casting and spin-coating methods should be improved. For the former, the substrates can be preheated, prior to drop-casting, to prevent applied solution from flowing over the contact or substrate edges. In this work, glass substrates were heated to 30°C for P3HT and up to 10 wt% PBDF and up to 50°C for 20 wt% and beyond. This is due to the relatively low boiling point of chloroform at 61°C, combined

with a high vapor pressure of 158.4 Torr [60]. On the contrary, DMSO has a high boiling point at 189°C [61], which increases the time that is required to evaporate the solvent. The chosen hot plate temperature is purposefully not higher than 50°C to prevent any unforeseeable reactions and rearrangements within the polymer blend. Further tests with batches of samples for different (pre-)heating temperatures can give more control about the coating behavior of the film, as well as possible changes in polymer properties when the here tested temperatures are exceeded. Also, so far the films are applied in accumulated layers of 10 µL, instead of one drop of the desired quantity. The reason is once more the liquidity of applied films, which requires each layer to partially dry before applying the next one. It is desirable to find a method to dry the applied film in one drop which only covers the electrodes quickly, to improve reproducibility and homogeneity without creating wrinkles between film layers.
For the latter, spin-coating, also the homogeneity of the film layer should be improved for PBDF-blended solutions. Pure P3HT solution mostly spreads evenly across the substrate, including the interdigit contacts. When PBDF is added, its poor solubility prevents a homogeneous coverage across the interdigits, as microscope and AFM images have shown. Hence, the FET devices that are created during the coating can have significantly different output behavior, depending on the size and amount of PBDF particles, all on the same substrate. On a macroscopic scale, the spin parameters can be further fine-tuned around the applied two steps of 500 rpm for 5 s and 3000 rpm for 55 s. However, a more beneficial approach would be to improve the solubility of PBDF either through a filtration, a treatment of DMSO or finding a better suitable solvent. Also, a series of tests of PBDF solutions of lower concentrations by adding more DMSO can prove useful. Our supplier at the *Université Paris Cité* tested multiple solvents besides DMSO, such as acetone, acetonitrile, ethyl acetate and dichlorobenzene. Out of those, DMSO turned out to be the best functioning one, most likely due to its property of being polar and aprotic, which means that it does not donate H-ions. Considering filtration, polyvinylidene difluoride (PVDF) filters with pore sizes of 0.2 and 0.45 µm were tested on PBDF in DMSO solution of the regular 7 mg/mL. It was not possible to squeeze the solution through a syringe through the filters, which suggests common particle sizes $>$0.45 µm as it is also expected from the microscope images.

Considering the FET analysis, further investigation on PBDF-doped FETs with 1 wt% and around this value should be carried out, as this percentage yielded the most consistent and enhanced doping results. It is desirable to increase both, the number of tested substrates, as well as series of tests with wt% of e.g. 0.9, 0.8... and 1.1, 1.2... . In order to achieve possibly higher enhancements in I_{ds} output and mobility for higher PBDF concentrations, the issue of poor solubility would need to be improved first. Furthermore, also wt% between 5 and 10 should be investigated in smaller steps to determine the maximum possible doping saturation of PBDF, while the blend keeps p-type conduction.
Additionally, the spin-coating process can be further optimized with regard to the spinning

time and possibly the number of applied layers. As the study from Na et al. 2015 [43] mentioned in section 4.2.1 reports, much shorter spinning times of 3 s, instead of 60 s, lead to significant beneficial results on the long-range crystallinity and hence mobility and achievable I_{ds} current in I_{ds}-V_{ds} sweeps. In addition, regarding the results of Jiang et al. 2011 [49], who reported a maximum saturation mobility μ_{sat} and I_{on}/I_{off} ratio for 2 mg/mL P3HT in chloroform, testing FET devices for that concentration region can also be beneficial.

Bibliography

[1] S. Bruckner, "Industrielle Abwaerme in Deutschland," *Technische Universitaet Muenchen*, 2016.

[2] J. Jing, L. Chopplet, N. Battaglini, V. Noël, B. Piro, T. Leydecker, Z. Wang, G. Mattana, and E. Orgiu, "The role of substrates and electrodes in inkjet-printed PEDOT:PSS thermoelectric generators," *J. Mater. Chem. C*, vol. 12, no. 17, pp. 6185–6192, 2024. [Online]. Available: https://xlink.rsc.org/?DOI=D4TC00505H

[3] Y. Ma, Y. Zou, C.-a. Di, and D. Zhu, *Introduction of Organic Thermoelectrics*. WILEY-VCH GmbH, 2023.

[4] I. H. Eryilmaz, Y.-F. Chen, G. Mattana, and E. Orgiu, "Organic thermoelectric generators: working principles, materials, and fabrication techniques," *Chem. Commun.*, vol. 59, no. 22, pp. 3160–3174, 2023. [Online]. Available: https://xlink.rsc.org/?DOI=D2CC04205C

[5] G.-H. Kim, L. Shao, K. Zhang, and K. P. Pipe, "Engineered doping of organic semiconductors for enhanced thermoelectric efficiency," *Nature Mater*, vol. 12, no. 8, pp. 719–723, Aug. 2013. [Online]. Available: https://www.nature.com/articles/nmat3635

[6] A. Zvezdin, E. Di Mauro, D. Rho, C. Santato, and M. Khalil, "En route toward sustainable organic electronics," *MRS Energy & Sustainability*, vol. 7, no. 1, p. 16, Jul. 2020. [Online]. Available: http://link.springer.com/10.1557/mre.2020.16

[7] C. Santato and P. Alarco, "The Global Challenge of Electronics: Managing the Present and Preparing the Future," *Adv Materials Technologies*, vol. 7, no. 2, p. 2101265, Feb. 2022. [Online]. Available: https://onlinelibrary.wiley.com/doi/10.1002/admt.202101265

[8] X. Rodríguez-Martínez, F. Saiz, B. Dörling, S. Marina, J. Guo, K. Xu, H. Chen, J. Martin, I. McCulloch, R. Rurali, J. S. Reparaz, and M. Campoy-Quiles, "On The Thermal Conductivity of Conjugated Polymers for Thermoelectrics," *Advanced Energy Materials*, vol. 14, no. 35, p. 2401705, Sep. 2024. [Online]. Available: https://onlinelibrary.wiley.com/doi/10.1002/aenm.202401705

[9] H. Wang and C. Yu, "Organic Thermoelectrics: Materials Preparation, Performance Optimization, and Device Integration," *Joule*, vol. 3, no. 1, pp. 53–80, Jan. 2019. [Online]. Available: https://linkinghub.elsevier.com/retrieve/pii/S2542435118305038

[10] D. Veldman, S. C. J. Meskers, and R. A. J. Janssen, "The Energy of Charge-Transfer States in Electron Donor–Acceptor Blends: Insight into the Energy Losses in Organic Solar Cells," *Adv Funct Materials*, vol. 19, no. 12, pp. 1939–1948, Jun. 2009. [Online]. Available: https://onlinelibrary.wiley.com/doi/10.1002/adfm.200900090

[11] W. C. Tsoi, S. J. Spencer, L. Yang, A. M. Ballantyne, P. G. Nicholson, A. Turnbull, A. G. Shard, C. E. Murphy, D. D. C. Bradley, J. Nelson, and J.-S. Kim, "Effect of Crystallization on the Electronic Energy Levels and Thin Film Morphology of P3HT:PCBM Blends," *Macromolecules*, vol. 44, no. 8, pp. 2944–2952, Apr. 2011. [Online]. Available: https://pubs.acs.org/doi/10.1021/ma102841e

[12] Z. Ke, A. Abtahi, J. Hwang, K. Chen, J. Chaudhary, I. Song, K. Perera, L. You, K. N. Baustert, K. R. Graham, and J. Mei, "Highly Conductive and Solution-Processable n-Doped Transparent Organic Conductor," *J. Am. Chem. Soc.*, vol. 145, no. 6, pp. 3706–3715, Feb. 2023. [Online]. Available: https://pubs.acs.org/doi/10.1021/jacs.2c13051

[13] Snyder, Jeffrey and Toberer, Eric S., "Complex thermoelectric materials," 2008. [Online]. Available: https://www.nature.com/articles/nmat2090

[14] V. Jangra, S. Maity, and P. Vishnoi, "A review on the development of conjugated polymer-based textile thermoelectric generator," *Journal of Industrial Textiles*, vol. 51, no. 1_suppl, pp. 181S–214S, Jun. 2022. [Online]. Available: https://journals.sagepub.com/doi/10.1177/1528083721996732

[15] H. M. Elmoughni, A. K. Menon, R. M. W. Wolfe, and S. K. Yee, "A Textile-Integrated Polymer Thermoelectric Generator for Body Heat Harvesting," *Adv Materials Technologies*, vol. 4, no. 7, p. 1800708, Jul. 2019. [Online]. Available: https://onlinelibrary.wiley.com/doi/10.1002/admt.201800708

[16] G. A. Naydenov, P. J. Hasnip, V. K. Lazarov, and M. I. J. Probert, "Huge power factor in p-type half-Heusler alloys NbFeSb and TaFeSb," *J. Phys. Mater.*, vol. 2, no. 3, p. 035002, Jul. 2019. [Online]. Available: https://iopscience.iop.org/article/10.1088/2515-7639/ab16fb

[17] Eryilmaz, Ilknur H., "Improving the Electrical Characteristics of Organic Devices for Thermoelectric Applications," Ph.D., Institute National de la Recherche Scientifique (INRS), 2023.

[18] Kymissis, Ioannis, *Organic Field Effect Transistors: theory, fabrication and characterization*. Springer Science & Business Media, 2008.

[19] M. Goel, C. D. Heinrich, G. Krauss, and M. Thelakkat, "Principles of Structural Design of Conjugated Polymers Showing Excellent Charge Transport toward Thermoelectrics and Bioelectronics Applications," *Macromol. Rapid Commun.*, vol. 40, no. 10, p.

1800915, May 2019. [Online]. Available: https://onlinelibrary.wiley.com/doi/10.1002/marc.201800915

[20] Rost-Bietsch, Constance, *Ambipolar and light-emitting organic field-effect transistors*. Cuvillier, 2005.

[21] A. Köhler and H. Bässler, *Electronic Processes in Organic Semiconductors*. Wiley-VCH, 2015.

[22] Goupil, Christophe and Tadashi, Mizutani, "Thermodynamics of Thermoelectricity," *InTech*, 2011. [Online]. Available: http://www.intechopen.com/books/thermodynamics/thermodynamics-of-thermoelectricity

[23] H. Fritzsche, "A general expression for the thermoelectric power," *Solid State Communications*, vol. 9, no. 21, pp. 1813–1815, Nov. 1971. [Online]. Available: https://linkinghub.elsevier.com/retrieve/pii/0038109871900962

[24] M. Büttiker, "Absence of backscattering in the quantum Hall effect in multiprobe conductors," *Phys. Rev. B*, vol. 38, no. 14, pp. 9375–9389, Nov. 1988, publisher: American Physical Society (APS). [Online]. Available: https://link.aps.org/doi/10.1103/PhysRevB.38.9375

[25] B. Russ, A. Glaudell, J. J. Urban, M. L. Chabinyc, and R. A. Segalman, "Organic thermoelectric materials for energy harvesting and temperature control," *Nat Rev Mater*, vol. 1, no. 10, p. 16050, Aug. 2016. [Online]. Available: https://www.nature.com/articles/natrevmats201650

[26] Leon van Dommelen, "A11 Thermoelectric effects," 2022. [Online]. Available: https://web1.eng.famu.fsu.edu/~dommelen/quantum/style_a/nt_pelt.html

[27] X. Wang, W. Wang, C. Yang, D. Han, H. Fan, and J. Zhang, "Thermal transport in organic semiconductors," *Journal of Applied Physics*, vol. 130, no. 17, p. 170902, Nov. 2021. [Online]. Available: https://pubs.aip.org/jap/article/130/17/170902/1063659/Thermal-transport-in-organic-semiconductors

[28] W. Kim, "Strategies for engineering phonon transport in thermoelectrics," *J. Mater. Chem. C*, vol. 3, no. 40, pp. 10 336–10 348, 2015. [Online]. Available: https://xlink.rsc.org/?DOI=C5TC01670C

[29] A. M. Glaudell, J. E. Cochran, S. N. Patel, and M. L. Chabinyc, "Impact of the Doping Method on Conductivity and Thermopower in Semiconducting Polythiophenes," *Advanced Energy Materials*, vol. 5, no. 4, p. 1401072, Feb. 2015. [Online]. Available: https://onlinelibrary.wiley.com/doi/10.1002/aenm.201401072

[30] M. Roesing, J. Howell, and D. Boucher, "Solubility characteristics of poly(3-hexylthiophene)," *J Polym Sci B Polym Phys*, vol. 55, no. 14, pp. 1075–1087, Jul. 2017. [Online]. Available: https://onlinelibrary.wiley.com/doi/10.1002/polb.24364

[31] J. Obrzut and K. A. Page, "Electrical conductivity and relaxation in poly(3-hexylthiophene)," *Phys. Rev. B*, vol. 80, no. 19, p. 195211, Nov. 2009. [Online]. Available: https://link.aps.org/doi/10.1103/PhysRevB.80.195211

[32] Jatosado, "File:Electron Beam Deposition 001.jpg," 2012. [Online]. Available: https://commons.wikimedia.org/wiki/File:Electron_Beam_Deposition_001.jpg

[33] G. Majni, "INTERDIFFUSION OF THIN Cr AND Au FILMS DEPOSITED ON SILICON," *Thin Solid Films*, vol. 38, pp. 15–19, 1976.

[34] A. Yilmaz, U. Yilmaz, and M. T. Cakir, "Silver films on glass with very thin chromium adherence interlayers; reflectance and adherence at film-glass interface," *Optik*, vol. 274, p. 170530, Mar. 2023. [Online]. Available: https://linkinghub.elsevier.com/retrieve/pii/S0030402623000268

[35] John Webster, *Electrical Measurement, Signal Processing, and Displays*. CRC Press, 2003.

[36] Ossila, "Calculate Sheet Resistance Using the Four-Probe Method," 2025. [Online]. Available: https://www.ossila.com/pages/sheet-resistance-theory

[37] S. J. Kang, Y. Yi, C. Y. Kim, C. N. Whang, T. A. Callcott, K. Krochak, A. Moewes, and G. S. Chang, "Analysis of octadecyltrichlorosilane treatment of organic thin-film transistors using soft x-ray fluorescence spectroscopy," *Applied Physics Letters*, vol. 86, no. 23, p. 232103, Jun. 2005. [Online]. Available: https://pubs.aip.org/apl/article/86/23/232103/239303/Analysis-of-octadecyltrichlorosilane-treatment-of

[38] M. Devynck, P. Tardy, G. Wantz, Y. Nicolas, and L. Hirsch, "Organic field-effect transistor with octadecyltrichlorosilane (OTS) self-assembled monolayers on gate oxide: effect of OTS quality," *Eur. Phys. J. Appl. Phys.*, vol. 56, no. 3, p. 34106, Dec. 2011. [Online]. Available: http://www.epjap.org/10.1051/epjap/2011110138

[39] D. S. Park, S. J. Kang, H. J. Kim, M. H. Jang, M. Noh, K.-H. Yoo, C. N. Whang, Y. S. Lee, and M. H. Lee, "Characteristics of perylene-based organic thin-film transistor with octadecyltrichlorosilane monolayer," *Journal of Vacuum Science & Technology B: Microelectronics and Nanometer Structures Processing, Measurement, and Phenomena*, vol. 23, no. 3, pp. 926–929, May 2005. [Online]. Available: https://pubs.aip.org/jvb/article/23/3/926/469676/Characteristics-of-perylene-based-organic-thin

[40] Y. Wang and M. Lieberman, "Growth of Ultrasmooth Octadecyltrichlorosilane Self-Assembled Monolayers on SiO_2," *Langmuir*, vol. 19, no. 4, pp. 1159–1167, Feb. 2003. [Online]. Available: https://pubs.acs.org/doi/10.1021/la020697x

[41] H. Li, J. Mei, A. L. Ayzner, M. F. Toney, J. B.-H. Tok, and Z. Bao, "A simple droplet pinning method for polymer film deposition for measuring charge transport in a thin film transistor," *Organic Electronics*, vol. 13, no. 11, pp. 2450–2460, Nov. 2012. [Online]. Available: https://linkinghub.elsevier.com/retrieve/pii/S1566119912003278

[42] H. Tang, Y. Liang, C. Liu, Z. Hu, Y. Deng, H. Guo, Z. Yu, A. Song, H. Zhao, D. Zhao, Y. Zhang, X. Guo, J. Pei, Y. Ma, Y. Cao, and F. Huang, "A solution-processed n-type conducting polymer with ultrahigh conductivity," *Nature*, vol. 611, no. 7935, pp. 271–277, Nov. 2022. [Online]. Available: https://www.nature.com/articles/s41586-022-05295-8

[43] J. Y. Na, B. Kang, D. H. Sin, K. Cho, and Y. D. Park, "Understanding Solidification of Polythiophene Thin Films during Spin-Coating: Effects of Spin-Coating Time and Processing Additives," *Sci Rep*, vol. 5, no. 1, p. 13288, Aug. 2015. [Online]. Available: https://www.nature.com/articles/srep13288

[44] P. M. Chaikin, "An Introduction to Thermopower for Those Who Might Want to Use It to Study Organic Conductors and Superconductors," in *Organic Superconductivity*, V. Z. Kresin and W. A. Little, Eds. Boston, MA: Springer US, 1990, pp. 101–115. [Online]. Available: http://link.springer.com/10.1007/978-1-4899-2605-0_11

[45] G. Zuo, X. Liu, M. Fahlman, and M. Kemerink, "High Seebeck Coefficient in Mixtures of Conjugated Polymers," *Adv Funct Materials*, vol. 28, no. 15, p. 1703280, Apr. 2018. [Online]. Available: https://onlinelibrary.wiley.com/doi/10.1002/adfm.201703280

[46] Y. Zou, D. Huang, Q. Meng, C.-a. Di, and D. Zhu, "Correlation between Seebeck coefficient and transport energy level in poly(3-hexylthiophene)," *Organic Electronics*, vol. 56, pp. 125–128, May 2018, publisher: Elsevier BV. [Online]. Available: https://linkinghub.elsevier.com/retrieve/pii/S1566119918300508

[47] Z. Bao, A. Dodabalapur, and A. J. Lovinger, "Soluble and processable regioregular poly(3-hexylthiophene) for thin film field-effect transistor applications with high mobility," *Applied Physics Letters*, vol. 69, no. 26, pp. 4108–4110, Dec. 1996. [Online]. Available: https://pubs.aip.org/apl/article/69/26/4108/1059754/Soluble-and-processable-regioregular-poly-3

[48] G. Wang, J. Swensen, D. Moses, and A. J. Heeger, "Increased mobility from regioregular poly(3-hexylthiophene) field-effect transistors," *Journal of Applied Physics*, vol. 93, no. 10, pp. 6137–6141, May 2003. [Online]. Available: https://pubs.aip.org/jap/article/93/10/6137/472293/Increased-mobility-from-regioregular-poly-3

[49] C.-x. Jiang, X.-m. Cheng, X.-m. Wu, X.-y. Yang, B. Yin, Y.-l. Hua, J. Wei, and S.-g. Yin, "Effects of P3HT concentration on the performance of organic field effect transistors," *Optoelectron. Lett.*, vol. 7, no. 1, pp. 30–32, Jan. 2011, publisher: Springer Science and Business Media LLC. [Online]. Available: http://link.springer.com/10.1007/s11801-011-0122-z

[50] M. Fahlman, S. Fabiano, V. Gueskine, D. Simon, M. Berggren, and X. Crispin, "Interfaces in organic electronics," *Nat Rev Mater*, vol. 4, no. 10, pp. 627–650, Jul. 2019, publisher: Springer Science and Business Media LLC. [Online]. Available: https://www.nature.com/articles/s41578-019-0127-y

[51] X. Guo, M. Baumgarten, and K. Müllen, "Designing pi-conjugated polymers for organic electronics," *Progress in Polymer Science*, vol. 38, no. 12, pp. 1832–1908, Dec. 2013, publisher: Elsevier BV. [Online]. Available: https://linkinghub.elsevier.com/retrieve/pii/S0079670013001196

[52] A. D. Scaccabarozzi, A. Basu, F. Aniés, J. Liu, O. Zapata-Arteaga, R. Warren, Y. Firdaus, M. I. Nugraha, Y. Lin, M. Campoy-Quiles, N. Koch, C. Müller, L. Tsetseris, M. Heeney, and T. D. Anthopoulos, "Doping Approaches for Organic Semiconductors," *Chem. Rev.*, vol. 122, no. 4, pp. 4420–4492, Feb. 2022. [Online]. Available: https://pubs.acs.org/doi/10.1021/acs.chemrev.1c00581

[53] I. Salzmann, G. Heimel, M. Oehzelt, S. Winkler, and N. Koch, "Molecular Electrical Doping of Organic Semiconductors: Fundamental Mechanisms and Emerging Dopant Design Rules," *Acc. Chem. Res.*, vol. 49, no. 3, pp. 370–378, Mar. 2016. [Online]. Available: https://pubs.acs.org/doi/10.1021/acs.accounts.5b00438

[54] B. Lüssem, C.-M. Keum, D. Kasemann, B. Naab, Z. Bao, and K. Leo, "Doped Organic Transistors," *Chem. Rev.*, vol. 116, no. 22, pp. 13 714–13 751, Nov. 2016. [Online]. Available: https://pubs.acs.org/doi/10.1021/acs.chemrev.6b00329

[55] S. M. Sze and K. K. Ng, *Physics of semiconductor devices*, 3rd ed., ser. Wiley-Interscience online books. Hoboken, N.J: Wiley-Interscience, 2007.

[56] Streetman, Ben G. and Sanjay, Banerjee, *Solid State electronic Devices*, 5th ed., New Jersey, 2000.

[57] "Solvent Miscibility Table," 2025. [Online]. Available: https://www.sigmaaldrich.com/CA/en/technical-documents/technical-article/analytical-chemistry/purification/solvent-miscibility-table?srsltid=AfmBOopjWsnpHxBxDvlqsP51ud0W4CmzXOeOTg0VZlSBw7dHfCCjaszi

[58] A. Besganz, V. Zöllmer, R. Kun, E. Pál, L. Walder, and M. Busse, "Inkjet Printing as a Flexible Technology for the Deposition of Thermoelectric Composite

Structures," *Procedia Technology*, vol. 15, pp. 99–106, 2014. [Online]. Available: https://linkinghub.elsevier.com/retrieve/pii/S2212017314001583

[59] A. Mazaheripour, S. Majumdar, D. Hanemann-Rawlings, E. M. Thomas, C. McGuiness, L. d'Alencon, M. L. Chabinyc, and R. A. Segalman, "Tailoring the Seebeck Coefficient of PEDOT:PSS by Controlling Ion Stoichiometry in Ionic Liquid Additives," *Chem. Mater.*, vol. 30, no. 14, pp. 4816–4822, Jul. 2018. [Online]. Available: https://pubs.acs.org/doi/10.1021/acs.chemmater.8b02114

[60] Luisiana State University, "Chloroform Solvent Properties." [Online]. Available: https://macro.lsu.edu/howto/solvents/chloroform.htm

[61] American Chemical Society, "Dimethyl sulfoxide." [Online]. Available: https://www.acs.org/molecule-of-the-week/archive/d/dimethyl-sulfoxide.html

Declaration of Authenticity

I hereby declare that the thesis on the above topic has been written independently, and no sources or aids other than those specified have been used, with verbatim and analogous quotations marked as such. As part of the double degree programme with the Institut national de la recherche scientifique, this thesis will only be submitted to Munich University of Applied Sciences and the Institut national de la recherche scientifique. It has not yet been submitted to any other examination authority and has not been published.

Marc Daniel Paulik, Montreal, 14.08.2025